國立中山大學 材料與光電科學系

碩士論文

Department of Materials and Optoelectronic Science

National Sun Yat-sen University

Master Thesis

奈米與非晶多層薄膜於聚亞醯胺基板上之變形機制

Deformation Mechanism of Amorphous/nanocrystalline Multilayer Thin Films on Polyimide Substrates

研究生：黃瀚生

Han-Sheng Huang

指導教授：黃志青 博士

Dr. J. C. Huang

中華民國 100 年 8 月

August 2011

論文審定書

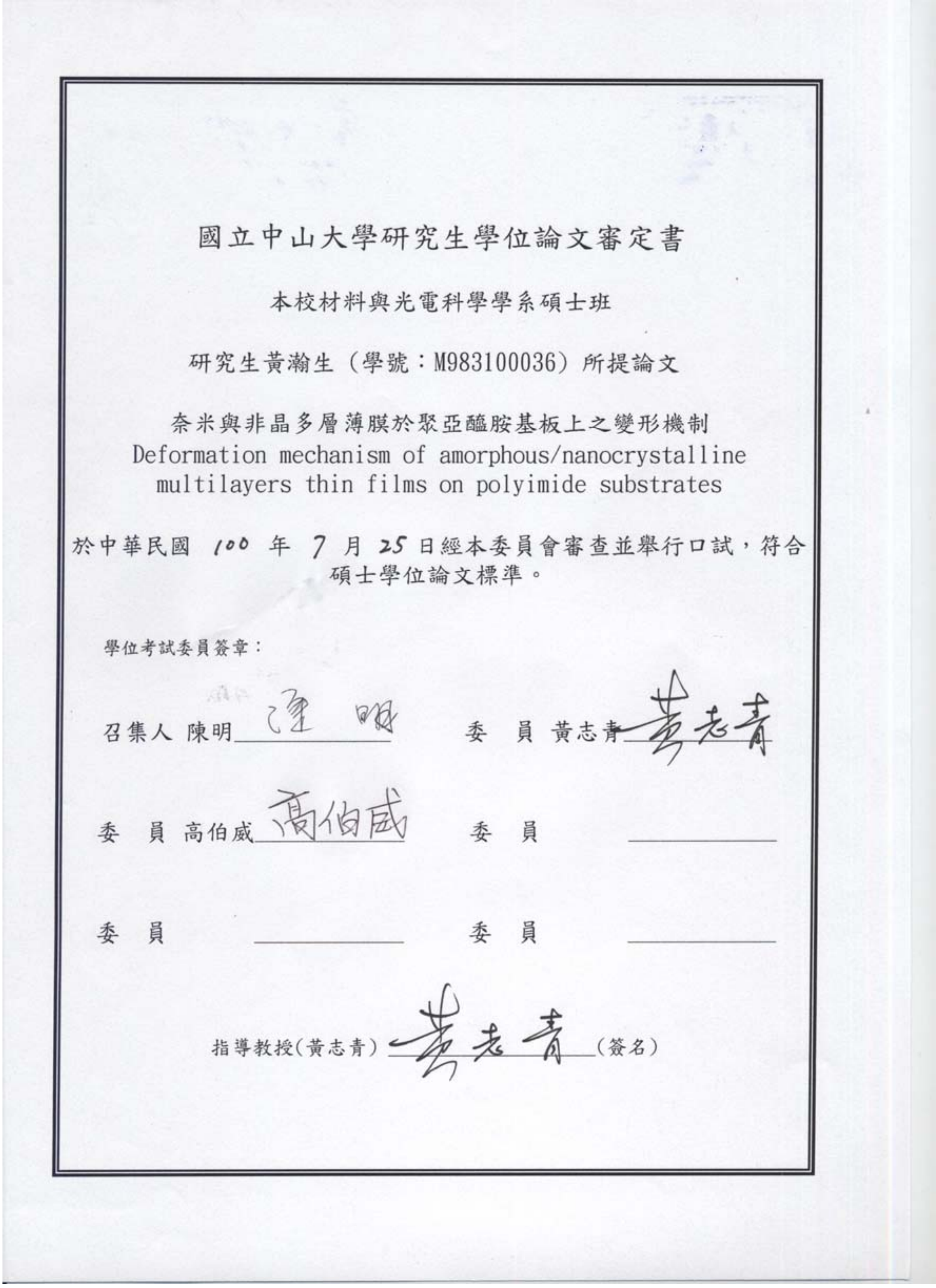

國立中山大學研究生學位論文審定書

本校材料與光電科學學系碩士班

研究生黃瀚生（學號：M983100036）所提論文

奈米與非晶多層薄膜於聚亞醯胺基板上之變形機制
Deformation mechanism of amorphous/nanocrystalline
multilayers thin films on polyimide substrates

於中華民國 100 年 7 月 25 日經本委員會審查並舉行口試，符合碩士學位論文標準。

學位考試委員簽章：

召集人 陳明 陳 明　　委　員 黃志青 黃志青

委　員 高伯威 高伯威　　委　員 ____________

委　員 ____________　　委　員 ____________

指導教授（黃志青） 黃志青 （簽名）

致謝

轉眼間，兩年的碩士生涯就這麼過去了。想當初對於中山大學一無所知，到現在對於校內各處瞭若指掌，真是讓人無限唏嘘。回顧這段時間中，首先我要感謝的是我的恩師 黃志青教授，帶領我這個對於金屬玻璃、甚至材料機械性質都不甚瞭解的學生，在身兼行政重任之餘仍能教導我一步一步瞭解這門領域的博大精深，甚至帶領我參與舉辦於香港的國際研討會，讓我在實驗資源不虞匱乏的環境中，自由的學習、向前邁進，真的是相當、相當的感謝黃老師。另外，也感謝口試委員高博威教授與陳明教授。高博威教授在研究計畫提審時即擔任過口試委員，對於實驗方法的設計與改良不藏私的提供自己的意見；擔任口試委員時，也與陳明教授提供相當寶貴的意見與指正，使本篇研究更加完整。

研究之路上的跌跌撞撞，也要感謝實驗室其他成員的幫忙與付出，讓我的研究更加順利。敬仁大學長提供了我實驗整體的設計的大方向，更在口試前的週末專程到學校幫我改正投影片的製作；大神育成學長雖然只有短短的回來一年，對於我所欠缺的高分子變形知識、電腦數據處理分析提供了很大的幫助，由衷的感謝兩位博士後學長。感謝浩然學長教導我拉伸機台的使用、與各種在寫作需要注意的地方有著精確的指導；鴻昇學長對於實驗一些細節，提供了獨到的見解；名哲學長對於實驗機台與做事道理的教導。謝謝大豪、哲男、阿官、朝先學長，在我實驗後期的那段壓抑的狀態，帶給實驗室大大的歡笑。感謝這位又是姊姊、同學、學妹的婷婷、還有兩位好學弟維昭和盈翰，讓我可以專心的準備口試與實驗，不必為其他的事煩惱。

此外，也要感謝死黨柏翰，在我壓力大的時候能夠當我情緒的垃圾桶，中午的時候吃飯不無聊。最早畢業的資津，以妳作為學習目標、還有妳所贈送的擺飾是我很熬夜實驗時，很重要的心靈支柱。也要感謝儀佳，妳讓我見識到人性的另一面，也不會再為朋友掏心挖肺。還有大哥冠綸、遠豪、宗霖、凱平、瓊文、雅琪、鈞隆、承瑋、國孝、雅婷等各位研究所的戰友，感謝你們與我一起奮戰到底。

最後，謝謝我的父母，在學業上包容我、容許我三不五時的熬夜、徹夜未歸的在外實驗。沒有您們的關愛呵護，就沒有今天的我。謹以此篇微不足道的論文，感謝您們對我的養育之恩。

摘要

本實驗選用沈積於聚亞醯胺（Polyimide，PI）基板上的單層非晶質 ZrCu 合金薄膜、單層結晶 Cu 薄膜與兩者之複合多層薄膜，研究並探討在相同體積分率情況下，其微拉伸行為與層厚度之間的關係。在掃描式電子顯微鏡（Scanning electron microscope，SEM）表面形貌的觀察中可以發現，多層薄膜表面之主要由球狀區域所構成；而應力集中會發生各球狀區域間，可由垂直於拉伸方向的裂痕會沿著球狀區域擴展得知。由能量解析光譜儀（Energy dispersive X-ray spectrometer，EDS）測量之成份分析結果顯示非晶質薄膜的原子百分比為 $Zr_{46.78}Cu_{53.22}$，接近預設目標之 $Zr_{50}Cu_{50}$。X 光繞設（X-ray diffraction，XRD）結果顯示多層薄膜結晶結構同時由非晶質 ZrCu 與結晶 Cu 所構成，在單層厚度降低時，結晶銅的正規化峰值與半高寬大小皆隨之降低。在本研究中，為取得單純由鍍膜的機械性質所產生的訊號，採用拉伸測試後減去基板貢獻的方式，再行後部的計算。以此法所獲得之單層非晶質 ZrCu 與單層結晶 Cu 之拉伸楊氏模數，接近於由微硬度壓痕測試所得數據；檢測多層膜之機械性質，可發現拉伸楊氏模數符合複合材料混合法則(Rule of Mixture)預測，可知此減去基板貢獻方法為可信賴的。隨著層厚度由 100 奈米降至 10 奈米，楊氏模數無明顯的改變。另一方面，最大應力值隨著層厚變化有明顯的改變，在層厚度為 25 奈米時具有相對最大的最大應力值。分析多層膜拉伸後之表面形貌，厚度的影響對於機械性質的影響可發現相同的趨勢。在本論文中對於單層與多層膜的拉伸機械性質會有詳細的研究與討論。

關鍵字：金屬玻璃、多層膜、薄膜、拉伸試驗

Abstract

The tensile behavior of the monolithic amorphous ZrCu and crystalline Cu thin films and the ZrCu/Cu multilayered thin films, coated on polyimide (PI) substrates in different layer thicknesses has been investigated. The scanning electron microscope (SEM) morphology of the as-deposited thin film is composed of sphere domains. Between the domains, stress concentration is induced. The cracks perpendicular to the loading direction would propagate along the domains. The constituent component examined by energy dispersive X-ray spectrometer (EDS) shows that the average composition (in atomic percent) amorphous thin film is $Zr_{46.78}Cu_{53.22}$, closed to the designed $Zr_{50}Cu_{50}$ goal. The X-ray diffraction (XRD) results show that the multilayered specimens are composed of both amorphous ZrCu and nanocrystalline Cu crystal structure. As the monolayer thickness become lower, the normalized peak height and grain sizes of Cu become lower. To obtain the mechanical properties of the coated films, deducting the contribution of substrates is used in this study. The tensile Young's moduli of monolithic amorphous ZrCu and nanocrystalline Cu thin films are close to the results extracted from micro-compression. Based on the current tensile results for the moduli of multilayered thin films, the obtained mechanical data are demonstrated to be reliable and are consistent with the theoretical values predicted by Rule of Mixture. As the thickness decreases from 100 nm down to 10 nm, the tensile Young's moduli do not vary much. On the other hand, the maximum tensile stress shows strong variation, being highest for the layer thickness of 25 nm. The deformed surface morphologies characterized by scanning electron microscopy also exhibit a similar trend. The optimum tensile properties of the monolithic and multilayered thin film combinations are examined and discussed in this thesis.

Key word: metallic glass, multilayer, thin film, tensile test

Content

List of Tables

List of Figures

Chapter 1 Introduction

1-1 Amorphous alloy

Amorphous alloys were discovered in 1960 when rapid quenching methods were first applied to liquid metal alloys [1]. They are metallic materials with a random or disordered atomic structure, unlike common metals having crystalline structure and atoms on repeated locations. The amorphous alloys are non-crystalline, meaning that atoms of amorphous alloys are randomly or short-ranged arranged. The difference of atomic arrangement between amorphous alloys and crystalline materials can be illustrated by Figure 1.1 [2]. Therefore, amorphous alloys can be called as "glassy metal" or "metallic glasses". Because of the unique atomic structure, amorphous alloys exhibit some significant characteristics, such as high strength and hardness, good corrosion resistance, larger elastic elongation limit [3] and special electric or magnetic properties [3, 4]. The features and applications of amorphous alloys are summarized in Table 1.1 [4].

Moreover, lots of methods for manufacturing amorphous alloys have been developed, such as sputtering [5], solid-state reaction [6], melt spinning [7], mechanical alloying [8] and suction-casting [9]. Some methods are utilized through cooling processes, and others are utilized by physical deposition or chemical reaction. Up to now, a great number of scientists and engineers have paid much attention in fabricating new amorphous alloy systems.

1-2 The development of thin film metallic glasses

Though many methods of fabricating amorphous alloys have been developed, most of them are used to make large size or bulk metallic glasses. Because of the near-zero tensile ductility, bulk metallic glasses (BMGs) are not easy to act as engineering materials [10]. On the other hand, according to their high strength and hardness, they appear to be promising coating materials. So far, many techniques of depositing thin film metallic glasses (TFMGs) have been developed. Among them, thermal evaporation and magnetron sputtering are in used for fabricating thin film of amorphous alloy. The related properties of thin film metallic glasses have been prepared by their methods investigated extensively.

It is well-known that the structure of as-deposited thin film depends on not only the composition of thin film, but also other deposition parameters, such as temperature of reaction, working distance, flow rate of carrying gas, pressure, atomic mobility, etc. So, thin film metallic glasses have lots of aspects to study and have been investigated from decades ago. In 1978, Forester et al. [11] made metallic glass film overlays of Fe-B as substrate by co-evaporation. In 1983, Schwarz and Johnson [12] utilized solid-state reaction to fabricate the La-Au TFMG. A few years later, Cotts et al. [13] successfully synthesized the Ni-Zr multilayer thin film by the magnetron sputtering method. In 1988, the Al-Fe and Bi-Ti binary thin films were fabricated by Chen et al. [14]. Then, Minnigerode et al. [15, 16] synthesized the Zr-Cu and Co-Cu thin films of amorphous alloys by electron-beam evaporation on the sapphire substrate. In 1996, Dudonis et al. [17] used co-sputtering to produce the Zr-Cu TFMGs. About the same time, various compositions of Zr and Cu thin film amorphous alloys were fabricated. After the binary thin film produced, Shimokohbe's group [18, 19] established the Zr-Cu-Al and Pd-Cu-Si ternary systems for TFMGs by using sputtering method and demonstrated their applications in micro electromechanical systems (MEMS). In 2000s, Shimokohbe and his cowokers [18, 20] then fabricated the Pd-based and Zr-based TFMGs by radio frequency (RF) magnetron sputtering method; Chu et al. [21] had also made TiNi-based amorphous alloy of thin film with RF-magnetron sputtering at this period.

In recent year after 2000, the mechanical and thermal properties of TFMGs have been investigated in a more advanced way. However, not just focusing TFMGs, the mechanical property of crystalline alloys were also investigated. In 2001, Grummon and Zhang [22] studied intrinsic stresses in sputtered films of crystalline and amorphous Ti-Ni alloy by means of tensile testing. Hashemi et al. [23] experimented the amorphous and partially crystalline silicon overlay by tensile and compressive testing. Unlike the former researchers, Nieh and Wadsworth [24] demonstrated the new concept of composite materials that combine the advantages of crystal and amorphous metals, which exhibiting high strength and toughness. Different from focusing on hard substrate, Xiang et al. [25] and Niu et al. [26] examined copper thin film deposited on polyimide in 2005 and 2007, respectively.

1-3 Flexible polymer substrates

For electronic industries, smaller and smaller devices are needed. So, deformable substrates are being much more used. They could be well applied as paperlike displays [27, 28], sensitive skins [29] and electronic textiles [30]. Comparing to common polymer materials, polyimide (PI) has many advantages, such as high temperature stability, radiation, oxidation and high chemical resistance, low dielectric constant, and excellent mechanical properties. Based on these significant properties, PI has been employed for many years no matter on itself or as substrate.

In 1991, Bell and Glocker [31] measured the stress profile in sputtered AlN on polyimide as a function of total gas pressure and argon-to-nitrogen partial pressure ratio. In next year, Choi and Kim [32] investigated delamination between the PI film and glass substrate by tensile testing. In 1997, the aluminum films deposited on PI-coated Si wafer by sputtering were studied by Kang and Ho [33]. In next year, Macionczyk et al. [34] investigated the mechanical property of CuNi (Mn) film on the 8-μm-thick PI substrate. In 1999, amorphous silicon used as transistors on polyimide foil was tested for its failure resistance of bending by Gleskova et al. [35]. In 2001, Kraft et al. [36] synthesized copper foil on polyimide and investigated the fatigue property. In 2002, in situ tensile testing of tungsten thin film with coupling X-ray diffraction measurements was preformed by Badawi et al. [37], and they had conclusions that for tungsten thin film, the obtained Young's modulus was close to the bulk material one. Yu and Spaepen [38] had deposited copper thin film on the 7.6-mm-thick Kapton® substrates with mask covering the polymer substrate, and examined the tensile properties of the copper thin film.

1-4 Motivation

Metallic glasses have unique atomic structure, unlike normal crystalline materials having defects or generating dislocations, so they are potential materials for the MEMS and other applications for some functional purposes, such as good wear and corrosion resistance, molding, etc. Because of easy fracture and brittleness, BMGs are not easy to be formed or processed into MEMS. Oppositely, thin film techniques can be employed to fabricate TFMGs. Furthermore, adjustment of component or crystal structure of thin films can be introduced to change properties of metallic glasses. Das et al. [39] and Liu et al. [40] both found that introducing inhomogeneous amorphous phases can largely enhance the plasticity in the BMGs. Lee et al. [41] considered that the embedded crystalline particles in a Cu-based BMG could improve the plasticity significantly. These results indicate that two coexisting phases can influence the movement of shear bands and improve the plasticity.

Preparing metallic glasses as thin films on a flexible substrate is also potentially useful, because it will solve two problems for metallic glass application. First, thin films can be prepared with a large area which is comparable with amorphous thread and ribbon. Complex composition and multilayer structure can now be realized by various deposition methods. A typical example is the magnetic materials prepared by roll deposition on flexible polymer substrates [42]. In addition, mechanical properties, especially plasticity, ductility or toughness, can be improved by structure design. Recent research on flexible electronics has shown that well-bonded functional films can be effectively supported by the substrate, enhancing ductility [25]. Similar enhancement should be possible for metallic glass films on flexible substrates. Inserting a secondary phase is another effective method to improve ductility.

Though metallic glasses have been discovered for decades, the tensile properties of metallic glasses on polymers are not yet to be investigated in details. In this study, the amorphous/nanocrystalline multilayer nanolaminate system is selected to deposit on the polymer substrates. The amorphous and nanocrystalline layers are metallic ZrCu metallic glass and nanocrystalline Cu thin film, respectively. The polymer substrates are 50-μm-thick Kapton® film. The nanocrystalline layer is chosen to suppress or absorb the energy of shear bands under the tensile testing in multilayer system. The composition and thickness of the individual ZrCu and nanocrystalline layers are controlled by alternative sputtering deposition. In this study, a set of amorphous/nanocrystalline nanolaminate samples are prepared with different nanocrystalline layer thicknesses. The thickness of nanocrystalline layers is controlled from 100 nm to 10 nm by sputtering, and the composition of nanocrystalline layers focuses on face centered cubic (FCC) metal. The microstructure, mechanical properties will be examined.

Chapter 2 Background and Literature Review

2-1 Properties of thin film metallic glasses

2-1-1 Electrical properties

The electrical properties are important factors for MEMS applications. As mentioned above, metallic glasses have the isotropy and homogeneous atom arrangement, it is not easy for electrons transporting through uncrystallized region. In cases of copper-involved systems, thin film metallic glasses all have higher electrical resistance than Cu and W films, as compared in Table 2.1 [43]. In order to enhance metallic glass conductivity, crystalline metal would be introduced. By means of 4 point probe measurement under annealing, the resistivity of Pd-TFMG is measured as a function of annealing temperature, as shown in Figure 2.1 [44]. There is a resistivity drop of TFMG, due to partial crystallization of the TFMG material. This phenomenon not only occurs from metallic glasses, the same observation was found other cases like MgAlZn [45] and $Be_{40}Ti_{50}Zr_{10}$ [46] systems.

2-1-2 Magnetic properties

The magnetic properties of metallic glass are not yet to be investigated in very detail, since atoms with magnetism are randomly arranged or only have short range order. Generally speaking, magnetic materials would contain magnetic element such as iron, cobalt or nickel, so the category of metallic glasses is constrained. In Fe-based metallic glasses, Chu et al. [47] indicated that the Fe-Ti-Co-Ni-B-Nb film would transform into various nanoscale and amorphous structures during annealing. The transmission electron microscopy (TEM) image and crystal structure are shown in Figure 2.2. As the annealing temperature is raised, the film transforms into nanocrystalline then again amorphous. There is no obvious color contrast in the images up to 873 K, suggesting that random magnetization directions lie in the plane of the film. The perpendicular magnetic anisotropy for the films annealed at 923 - 973 K is attributed to the internal stress caused by the existence of cubic Fe (Ni) phase with the minor FeNi phase, as shown in Figure 2.3.

2-1-3 Thermal properties

The thermal stability of the amorphous thin films is the most important key for the micro-forming application. The viscous flow in the supercooled liquid region makes metallic glasses easily to form into three-dimensional structure MEMS. The Zr-Cu metallic glass system allows a large range for zirconium/copper ratio to maintain the amorphous structure. Figure 2.4 [48] shows the DSC traces of the 1-mm-diameter rods for compositions ranging from $Cu_{40}Zr_{60}$ to $Cu_{66}Zr_{34}$. The more zirconium content increases, the less glass transition and crystallization temperature the metallic glasses will have, as inserted in Figure 2.5 [48, 49, 50, 51, 52].

On the other hand, the time-temperature-transformation (TTT) diagrams showing the property of thermal stability can be constructed using DSC. Figure 2.6 [53] shows the TTT diagrams foe the Zr-based TFMGs and the time till the onset of crystallization and amorphization can be seen. In addition, the permissible interval of heating time and temperature of TFMGs can also be ascertained for the micro-forming process and annealing heat treatment.

2-1-4 Mechanical properties

According to the random atomic structure of amorphous alloys, metallic glasses exhibit unique mechanical properties different from regular crystalline metals which are associated with motions of dislocations under the applied stresses. That is to say, the amorphous alloys exhibit higher strength than the traditional crystalline alloys, as shown in Figure 2.7 [4].

It is well known that the plastic deformation of crystalline materials starts when the shear stress is higher than the critical resolved shear stress (CRSS) on the slip plane. At the same time, dislocations may be formed and move along the slip directions on the slip planes. It means that mechanical properties of crystalline materials rely strongly on their crystal structure. However, the plastic deformation mechanism by dislocations does not occur in amorphous alloys for the lack of long-range-ordered structure. The amorphous alloys deform by different deformation mechanisms.

In Figure 2.8 [68], there are lots of small unoccupied spaces among atoms, called free volumes, existing within the amorphous short-range-order structure. The plastic deformation in amorphous alloy can be seen as a diffusion-like process involving small units of plasticity that are called flow defects or shear transformation zones (STZs) [54, 55]. STZs act as a fundamental unit of plasticity that formed a small cluster of randomly close-packed atoms in amorphous environment. These zones are usually about 10~50 atoms in open spaces or free volume sites distributing all over the amorphous structure. Figure 2.8 also illustrates the STZ deformation in two-dimensional space. Therefore, the physical mechanisms behind the glass structure and deformation can be localized in this fine scale. In other words, it is usually assumed that the amount and distribution of free volumes dominate the plastic deformation of amorphous alloys. In 2005, Dai et al. [56] reported that the moving of STZs may cause the adiabatic heat near the STZ. The temperature around the shear band would increase rapidly with more and more STZs moving on the shear plane. If the temperature reaches the glass transition temperature and the amorphous alloy becomes viscous flow, the fluid region will be formed in the shear plane, as shown in Figure 2.9 [68]. This fluid region offers more free volume sites for STZs, and makes the plastic deformation of amorphous alloy more easily.

2-2 Property of polyimide substrate

2-2-1 Characteristics of polyimide

Polyimide (PI) is a polymer of imide monomers. The structural formulae of polyimide are shown in Figure 2.10 [57]. The common used PI films are UPILEX® and Kapton®, produced by UBE industry and DuPont, respectively. PI has many advantages, such as high temperature stability, high radiation /oxidation /chemical resistance, low dielectric constant, and excellent mechanical properties, so it can be used in aeronautical, electrical engineering, mechanical and electronics industry.

There are many remarkable properties for the polyimide film, summarized in the following paragraph [58]:

1. Outstanding thermal resisting: PI does not melt or burn as it has the highest UL-94 flammability rating: V-0. It can be used at both high and low temperature extremes where other organic polymeric materials would not be functional. At temperature of 240 °C, it would not be damaged; even at 400 °C, PI still can resist for a short while. On condition of 300 °C and 2500 V/mm, PI will maintain its insulation of electricity, so PI is proper for flexible printed circuit. At a low temperature of -269 °C, PI can remain its elasticity without brittlement or losing its original characteristics.

2. Distinct mechanical properties: PI has high yield strength, toughness and fracture stress comparing to other polymers, so it fits well to industrial demand. For use of flexible printed circuit boards, it especially needs high resistance of friction and folding. The PI-made flexible printed circuit boards can be twisted or plaited except failure of the circuit.

3. Remarkable electrical properties: PI has good performance of insulating, dielectric and diffusing properties. For 25-μm-thick PI, the dielectric strength is 7000 V; if the temperature raises to 300 °C, the dielectric strength will only reduce to 2500 V. PI has high dielectric constant and low diffusion ability, so it can reduce noises in low working voltage for using as flexible printed circuit boards.

2-2-2 Interface characteristics between metal and polyimide [59]

The metallization of polyimide has been investigated for a long time, and the adhesion between metals and polymer had been tested by Fourier transform infrared reflection absorption spectroscopy (FT-IRA). The Kapton® film in this thesis is PMDA-ODA type shown in Figure 2.10. For metals that do not have high reactivity such as gold, silver, copper and palladium, they are hardly to have chemical bond with polyimide. Chromium atoms interact in several possible ways with the pyromellitimide part (PMDA-functional group) of the polymer but do not (contrary to metallic chromium) disrupt the polymer units, and potassium reacts as expected by reducing the polymer.

Figure 2.11 illustrates the FT-IRA difference spectra for Cr, Cu, Pd, Ag, Au, and K deposited onto polyimide. The FT-IRA spectra for the metals are similar over the whole coverage range. The difference in chemical reactivity between chromium and the other metals is not apparent in the FT-IRA difference spectra. The similarity of the IR difference spectra for chromium, copper, palladium, silver, and gold could be seen as evidence that the changes in the IR data are caused by nonchemical effects. However, strong chemical changes as induced by argon ion bombardment also cause attenuation of the IR bands.

2-3 Uniaxial tensile test of thin films

Table 2.3 shows the advantage and disadvantage of thin film mechanical properties testing methods. In a tension test, a specimen is subjected to a continually increasing uniaxial tensile force while simultaneous observations are made of the elongation of the specimen. An engineering stress-strain curve can be constructed from the load-elongation measurements illustrated in Figure 2.12 [60]. Properties that may be determined from this curve include the Young’s modulus, yield strength, tensile strength, work hardening rate and ductility. Standard tensile testing methods for metal foils have been developed, but these are not always directly applicable to the very thin films produced by vapor deposition processes.

Specimens for tensile testing can be cut using a variety of techniques; these can range from the very simple, for example: scalpels and razor blades, to more complicated techniques, such as the electrical discharge machining. Tensile samples can also be vacuum deposited in their final shape through the use of masks and can even assume the traditional “dog-bone shape” [61]. Samples can be removed from the substrate on which they were deposited either through the dissolution of a parting agent such as a soluble salt or dissolution of the substrate itself in a suitable medium.

In addition to the use of conventional testing equipment (usually “hard” motor or hydraulic driven units with strain gauge or differential transformer instrumented extensometers), a large variety of microtensile testing machines have been developed specifically for the testing of thin films. These differ in the way in which the force is applied, the extension measured and the method of mounting the specimen. The force necessary to deform a sample is often controlled electromagnetically but other schemes have been described including thermal expansion [62]. The measurement of extension can be accomplished either directly, through optical microscope observation of the sample or its linkages [63], or indirectly using for example a differential transducer [64]. A wide variety of gripping systems have been used for foil samples. One popular strategy is to attach the specimen using a suitable glue, for instance Eastman 910, either directly to the grips [65] or to an intermediate pull rod [61]. Friction grips have been used and researchers have developed variations on the conventional corrugated metal design, e.g. Plexiglass grip faces cushioned with 12 μm copper foils [66]. A unique gripping system is employed with the "nano-tensilemeter" developed by Andeen et al. [67]; samples are held onto the glass slides which form the grips by van der waals forces.

Chapter 3 Experimental Procedures

In this study, multilayered thin films were chosen in amorphous/nanocrystalline system. The thickness and composition of each metallic layer were controlled by alternative deposition of ZrCu and Cu by magnetron sputtering. The microstructure was examined by scanning electron microscopy (SEM) and X-ray diffraction (XRD). The mechanical properties of tensile test were examined by MTS Tytron® 250 mini-tester.

3-1 Materials and equipment

The sputter equipment used in the thesis is the Multi-Target Sputter (Psur-100HB), purchased from the Advanced System Technology (AST) Corporation. The 4 inches targets, Cu and Zr, used in this study were purchased from the Well Being Enterprise Co., Ltd. The purities of copper and zirconium are both as pure as 99.99%. Polymer substrates made of Polyimide film (Kapton® FPC) were purchased from DuPont®. Figure 3.1 shows the flow chart of experimental procedures.

3-2 Sample preparation

3-2-1 Substrate preparation

In order to avoid organics or dust affecting experimental results, the surface of polymer substrate should be carefully cleaned.

1. The polyimide film 50 μm in thickness was firstly cut into suitable size.
2. Clean the surface of polymer subtrate by ultrasonic cleaning in isopropanol for 5 minutes.
3. After emptying out organic solvent, the beaker would be filled up with deionized water for three times. Ultrasonic cleaner would then be used with deionized water for 10 minutes.
4. In the end, polymer substrates were dried by wiped water off.

3-2-2 Preparation for thin film and multilayered thin films

In this study, thin films were synthesized by the magnetron sputtering equipment with one magnetron DC and two magnetron RF guns, which is set as the Cu target on the RF gun and the Zr target on the DC gun.. The amorphous ZrCu layers were deposited by co-sputtering with the DC and RF guns, and the nanocrystalline Cu layers were just by the RF gun. The multilayered specimens were layer-by-layered deposited with alternative amorphous and nanocrystalline thin films in different layer thicknesses. In order to avoid sample crimping, the films with thicknesses of 1 μm were deposited through a stainless squire-patterned mask 0.3 mm in thickness, and the deposited pattern is shown in Figure 3.2. The deposition rate of amorphous layer (ZrCu) and nanocrystalline (Cu) is 0.343 nm/s and 0.2696 nm/s, respectively. These thin film metallic glasses were all prepared by magnetron sputtering with target of 101.6 mm (i.e., 4 inches) in diameter and at a working pressure of 4×10^{-3} torr. A rotary pump was used to achieve medium vacuum and a turbomolecular pump was used to achieve a base pressure less than 5×10^{-6} torr.

After achieving the base pressure lower than 1 × 10^{-5} torr, argon gas was then introduced into the chamber making working pressure (4 mtorr), and the Cu target and Zr target would be pre-sputtered for 5 minutes with moveable shutters in order to remove impurity on targets. Better depositing conditions can be achieved on the RF guns, but a lower depositing rate could be resulted on the RF gun. As the deposition rate is higher for Cu and nanocrystalline Cu layers need good deposition quality, the Zr target was set on the DC gun and the Cu target was set on the RF gun during depositing. For metallic glasses layer and nanocrystalline layers, the working power of sputter was set at different values. For coating amorphous layers composed of Zr and Cu, the RF gun was set to be 84 W and the DC gun was set to be 140 W; for coating nanocrystalline Cu layers, the RF gun was set 150 W. The substrate was placed on sample holder, 150 mm higher than the target, and was rotating with an average speed of 10 rpm for uniform distribution of the film thickness. The flow rate of working gas, pure argon, was fixed at 30 standard cubic centimeters per minute (sccm).

3-3 Property measurements and analyses

As the films are manufactured, the microstructure, morphology, crystal structure and mechanical property can be examined. The scanning electron microscope, energy dispersive X-ray spectrometry, and Mini-tester were used in this study.

3-3-1 SEM observations and constituent analysis

In this study, the JEOL ISM-6330 scanning electron microscope (SEM) was selected to characterize the microstructure and morphology of the manufactured film. The SEM is equipped with energy dispersive X-ray spectrometer (EDS), and we use it to identify the constituent component and confirm the composition percentage of the as-deposited thin film metallic glasses.

3-3-2 XRD analysis

The glassy nature of the as-deposited ZrCu thin films was characterized by X-ray diffractometer (XRD, Siemens D5000) with a monochromatic Cu-K_α radiation (λ = 0.15406 nm), a working voltage of 40 kV and electron current of 30 mA, equipped with 0.2 mm graphite monochromater. The diffraction angle (2θ) covers from 20° to 80° using a scanning rate of 0.05° per four seconds in the continuous mode.

3-3-3 Mechanical property analysis

The PI substrates deposited with metallic glass ZrCu and nanocrystaliyne Cu through 8 stainless masks with 3-size holes arranged as Figure 3.2. After removing the mask, the PI substrates were cut into a rectangle samples fully with deposited region. The deforming area is set as 12 mm × 3 mm, in the middle of squire samples as shown in Figure 3.3. The as-deposited PI right next to deposited region was also cut off, in order the confirm that the tensile test is set up right. The tensile test was carried out with MTS Tytron® 250 as shown in Figure 3.4. The strain rate is set to be 3×10^{-3} s^{-1}, and the whole displacement was controlled to be less than 2 mm. The datum processing method would be introduced in detail in section 4.5.

Chapter 4 Results and Discussion

4-1 Sample preparations

The magnetron sputtering deposition system in this study is equipped with three independent magnetron targets (two RF guns and one DC gun), but only one DC gun and one RF gun were used to deposit Zr and Cu. All samples with layered structures were deposited onto PI substrates and the thickness of each layer and the whole multilayers films is controlled by shutters on and off. In our general sense, the maximum limit in film thickness is approximately 2 μm in order to avoid the shrinkage of the tested samples, so the total thickness in this study is set to be 1 μm for all specimens.

Amorphous-crystalline multilayer films were alternatively deposited onto the PI substrate. In order to make the volume ratio between amorphous and nanocrystalline layers equal, the Cu layer was deposited at first then followed by the ZrCu layer, Cu layer, ZrCu layer, alternately. The first multilayered sample consists of 10 layers, that is to say, Cu/ZrCu/Cu…ZrCu/Cu/ZrCu, with the individual thickness of ZrCu amorphous layers being 100 nm and the Cu crystalline layers being 100 nm. The total film thickness of multilayer sample is 1 μm. The schematic drawing of the multilayer sample is shown in Figure 4.1(a).

The second multilayered sample consists of 14 layers with the individual thickness of ZrCu amorphous layers being 75 nm and the Cu crystalline layers being 75 nm. The total film thickness of second multilayer sample is 1.05 μm. The third sample is composed of 50-nm-thick Cu and ZrCu layers, and the total thickness of the third sample is 1 μm. The other two samples are composed of the same multilayered structure as mentioned above with thickness of 25 nm and 10 nm. The illustrations of the 50-nm-thick and 10-nm-thick sample are shown in Figures 4.1 (b) and (c), respectively. In this study, all samples have an amorphous as the top layer to ensure the initiation of shear bands from this layer and can also exhibit the property of amorphous alloy at the top surface. Also, thin films of monolithic crystalline Cu and monolithic amorphous ZrCu in thickness of 1 μm were also made for parallel study.

4-2 EDS analyses

The composition quantity analyses of the as-deposited thin films were characterized by SEM/EDS. For easy analyses, the amorphous film with 500 nm in thickness is deposited on the silicon nitride substrate under the same condition of coating amorphous layers on the PI substrates. The accelerating voltage for SEM/EDS is set in 10 kV, with 60 seconds life time. One of the EDS spectrums is shown in Figure 4.2. The composition data on the amorphous thin film is listed in Table 4.2. The average ratio between Zr and Cu in atomic percent in the amorphous thin film identified by SEM/EDS is $Zr_{46}Cu_{54}$, very close to the designed $Zr_{50}Cu_{50}$ goal.

4-3 XRD analysis

The crystal structure of the deposited thin films was characterized by XRD. Figures 4.3 to 4.9 shows the XRD patterns obtained from the thin films deposited on the

PI substrates. In Figure 4.3, there is no apparent sharp peak from 20° to 80°. The ZrCu amorphous diffuse hump between 35° to 45° can be observed. In Figure 4.4, the curve of pure Cu has shown the preferred orientation of Cu (111), crystalline peaks of (200) and (220) at 43.4°, 50.5° and 74.2°, respectively. The diffraction patterns of Figures 4.5 to 4.9 composed of ZrCu/Cu = (100 nm/100 nm,75 nm/75 nm, 50 nm/50 nm, 25 nm/25 nm, 10 nm/10 nm) show not only ZrCu amorphous diffuse peak in lower intensity, but the strongest peaks of Cu. As the thickness of ZrCu and Cu layer getting lower, the intensity of characteristic diffraction peaks of Cu become lower. It can barely to observe the peals of Cu (200) and (220) as the layer thickness falls in 10 nm, as shown in Figure 4.9. In Figure 4.10, the diffraction pattern of PI shows diffused peak in the ranges of 20° to 23°, 25° to 35° and 38° to 46°. Comparing Figure 4.10 and Figures 4.3 to 4.9, the diffused peak from 20° to 23° and 25° to 35° are attributed to the PI substrates.

The crystallite sizes of Cu can be obtained by Scherrer's formula:

$$t = \frac{0.9\lambda}{B\cos\theta_B} ,$$

(1)

where t, λ, B, θ_B are the diameter of crystallite, the X-ray wavelength, the full width at half maximum (FWHM) of diffraction peak and the Bragg angle, respectively. In this study, the FWHM of peaks of Cu (111) were measured after deducting the baseline of the diffraction curves. As the thickness become lower from 100 to 10 nm, the crystallite sizes of Cu become lower from ~30 nm down to ~5 nm, as shown in Figure 4.11. During the sputtering deposition, the grains of Cu become larger. As the thickness become larger, there was more time for Cu grains growing.

4-4 SEM film surface morphology characterization

The top layer of the as-deposited thin film is the amorphous ZrCu. The SEM surface morphology of ZrCu/Cu (100 nm/100 nm) samples is shown in Figures 4.12 to 4.15. Under low magnifications, the as-deposited sample showed a smooth surface, as illustrated in Figure 4.12. As the magnification increases to 3000X, the sphere-composed morphology can be observed, as shown in Figures 4.13 to 4.15. This morphology is consistent with the results of Raible et al. [69] on their amorphous $Zr_{65}Cu_{27.5}Al_{7.5}$.

The SEM surface morphologies of other thinner thickness of ZrCu/Cu (75 nm/75 nm), (50 nm/50 nm), (25 nm/25 nm), (10 nm/10 nm) are shown from Figures 4.16 to 4.36. At the low magnification, the samples of 75 nm to 10 nm in thickness show similar smooth surface morphology with some particles like ZrCu/Cu (100 nm/100 nm) samples. At higher magnification of 25000X and 50000X, the sphere domains can be observed as well. By contracting Figures 4.15, 4.20, 4.26, 4.31 and 4.36, the size of sphere domains become smaller as the thickness become smaller. These domains may contribute to the difference in mechanical properties, and affect the propagation of microcracks.

4-5 Mechanical property analysis

Before measuring the tensile mechanical properties, the stress concentration effect is needed to be considered, since that the tensile test is not set as traditional dog-bone shape. The clean PI samples were examined to find out whether the spacers will affect the mechanical properties. The stress-strain curves of PI with the Al spacers are shown in Figure 4.37. Clean PI samples stuck with the spacers stuck by the 3M^{TM} instant glue, the tradition double-sided tape and the 3M^{TM} V1805 double-sided tape were examined. Considering the mechanical properties of Kapton$^{®}$ FPC listed in Table 4.2, the theoretical values of the tensile modulus and the tensile strength are 2.8 GPa and 234 MPa, respectively. From these representative curves, the tensile moduli and maximum stress can be obtained and are listed in Table 4.3. All the experimental results are far below the theoretical value, and the one most close to the theoretical value is the PI sample without spacers and stuck with traditional double-sided tape. The effects of whether the spacers are used or how the spacers are stuck can be neglected in this experiment, so the spacers are not utilized in all tensile tests of this research.

The mechanical properties were examined by mini tensile testing. Since there has not been standard regulation on the thin film tensile testing, the reported method in reference of [38] is utilized in this study. The clean PI substrates were tested for more than ten times shown, as Figure 4.38, and then the curves are averaged and fitted with a fourth-order polynomial, with constraints:

$$\sigma\big|_{\varepsilon=0} = 0 \quad \text{and} \quad \frac{d\sigma}{d\varepsilon}\bigg|_{\varepsilon=0} = E_{PI}\,,$$

(2)

where σ, ε, E is stress, strain, tensile modulus, respectively. The result for the 50 μm PI foil is:

$$F = 15.88037\varepsilon - 321.25815\varepsilon^2 + 4043.95503\varepsilon^3 - 20346.30584\varepsilon^4,$$

(3)

where the F is tensile load in kgf and ε is in mm/mm. The polynomial form is used as reference and shown in Figure 4.39. The coated samples were then tested and the tensile property of the coated film is extracted by deducting the substrate reference. The deducting method had been utilized by Macionczyk and Brűckner [70]. The stress in the film is obtained by deducting the contribution of the PI substrate from the total load:

$$\sigma_{film} = \frac{1}{w_{film} t_{film}} (F_{total} - F_{Kpton}) ,$$

(3)

where σ_{film} is the tensile stress on the coated film, and w_{film}, t_{film}, F_{total}, F_{PI} are width and thickness of the coated film, the total applied force and the Kapton® force, respectively. The force on Kapton® is obtained by tensile testing of the clean PI substrate. The schematic illustration is shown in Figure 4.40.

4-5-1 Tensile properties analysis

In this study, the drformed area of coated foils is set in 12 cm × 3 cm, and the tensile tests are examined by Mini-Tester under uniform loading rate of 3×10^{-3} s^{-1}. The schematic engineering stress-strain curve of the monolithic amorphous ZrCu and monolithic nanocrystalline Cu thin films 1 μm in thickness are shown in Figures 4.41 and 4.42. The tensile moduli of the monolithic ZrCu and Cu thin films are 83 GPa and

104 GPa, respectively. This experimental value is close to the results from nano-indentation which are 93 GPa for ZrCu and 127 GPa for Cu [71-74].

The system is set in iso-strain model, so the total stress σ_t on specimens can be expressed as:

$$\sigma_t = \sigma_{film} + \sigma_{subs} = E_{film} \times \varepsilon + E_{subs} \times \varepsilon, \quad (5)$$

where σ_{film}, σ_{sub}, E_{film}, E_{sub} and ε are the stress on the coated film, the stress on the substrate, tensile moduli of the coated film, the tensile moduli of the substrates and total strain respectively. The experimental results show that the moduli of coated films is much higher than the moduli of substrates, so the stress acting on the coated films is greater than on the substrates. It would make the coated films experience more stress and showing lower moduli than the results from nano-indentation.

The theoretical value of the modulus of multilayered thin films can also be obtained from an iso-strain model of Rule of Mixture (ROM) as expressed by:

$$E_{multilayer} = (1 - f) \times E_{ZrCu} + f \times E_{Cu}, \quad (5)$$

where $E_{multilayer}$, E_{ZrCu}, E_{Cu} and f are tensile moduli of the multilayer thin films, ZrCu TFMG films, crystalline Cu thin films and the volume fraction of the crystalline Cu layer in the multilayer thin films, respectively. In this research, the volume fraction is set as the same, so the theoretical value of the modulus can be calculated by ROM as 94 GPa (i.e., 1/2 × 83 GPa + 1/2 × 104 GPa). The maximum stress, σ_{max}, can be obtained in the same form. The experimental value of σ_{max} of ZrCu and Cu 1 μm in thickness are 612 MPa and 570 MPa, according to ROM, so the theoretical ROM stress value of the multilayer thin films should be 591 MPa.

The representative engineering stress-strain curve in about 2% strain of TFMG ZrCu and crystalline Cu monolayer thickness in 100 nm/100 nm, 75 nm/75 nm, 50 nm/50, 25 nm/25 nm and 10 nm/10 nm are shown in Figures 4.43 to 4.47. The moduli of these samples are in the range of 87 ± 10 GPa, close to 94 GPa of the ROM result. The influence of the monolayer thickness on modulus is not very significant, as shown in Figure 4.48. The Young's modulus is a value of intrinsic property, and is hard to be affected by experimental conditions. This result is reasonable and predictable.

The maximum stresses of 100 nm/100 nm, 75 nm/75 nm, 50 nm/50 nm, 25 nm/25 nm and 10 nm/10 nm are 550 ± 20 MPa, 765 ± 30 MPa, 740 ± 12 MPa, 1030 ± 15 MPa and 540 ± 10 MPa, respectively. For the clarity of presentation, all the results of maximum stresses are shown in Figure 4.49. This phenomenon can be associated with the Hall-Petch relation for multilayered materials [75]. The Hall-Petch relation for multilayered materials can be obtain by the linear fitting of the maximum stresses thickness in the range of 25 nm to 100 nm, which is shown in Figures 4.50. The linear fitted equation is:

$$\sigma = 186.58663 + 4091.73755 \times h^{-1/2}, \text{ and } R^2 = 0.94867, \quad (6)$$

while σ, h and R are the maximum stresses, thickness and the correlation coefficient, respectively. As the thickness of Cu is in the range of 25 nm to 100 nm, the deformation is made by dislocation pile up. Here the thickness can be seen as the grain sizes in Hall–Petch equation, as the smaller of thickness, the stronger of the monolayers. On the other hand, the deformation mechanism of amorphous ZrCu layers is shear band transmition, which is less sensitive of dimension in thickness in the range of 10 nm to 100 nm. The decreases in thickness would barely affect the mechanical properties of amorphous monolayers. According to equation (5), the layers with lower modulus would experience lower stress. During the deformation, the crystalline Cu layers deform first and turn into plastic deformation before the amorphous ZrCu layers, but the ZrCu layers would fracture earlier than Cu layers in elastic deformation, as shown in Figure 4.51. So, the deformation behavior of Cu layers becomes very important. That is, if Cu layers become tougher, the total thin film would be strengthened.

If the thickness is too small (10 nm/10 nm) for dislocation pile-up, the deformation mechanism of multilayered thin film would turn into interface gliding. In this time, the mismatch of interface would play an important role. The mismatch between metallic glass and nanocrystalline metal is very small, so it can hardly to obstruct the gliding. It leads to the lowest stress for the 10 nm/10 nm specimens.

The yield stresses and yield strain of the multilayered thin films are shown in Figures 4.52 and 4.53. The ZrCu/Cu (25 nm/25 nm) multilayered thin films have the largest yield stress and yield strain. As mentioned in last paragraph, the Cu layers deform earlier than ZrCu layers. At lower layer thickness the formation of dislocations in Cu layers is not easy to happen. On the other hand, amorphous metals often have higher elasticity. Higher strain and stress is needed to activate plastic deformation of Cu owing to the changes of elastic mechanical properties of Cu layers.

4-5-2 SEM fracture surface morphology analysis

The deformation of the PI substrate would directly influence the mechanical behavior of the coated thin films, so the uncoated PI substrate was first examined by SEM. In Figure 4.54 and 4.55, the crack pattern in uncoated and tensile-loaded PI is not observed. The tensile tests are progressed in the elastic region of PI substrates, so we can assume that the PI substrate remains flat in the whole tensile experiments. The deformed SEM surface morphology reveals this assumption.

In the observation of monolithic amorphous ZrCu and nanocrystalline Cu deformed surface morphology shown in Figures 4.56 to 4.59, the different crack types can be seen. At a low magnification of 350X, the surface is composed of parallel microcracks, as Figure 4.56 and 4.58. In Figure 4.57, the monolithic amorphous ZrCu specimen observed at magnification of 1000X, the straight microcracks are contributed by direct gliding of shear bands. In Figure 4.59, the monolithic crystalline Cu film shows zig-zag microcracks owing to dislocations sliding. The zig-zag or straight form of microcracks could be linked with the resistance of microcracks propagation.

Figures 4.60 to 4.63 show the SEM surface morphology of the deformed ZrCu/Cu (100 nm/100 nm) multilayer sample at magnifications of 350X, 1500X, 5000X and 15000X. Most of microcracks perpendicular to the tensile loading direction can be observed in these figures. Microcracks will propagate along the sphere domains, as shown in Figure 4.60 and 4.61. The perpendicular microcracks can also be observed in the ZrCu/Cu (50 nm/50 nm), ZrCu/Cu (25 nm/25 nm) and (10 nm/10 nm) multilayer samples at magnifications of 350X, 1500X and 5000X, shown in Figures 4.64 to 4.73.

By comparing the deformed surface morphologies of multilayered thin films at 5000X in magnification, the spacing in cracks can be analyzed qualitatively. The spacing in cracks of ZrCu/Cu (100 nm/100 nm), (50 nm/50 nm) and (10 nm/10 nm) are about 125 nm, 53 nm and 88 nm, respectively, and the spacing in crack of ZrCu/Cu (100 nm/100 nm) multilayered samples can not be clearly observed. The specimens were deformed at near strain, so the spacing in the cracks can be linked with the resistance of the accumulation of cracks or elasticity. The 25 nm in thickness samples have the largest resistance owing to the cracks can barely separate. This result agree with the result of yield strain shown in Figure 4.53.

The crack spacing on the surface could represent the toughness of the specimens. The schematic illustration of average crack spacing of the ZrCu/Cu (100 nm/100 nm), ZrCu/Cu (50 nm/50 nm), ZrCu/Cu (25 nm/25 nm) and ZrCu/Cu (10 nm/10 nm) is shown in Figure 4.74. The crack density can be calculated by taking the average spacing into reciprocal. The crack density of large strain for the 10% are smaller than that after 2% strain, as shown in Figure 4.78. It means that the crack density would accumulate until a saturated value. The crack density is the minor in the sample of ZrCu/Cu (25 nm/25 nm), and encreases along both sides of decreasing or increasing thickness. This is exactly the same as the examination of the maximum stress shown in Figure 4.49.

For clearly representation, the curves of crack densities of 2% strain versus the maximum stresses and yield stresses of different thickness samples are shown in Figure 4.76. The higher of the crack density is, the lower of the maximum stresses and yield stresses are. The most strengthened multilayered thin films of ZrCu/Cu (25 nm/25 nm) would exhibit the least crack density.

Chapter 5 Conclusion

The tensile behavior of the monolithic amorphous ZrCu and crystalline Cu thin films and the ZrCu/Cu multilayered thin films in different monolayer thicknesses has been investigated. The following conclusions can be obtained from the experimental results.

1. The morphology of as-deposited thin film of ZrCu/Cu (100 nm/100 nm) is composed of sphere domains, and between the domains there would be stress concentration. The cracks perpendicular to the loading direction would propagate along the domain interface.

2. The tensile moduli of monolithic amorphous ZrCu and crystalline Cu thin films are closed to results from micro-compression (93 and 127 GPa).

3. The stress-strain curves of the multilayered ZrCu/Cu thin film, extracted by deducting the curves of the uncoated PI substrate from the coated samples are compatible with the theoretically rule of mixture prediction.

4. As the layer thickness going down from 100 nm to 10 nm, the tensile moduli would not change too much. The current study demonstrates that the nanolaminate of ZrCu/Cu (25/25 nm) can reach the highest maximum stress (1030 MPa) among all samples.

References

[1] W. Klement, R. H. Willens and P. Duwez, Nature, 187, pp. 869-870 (1960).

[2] A.C. Lund and C. A. Schuh, J. Appl. Phys., 95, pp. 4815-4822 (2004).

[3] W. L. Johnson, MRS Bull. 24, pp. 42-56 (1999).

[4] A. Inoue. Acta Mater. 48, pp. 279-306 (2000).

[5] H. S. Chou, J. C. Huang, Y. H. Lai, L. W. Chang, X. H. Du, J. P. Chu and T. G. Nieh, J. Alloy Compd., 483, pp. 341-345 (2009).

[6] B. Golding, B. G. Bagley and F. S. L. Hsu, Phys. Rev. Lett., 29, pp. 68-70 (1972).

[7] S. K. Sharma, S. Hofmann, Appl. Surf. Sci., 51, pp. 139-155 (1991).

[8] A. Calka, A. P. Pogany,R. A. Shanks and H. Engelman, Mat. Sci. Eng. A., 128, pp. 107-112 (1990).

[9] X. H. Du, J. C. Huang, H. M. Chen, H. S. Chou, Y. H. Lai, K. C. Hsieh, J. S. C. Jang and P. K. Liaw, Intermetallics, 17, pp. 607-613 (2009).

[10] Y. Wang, J. Li, A. V. Hamza and T. W. Barbee, Proc. Natl. Acad. Sci. U. S. A., 104, pp. 11155–11160 (2007).

[11] D. W. Forester, C. Vittoria, D. C. Webb and K. L. Davis, J. Appl. Phys., 49, pp. 1794-1796 (1978).

[12] R. B. Schwarz and W. L. Johnson, Phys. Rev. Lett., 51, pp. 415-418 (1983).

[13] E. J. Cotts, W. J. Meng and W. L. Johnson., Phys. Rev. Lett., 57, pp. 2295-2298 (1986).

[14] Q. M. Chen, Y. D. Fan and H. D. Li., Mater. Lett., 6, pp. 311-315 (1988).

[15] G. Minnigerode, A. Regenbrecht and K. Samwer, Z. Phys. Chem. Neue Folge, Bd., 157, pp. 197-201 (1988).

[16] A. Regenbrecht, G. Minnigerode and K. Samwer, Z. Phys. B, 79, pp. 25-31 (1990).

[17] J. Dudonis, R. Brucas and A. Miniotas, Thin Solid Films, 275, pp. 164-167 (1996).

[18] S. Hata, K. Sato and A. Shimokohbe, Proc. SPIE, 3892, pp. 97-108 (1999).

[19] Y. Liu, S. Hata, K Wata and A. Shimokohbe, Jpn. J. Appl. Phys., 40, pp. 5382-5388 (2001).

[20] Y. Liu, S. Hata, K. Wada and A. Shimokohbe, Interlaken, Switzerland, MEMS 14th IEEE International Conference (2001).

[21] J. P. Chu, Y. W. Lai, T. N. Lin and S. F. Wang, Mat. Sci. Eng. A, 277, pp. 11-17 (2000).

[22] D. S. Grummon and J. Zhang, Phys. Stat. Sol. A, 186, pp. 17-39 (2001).

[23] P. Hashemi, J. Derakhshandeh, S. Mohajerzadeh, M. Robertson and A. Tonita, J. Vac. Sci. Technol. A, 22, pp. 966-970 (2004).

[24] T. G. Nieh and J. Wadsworth, Scripta Mater., 44, pp. 1825-1830 (2001).

[25] Y. Xiang, T. Li, Z. Suo and J. J. Vlassak, Appl. Phys. Lett., 87, 161910 (2005).

[26] R. M. Niu, G. Liu, C. Wang, G. Zhang, X. D. Ding and J. Sun, Appl. Phys. Lett., 90, 161907 (2007).

[27] S. R. Forrest, Nature, 428, pp. 911-918 (2004).

[28] A. Rogers, Z. Bao, K. Baldwin, A. Dodabalapur, B. Crone, V. R. Raju V. Kuck, H. Katz, K. Amundson, J. Ewing and P. Drzaic, Proc. Natl. Acad. Sci. U.S.A. 98, pp. 4835-4840 (2001).

[29] V. J. Lumelsky, M. S. Shur and S. Wagner, IEEE Sens. J., 1, pp. 41-51 (2001).

[30] Bonderover and S. Wagner, IEEE Electron Device Lett., 25, pp. 295-297 (2004).

[31] B. C. Bell and D. A. Glocker, J. Vac. Sci. Tech. A, 9, pp. 2437-2441 (1991).

[32] H. C. Choi and K. S. Kim, J. Mech. Phys. Solids, 40, pp. 75-103 (1992).

[33] Y. S. Kang and P. S. Ho, J. Electron. Mater., 26, pp. 805-813 (1997).

[34] F Macionczyk, W Brűckner, W Pitschte and Reiss, J. Mater. Res., 13, pp.

2852-2858 (1998).

[35] H. Gleskova, S. Wagner and Z. Suo, Appl. Phys. Lett., 75, pp. 3011-3013, (1999).

[36] O. Kraft, R. Schwaiger and P. Wellner, Mater. Sci. Eng. A., 319, pp. 919-923 (2001).

[37] K. F. Badawi, P Villain, P Goudeau and P. O. Renault, Appl. Phys. Lett., 80, pp. 4705-4707 (2002).

[38] D. Y. W. Yu and F. Spaepen, J. Appl. Phys., 95, pp. 2991-2997 (2004).

[39] J. Das, M. B. Tang, K.B. Kim, R. Theissmann, F. Baier, W. H. Wang and J. Eckert, Phys. Rev. Lett., 94, 205501 (2005).

[40] Y. H. Liu, G. Wang, R. J. Wang, D. Q. Zhao, M. X. Pan and W. H. Wang, Science, 315, pp. 1385-1388 (2007).

[41] J. C. Lee, Y. C. Kim, J. P. Ahn and H.S. Kim, Acta Mater., 53, pp. 129-139 (2005).

[42] K. Oka, N. Yano, S. Furukawa, I. Ogasawara, J. Yamasaki and F. B. Humphrey, IEEE Trans. Mag., 31, pp. 3997-3999 (1995).

[43] J. Sakurai, S. Hata, and A. Shimokohbe, International Conference on Advanced Technology in Experimental Mechanics 2003, pp. 10-12 (2003).

[44] Y. Liu, S. Hata, K Wada and A. Shimokohbe, Jpn. J. Appl. Phys., 40, pp. 5382-5388 (2001).

[45] S. J. Poon, Adv. Phys., 41, pp. 303-363 (1992).

[46] S. R. Nagel, Phys. Rev. Lett., 41, pp. 990-993 (1978).

[47] J. P. Chu, C. T. Lo, Y. K. Fang and B. S. Han, Appl. Phys. Lett., 88, pp. 1-3 (2006).

[48] O. J. Kwon, Y. C. Kim, K. B. Kim, Y. K. Lee and E. Fleury, Met. Mater. Int., 12, pp. 207-212 (2006).

[49] A. J. Kerns, D. E. Polk, R. Ray and B. C. Giessen, Mat. Sci. Eng. A., 38, pp. 49-53 (1979).

[50] K. H. J. Buschow, J. Appl. Phys. 52, pp. 3319-3323 (1981).

[51] Z. Altounian, G. H. Tu and J. O. Strom-Olsen, J. Appl. Phys. 53, pp. 4755-4760 (1982).

[52] E. Kneller, Y. Khan and U. Gorres, Z. Metallkd. 77, pp. 152-163 (1986).

[53] I. Karaman, J. Robertson, J. T. Im, S. N. Mathaudhu, Z. P. Luo and K. T. Hartwig, Metall. Mater. Trans. A, 35A, pp. 247-256 (2004).

[54] F. Spaepen, Acta Matall. 25, pp. 407-415 (1977).

[55] A. S. Argon, Acta Matall. 27, pp. 47-58 (1979).

[56] L. H. Dai, M. Yan, L. F. Liu and Y. L. Bai, Appl. Phys. Lett. 87, 141916 (2005).

[57] S. Iwamori, T. Miyashita, S. Fukuda, S. Nozaki, K. Sudoh and N. Fukuda, Vacuum, 51, pp. 615-618 (1998).

[58] 林金雀, 化工資訊, pp. 29-34 (1998).

[59] T. Strunskus, M. Grunze, G. Kochendoerfer and C. Woll, Langmuir, 12, pp. 2712-2725 (1996).

[60] D. A. Hardwick, Thin Solid Films, 154, pp. 109-124 (1987).

[61] M. D. Merz and S. D. Dahlgren, J. Appl. Phys., 46, pp. 3235-3237 (1975).

[62] R. W. Springer and D. S. Catlett, Thin Solid Films, 54, pp. 197-205 (1978).

[63] C. A. Neugebauer, J. Appl. Phys., 31, pp. 1096-1101 (1960).

[64] D. Kuhlmann-Wilsdorf and K. S. Raghavan, Rev. Sci. Instrum., 33, pp. 930-933 (1962).

[65] J. M. Blakely, J. Appl. Phys., 35, pp. 1756-1759 (1964).

[66] A. Lawley and S. Schuster, Sci. Insfrum. Res., 3, pp. 1178-1180 (1962).

[67] C. G. Andeen, C. W. Hagerling and R. W. Hoffman, Proc. 7th. Int. Vacuum Congr. and 3rd Int. Conf. on Solid Surf., Vienna, Austria, pp. 1769-1772 (1977).

[68] I. C. Lin, Master Thesis, pp. 67-68 (2010).

[69] M. Raible, S. J. Linz and P. Hänggi, Phys. Rev. E, 64, 031506 (2001).

[70] F. Macionczyk and W. Brűckner, J. Appl. Phys., 86, pp. 4922-4929 (1999).

[71] M. C. Liu, J. C. Huang, H. S. Chou, Y. H. Lai and T. G. Nieh, Scripta Materialia, 61, pp. 840-843 (2009).

[72] M. C. Liu, C. J. Lee, Y. H. Lai and J. C. Huang, Thin Solid Films , 518, pp. 7295-7299 (2010).

[73] G. W. Nieman, J.R. Weertman, and R. W. Siegel, J. Mat. Res, 6, pp. 1012-1027 (1991).

[74] H. D. Espinosa, B.C. Prorok, and B. Peng, J. Mech. Phys., 52, pp. 667-689 (2004).

[75] P. M. Anderson, C. Li, Nanostructered Mater., 5, pp. 349-362 (1995).

[76] J. Y. Zhang, X. Zhang, G. Liu, G.J. Zhang and J. Sun, Scripta Mater., 63, pp. 101–104 (2010).

[77] X. F. Zhu, G.P. Zhang, C. Yan, S.J. Zhu and J. Sun, Philos. Mag. Lett., 90, pp. 413–421 (2010).

Table 1.1 Fundamental properties and application fields of bulk amorphous and nanocrystalline alloys [4].

Fundamental characteristic	Application field
High strength	Machinery structural materials
High hardness	Optical precision materials
High fracture toughness	Die materials
High impact fracture energy	Tool materials
High fatigue strength	Cutting materials
High elastic energy	Electrode materials
High corrosion resistance	Corrosion resistant materials
High wear resistance	Hydrogen storage materials
High viscous flowability	Ornamental materials
High reflection ratio	Composite materials
Good soft magnetism	Writing appliance materials
High frequency permeability	Sporting goods materials
High magnetostriction	Bonding materials
Efficient electrode (Chlorine gas)	Soft magnetic materials
High hydrogen storage	High magnetostrictive materials

Table 2.1 Electrical resistivity of the thin film metallic glasses and conventional electricaldevice materials [43].

	Thin film metallic glass			Cu	W
	$Pd_{76}Cu_6Si_{18}$	$Zr_{75}Cu_{19}Al_6$	$Cu_{60}Zr_{40}Ti_{10}$		
Electrical resistivity (μ Ω cm)	62	160	216	1.5	4.9

Table 2.2 Dipole screening and localization energies [59].

metal	atomic radius[63] (nm)	polarizability[64] (nm^3)	dipole screening ΔA (%)	localization energy (kJ/mol)
Cu	0.128	0.0061	53	5
Ag	0.144	0.0072	53	4
Au	0.144	0.0058	44	3
Pd	0.137	0.0048	40	3
Cr	0.128	0.0116	84	10

Table 2.3 Mechanical testing techniques: advantage and liabilities [60].

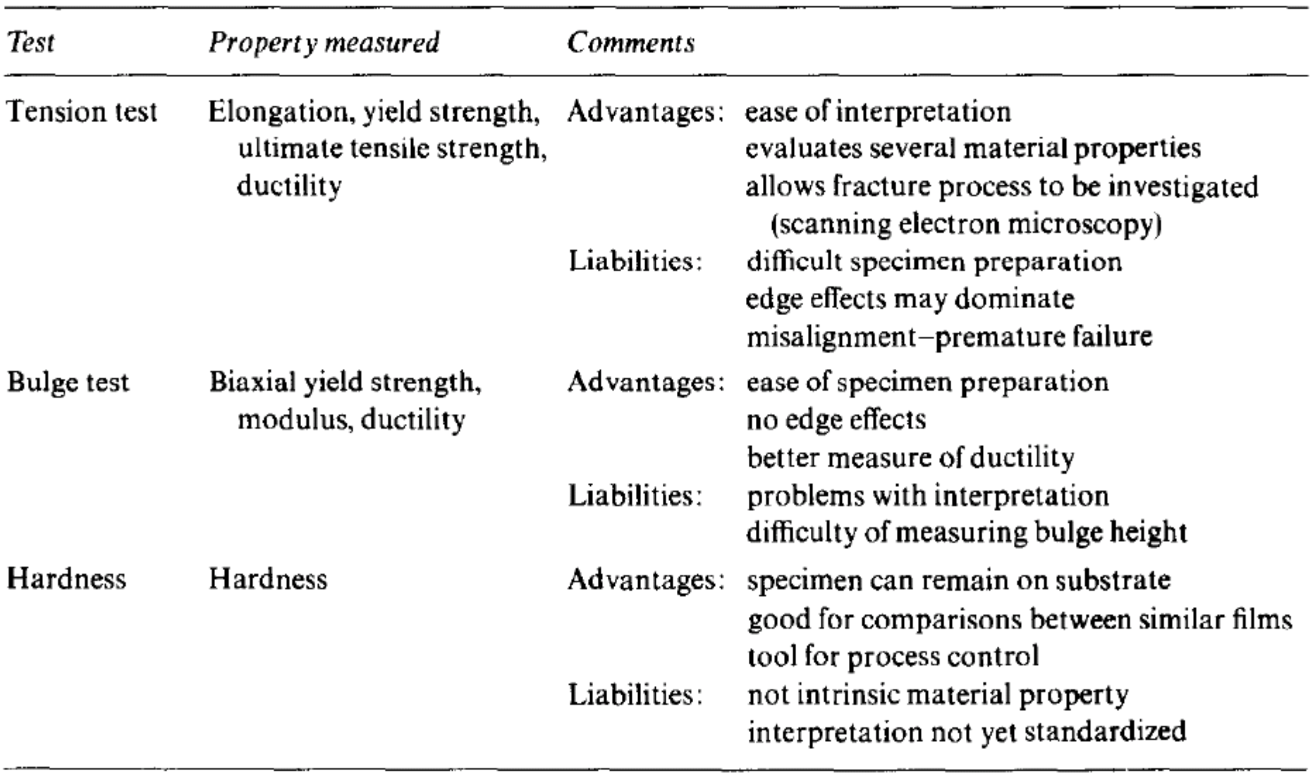

Test	*Property measured*	*Comments*	
Tension test	Elongation, yield strength, ultimate tensile strength, ductility	Advantages:	ease of interpretation evaluates several material properties allows fracture process to be investigated (scanning electron microscopy)
		Liabilities:	difficult specimen preparation edge effects may dominate misalignment–premature failure
Bulge test	Biaxial yield strength, modulus, ductility	Advantages:	ease of specimen preparation no edge effects better measure of ductility
		Liabilities:	problems with interpretation difficulty of measuring bulge height
Hardness	Hardness	Advantages:	specimen can remain on substrate good for comparisons between similar films tool for process control
		Liabilities:	not intrinsic material property interpretation not yet standardized

Table 4.1 The composition quantity analysis of ZrCu amorphous thin film characterized by EDS.

element	Composition (in atomic percent)				
	1	2	3	4	Avg.
Cu	53.63	52.54	53.08	53.63	53.22
Zr	46.37	47.46	46.92	46.37	46.78

Table 4.2 Typical Properties of Kapton® FPC at 23 °C (73°F)

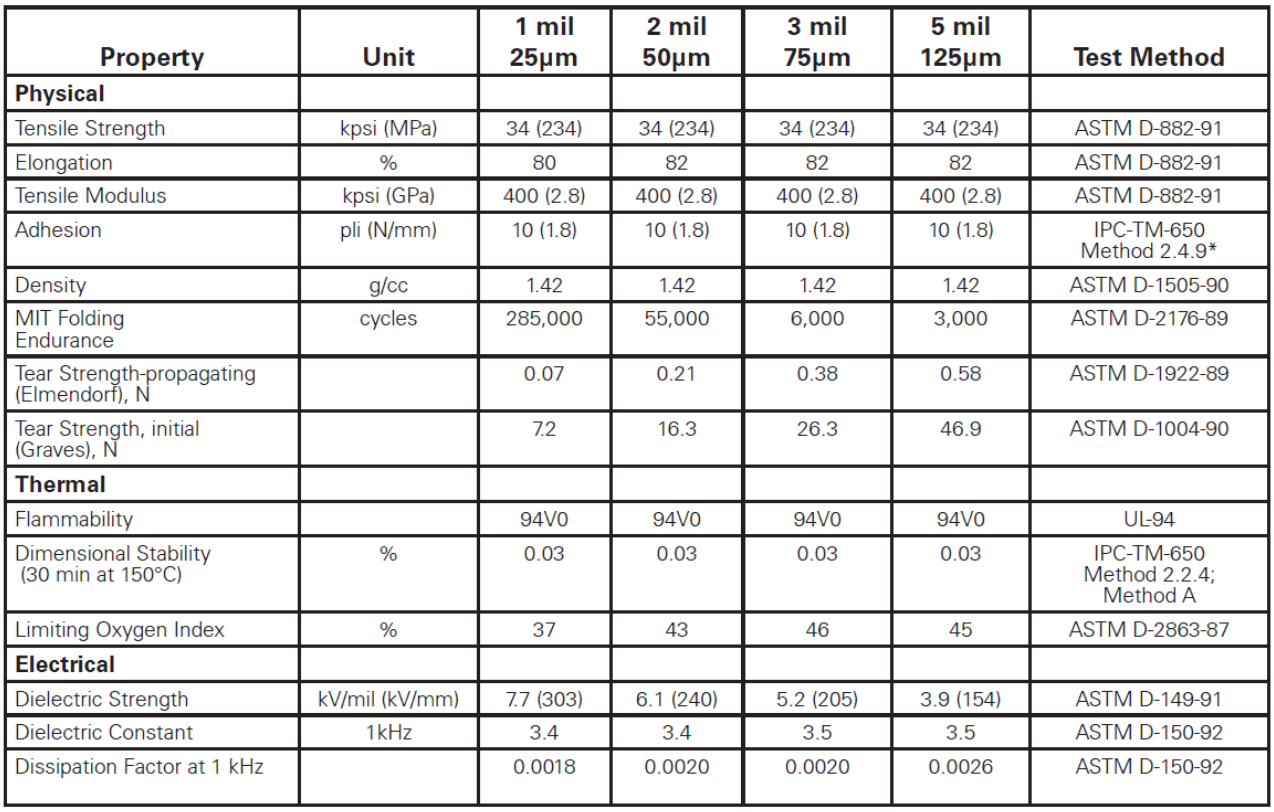

Property	Unit	1 mil 25µm	2 mil 50µm	3 mil 75µm	5 mil 125µm	Test Method
Physical						
Tensile Strength	kpsi (MPa)	34 (234)	34 (234)	34 (234)	34 (234)	ASTM D-882-91
Elongation	%	80	82	82	82	ASTM D-882-91
Tensile Modulus	kpsi (GPa)	400 (2.8)	400 (2.8)	400 (2.8)	400 (2.8)	ASTM D-882-91
Adhesion	pli (N/mm)	10 (1.8)	10 (1.8)	10 (1.8)	10 (1.8)	IPC-TM-650 Method 2.4.9*
Density	g/cc	1.42	1.42	1.42	1.42	ASTM D-1505-90
MIT Folding Endurance	cycles	285,000	55,000	6,000	3,000	ASTM D-2176-89
Tear Strength-propagating (Elmendorf), N		0.07	0.21	0.38	0.58	ASTM D-1922-89
Tear Strength, initial (Graves), N		7.2	16.3	26.3	46.9	ASTM D-1004-90
Thermal						
Flammability		94V0	94V0	94V0	94V0	UL-94
Dimensional Stability (30 min at 150°C)	%	0.03	0.03	0.03	0.03	IPC-TM-650 Method 2.2.4; Method A
Limiting Oxygen Index	%	37	43	46	45	ASTM D-2863-87
Electrical						
Dielectric Strength	kV/mil (kV/mm)	7.7 (303)	6.1 (240)	5.2 (205)	3.9 (154)	ASTM D-149-91
Dielectric Constant	1kHz	3.4	3.4	3.5	3.5	ASTM D-150-92
Dissipation Factor at 1 kHz		0.0018	0.0020	0.0020	0.0026	ASTM D-150-92

Table 4.3 Tensile mechanical properties of clean PI stuck with the spacers stuck by the the tradition double-sided tape, 3M^{TM} instant glue and the 3M^{TM} V1805 double-sided tape.

Sticking material	**Tensile modulus (MPa)**	**Maximum stress (MPa)**
No spacers	712	42
Tradition double-sided tape	634	43
3M^{TM} instant glue	641	28
3M^{TM} V1805 double-sided tape	375	28

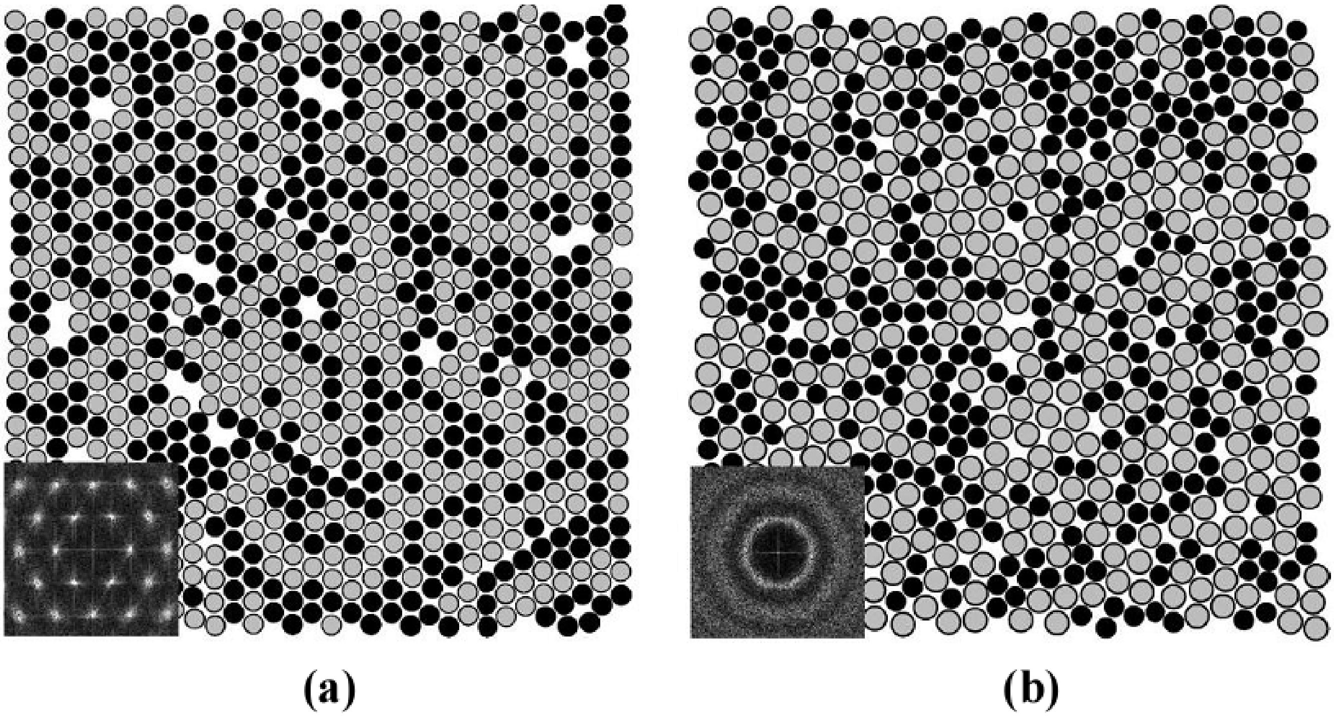

Figure 1.1 Two typical arrangement of atomic structures in (a) crystal and (b) amorphous alloy. The inset Fourier transforms in left corner shows the structural differences [2].

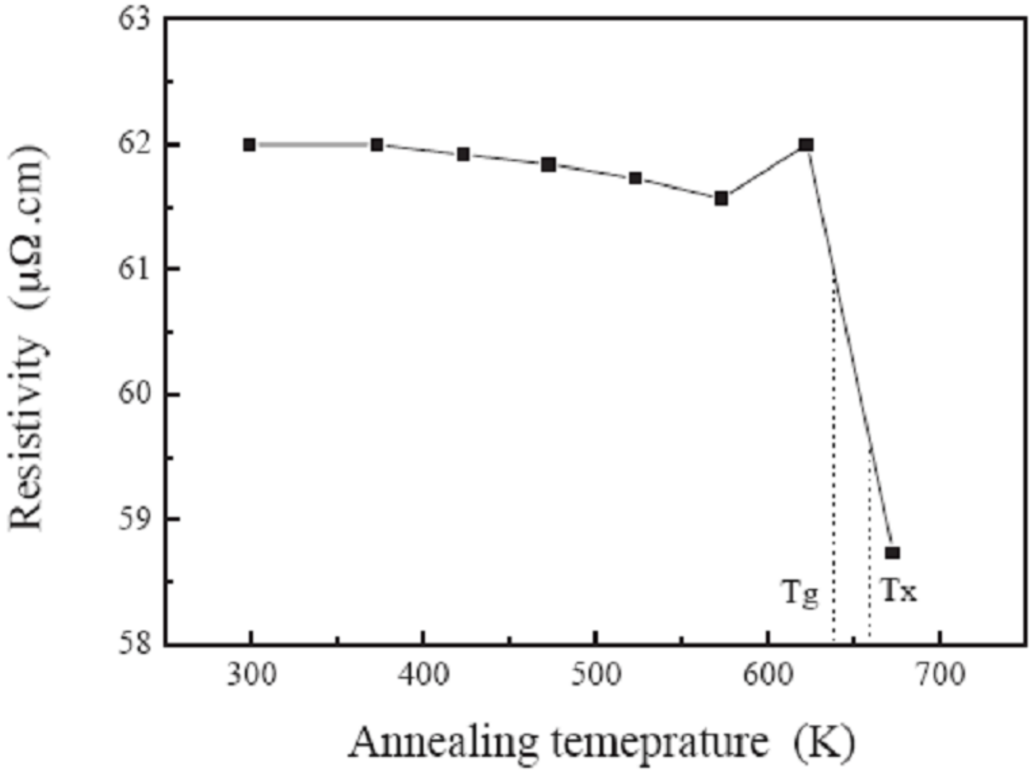

Figure 2.1 Resistivity as a function of annealing temperature of Pd-TFMG [44].

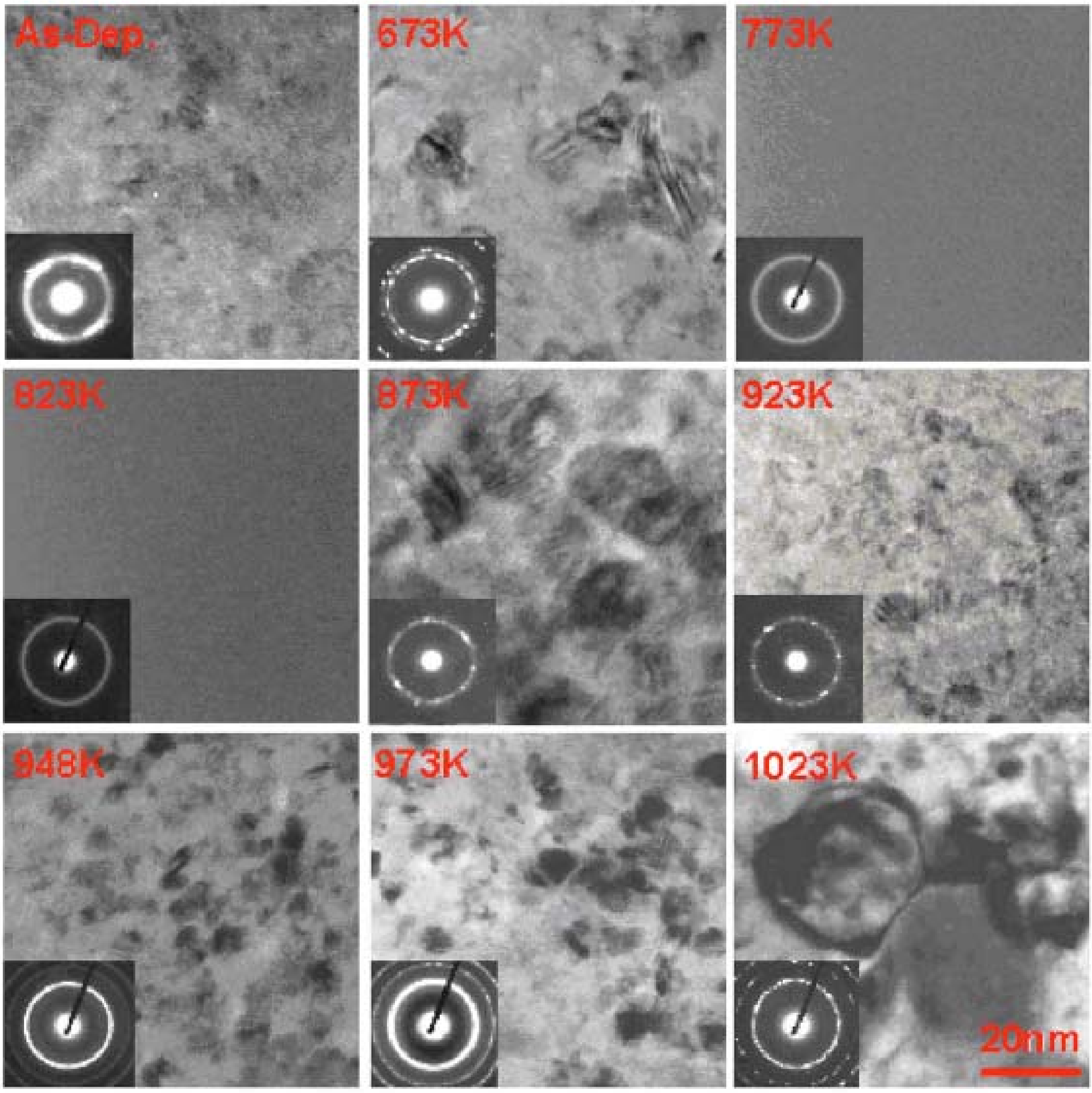

Figure 2.2 TEM bright-field images and diffraction patterns of films in asdeposited and annealed conditions [47].

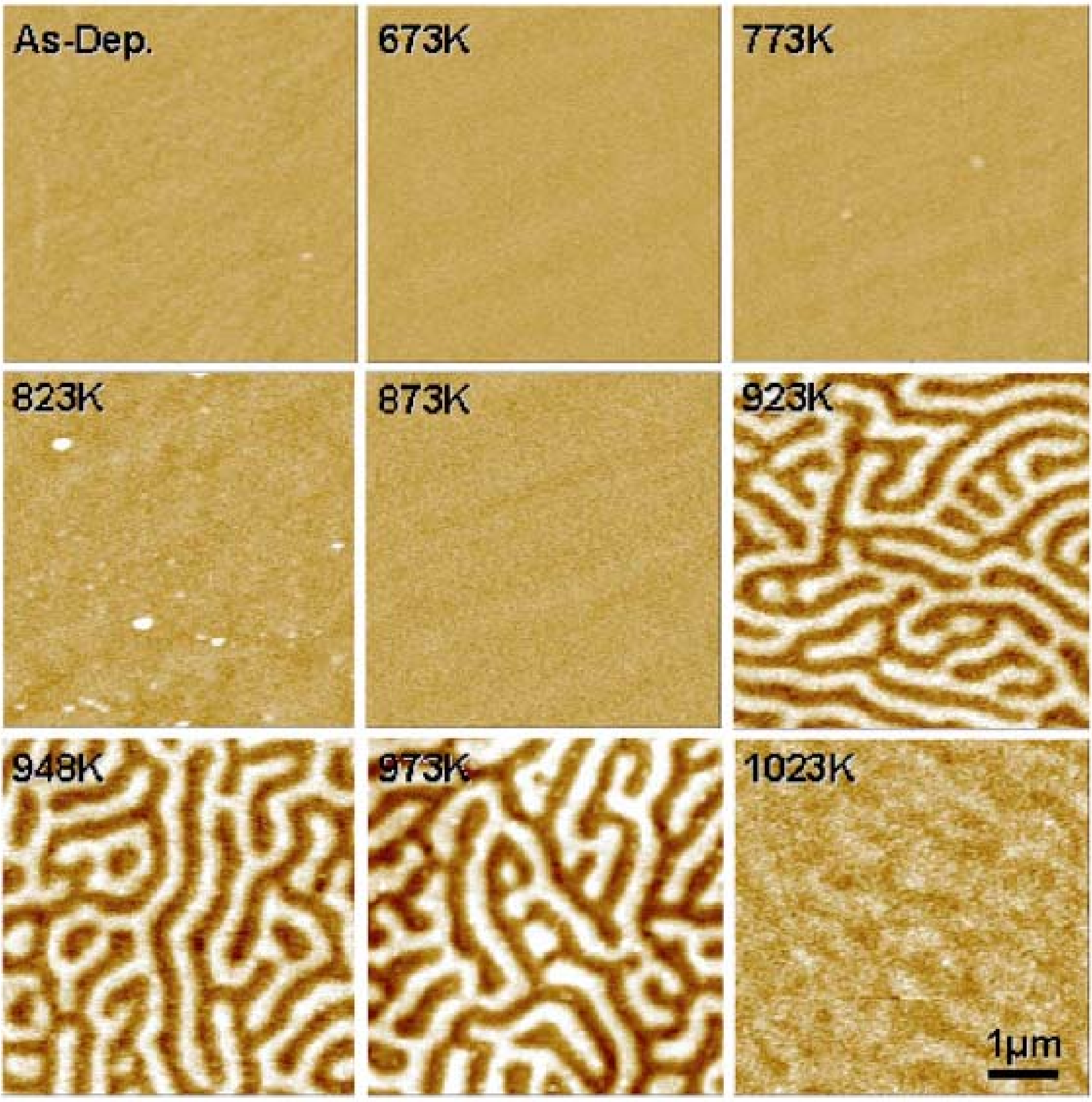

Figure 2.3 Magnetic force microscopy images of films in asdeposited and annealed conditions [47].

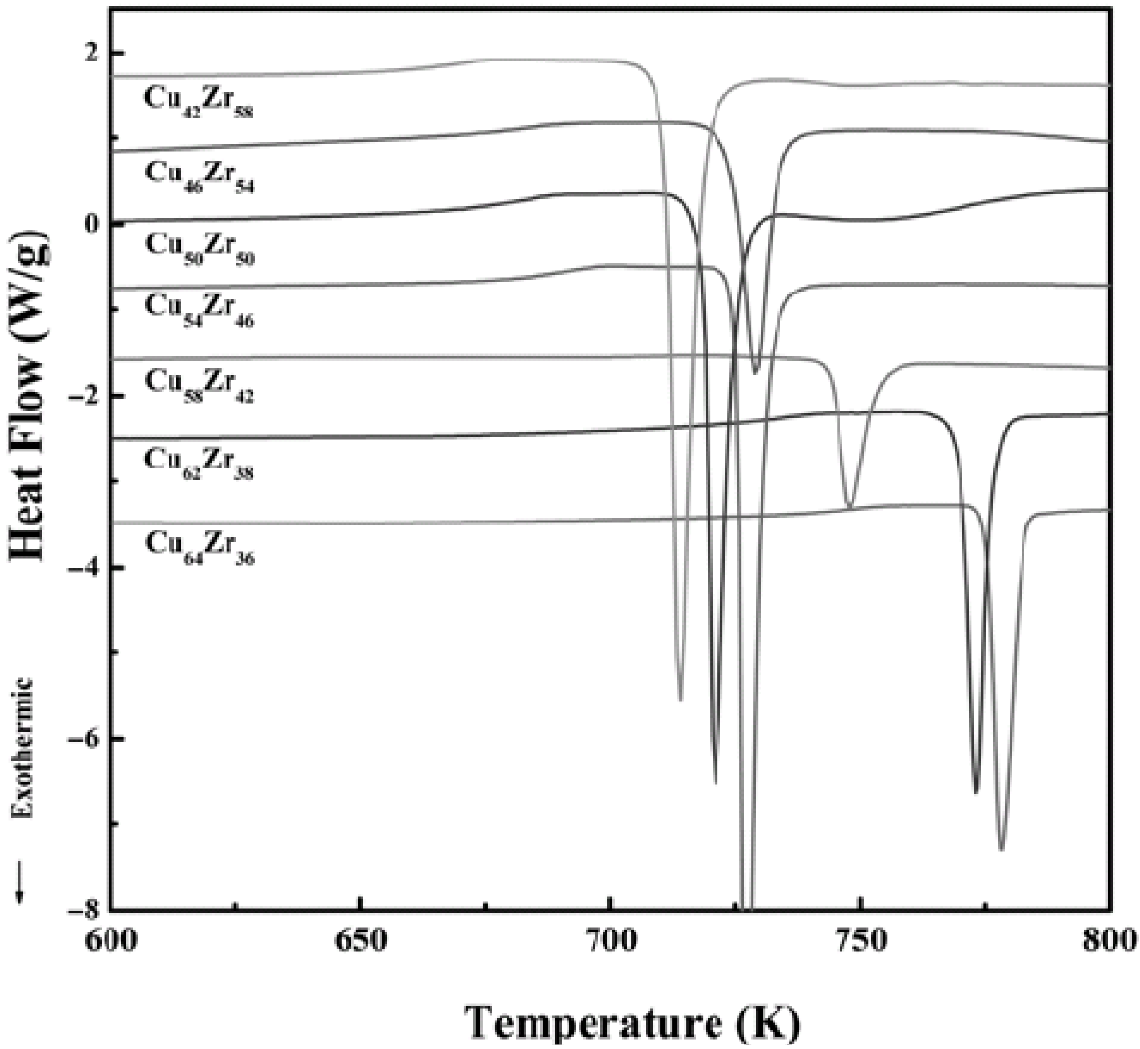

Figure 2.4 DSC traces of the Φ1 mm rods for compositions ranging from $Cu_{40}Zr_{60}$ to $Cu_{66}Zr_{34}$ [48].

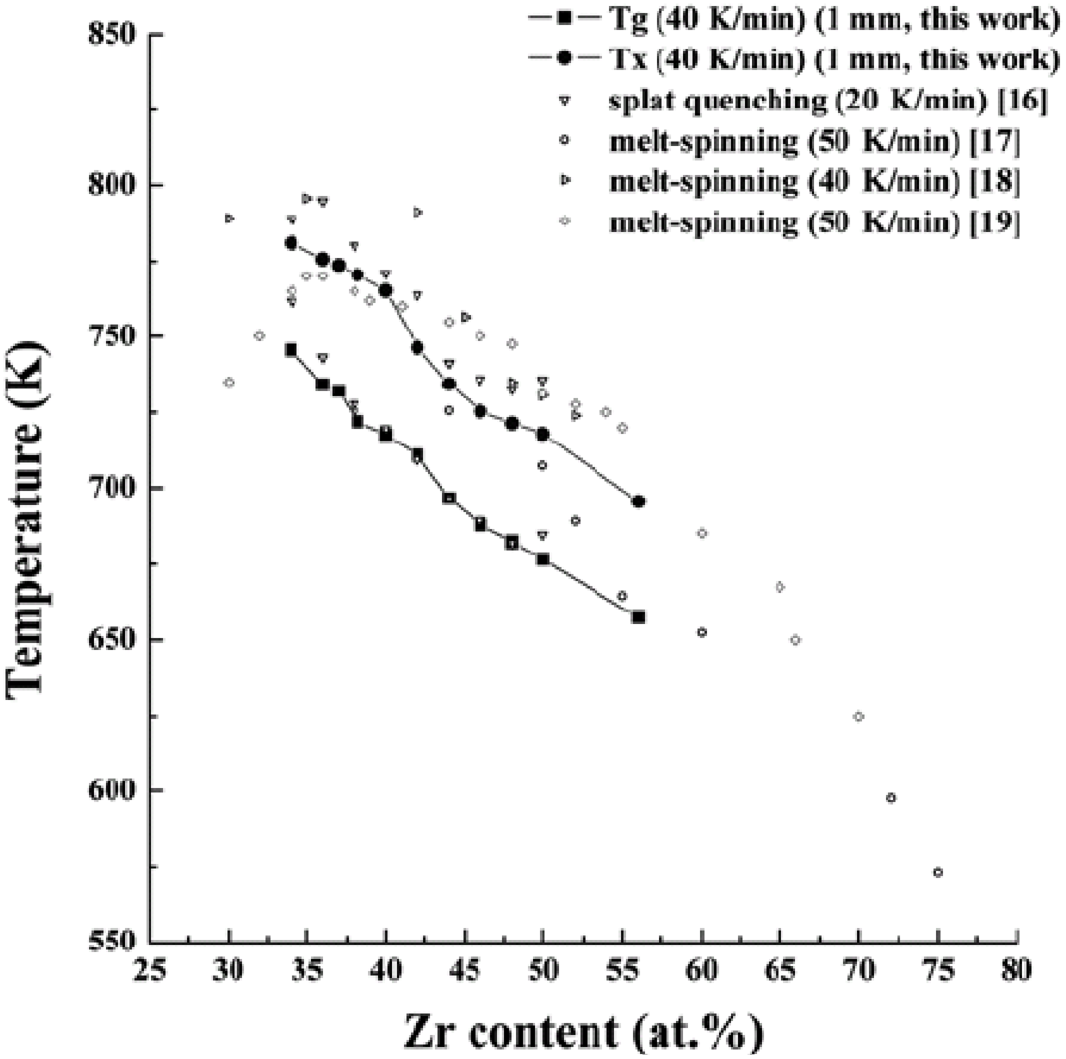

Figure 2.5 Variation of the glass transition and crystallization temperature with the Zr content [48, 49, 50, 51, 52].

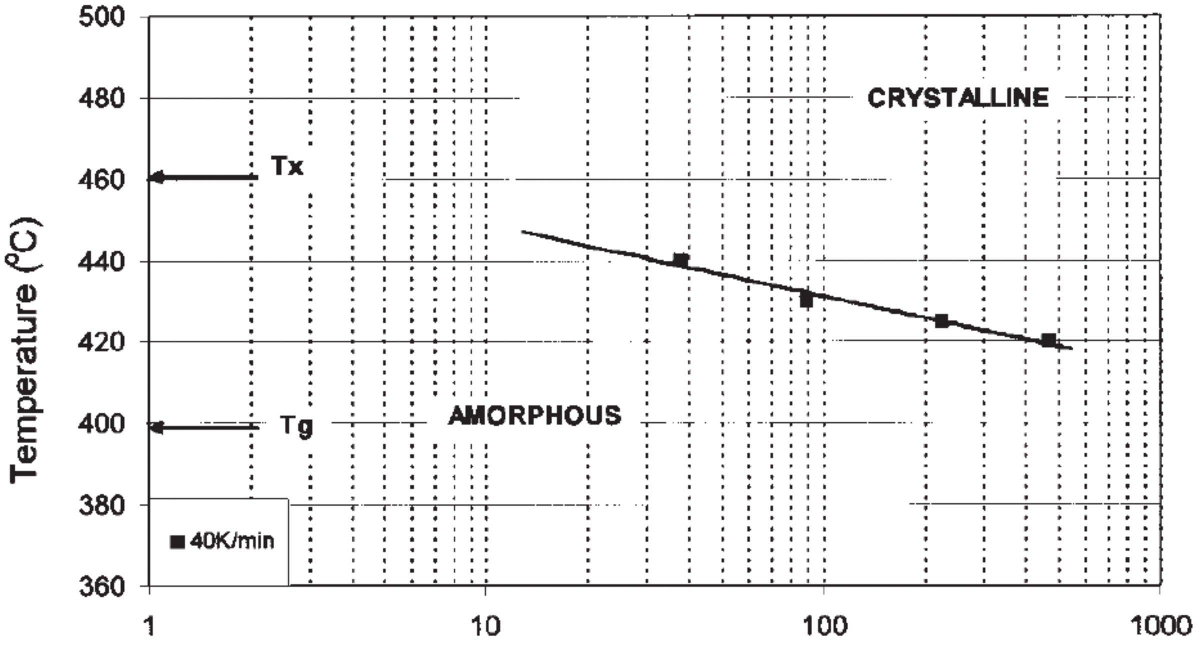

Figure 2.6 TTT diagram for the onset of crystallization of metallic glass powder heated to selected temperatures at 40 K/min [53].

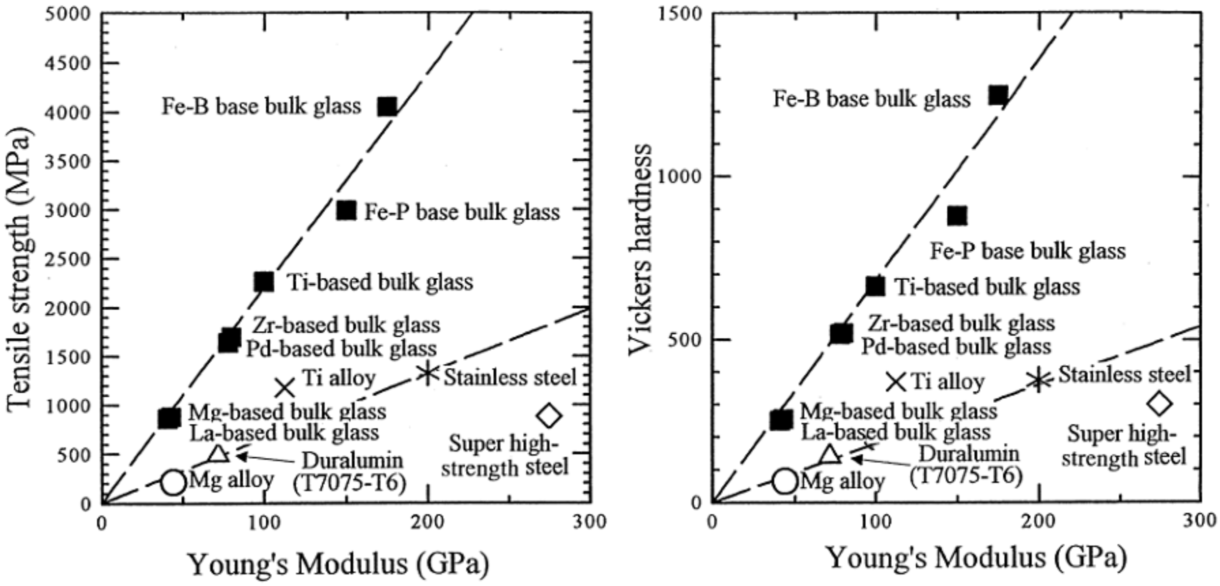

Figure 2.7 Relationship between tensile strength or Vickers hardness (H) and E for various bulk amorphous alloys [4].

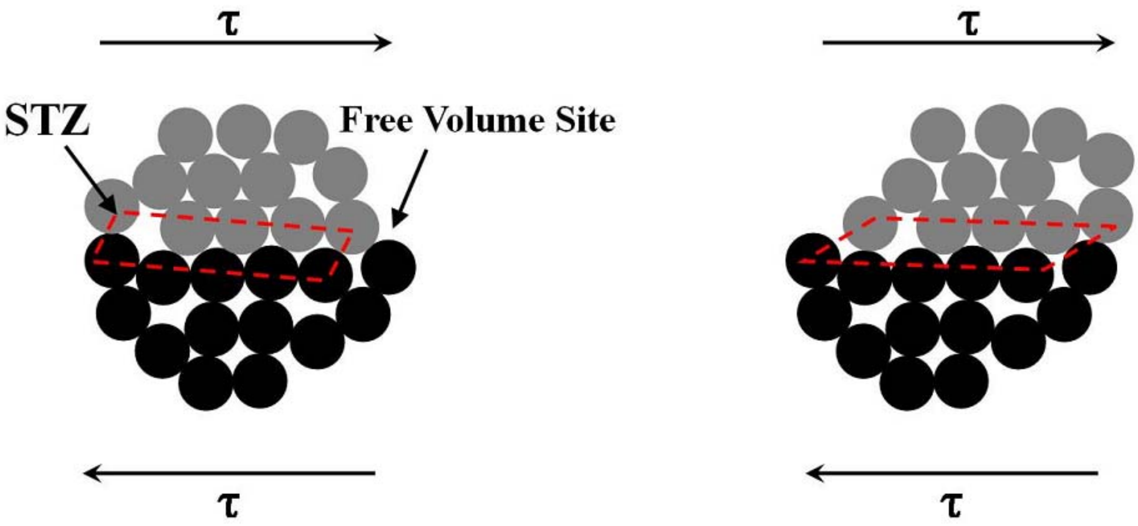

Figure 2.8 The illustration of the shear transformation zones (STZs) (a) before shear deformation and (b) after shear deformation in two-dimensional space [68].

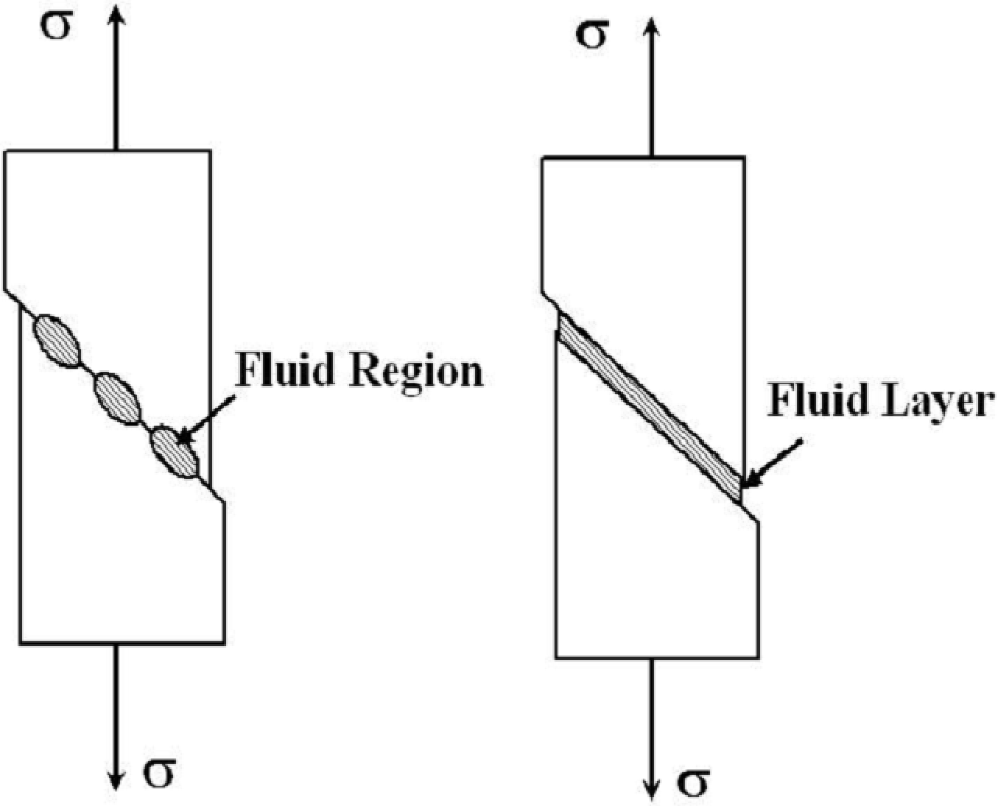

Figure 2.9 Schematic drawing of the fluid zones of amorphous alloy [68].

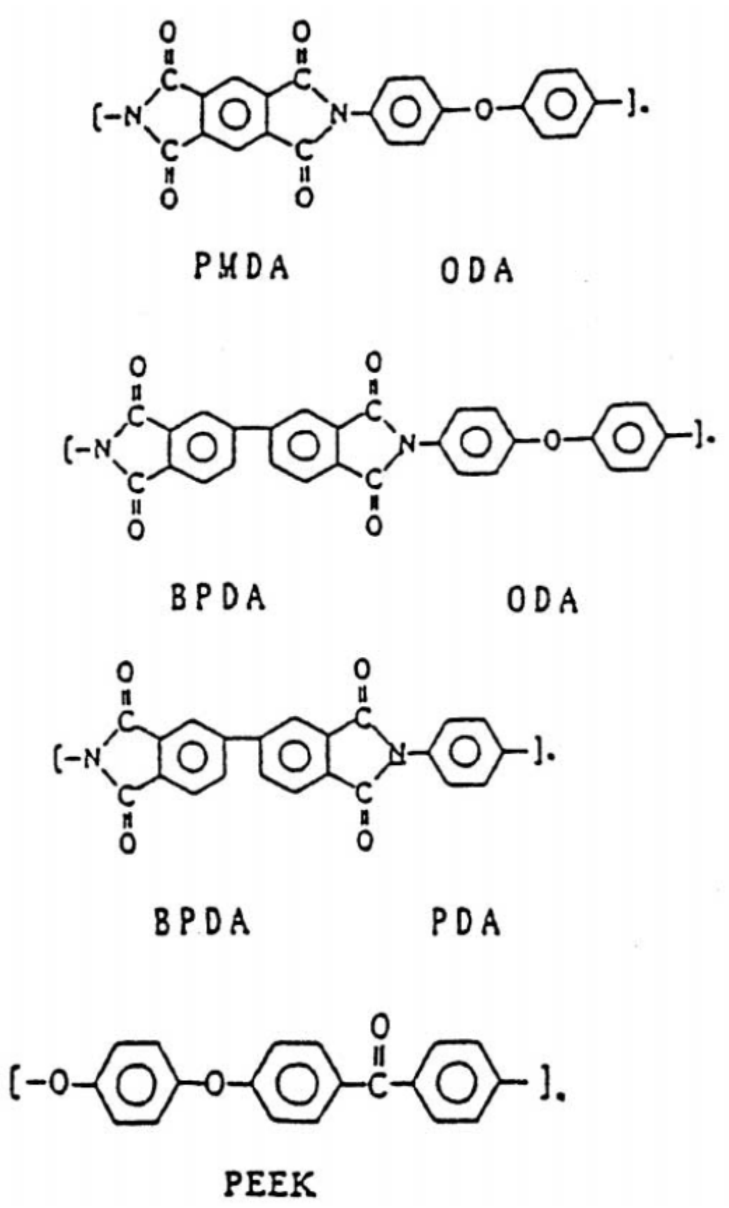

Figure 2.10 Structural formulae of polymer substrate. The upper three formulae is three forms of polyimide, the last formula is polyetheretherketon [59].

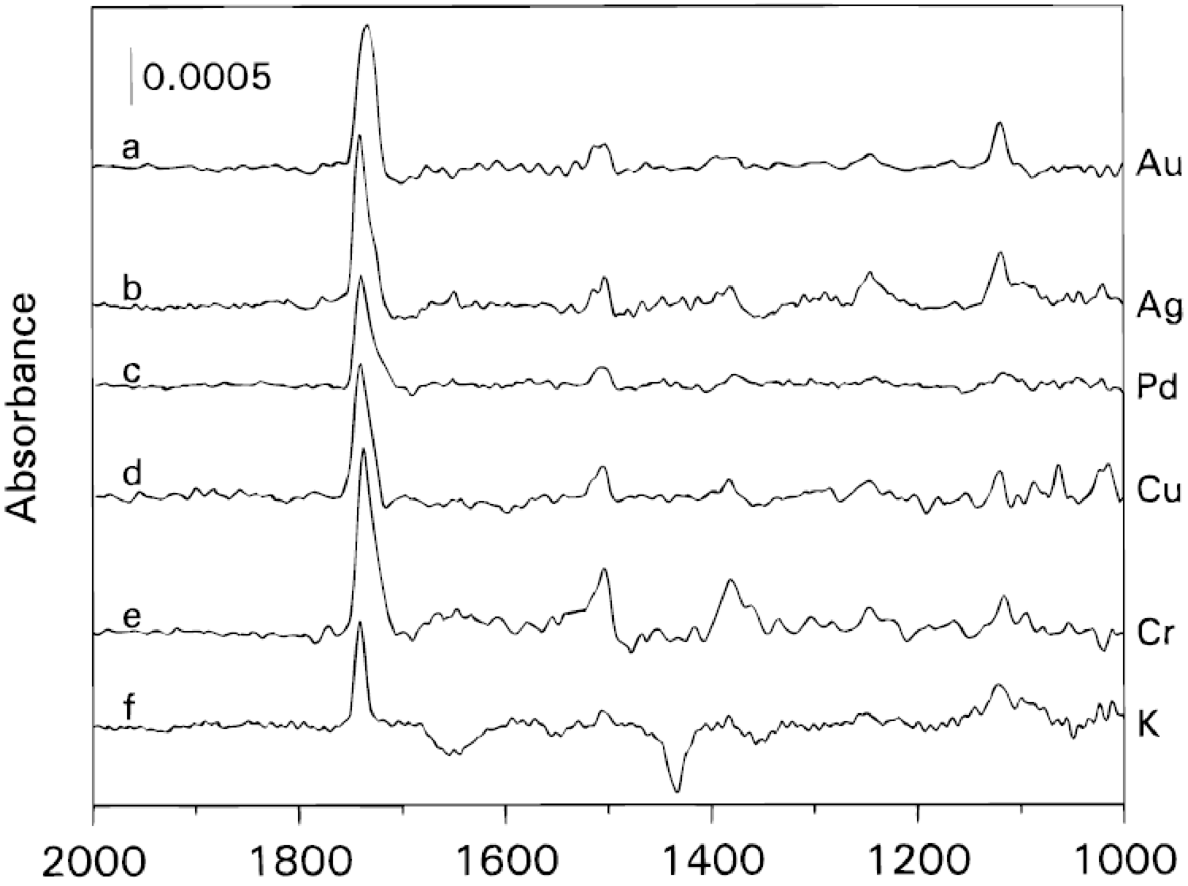

Figure 2.11 FT-IRA difference spectra for about monolayer coverages of (a) gold, (b) silver, (c) palladium, (d) copper, (e) chromium, and (f) potassium [59].

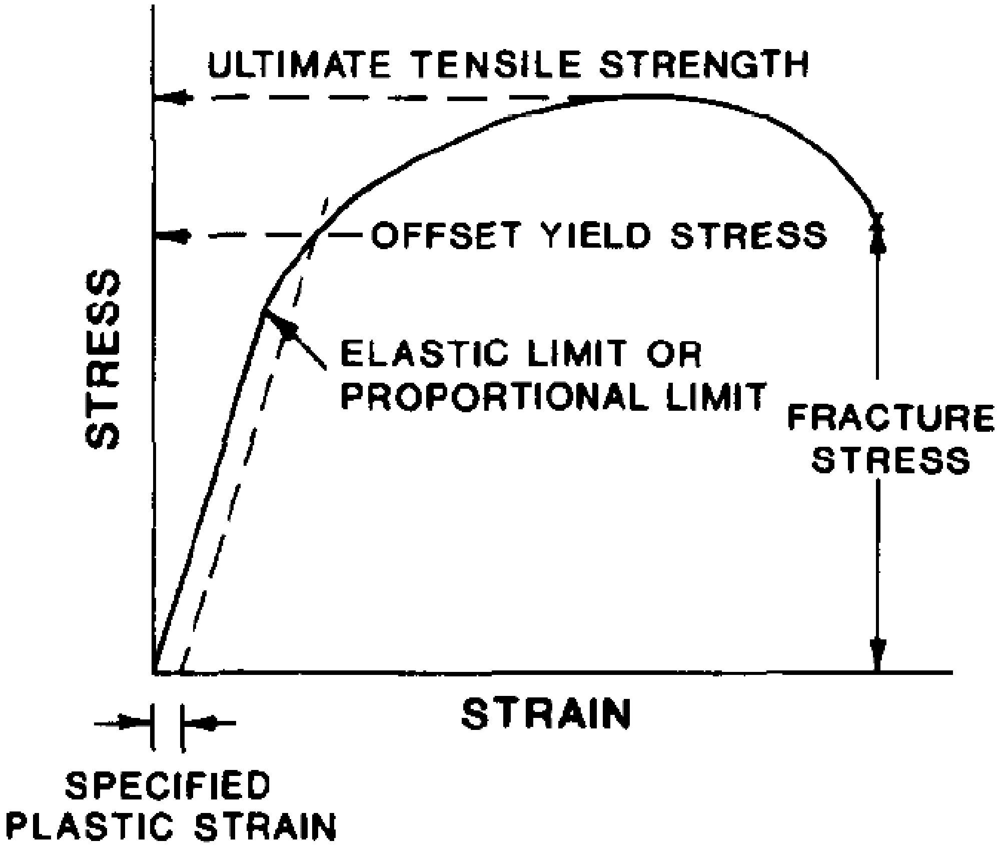

Figure 2.12 Typical stress-strain curve for a metal under uniaxial tension [60].

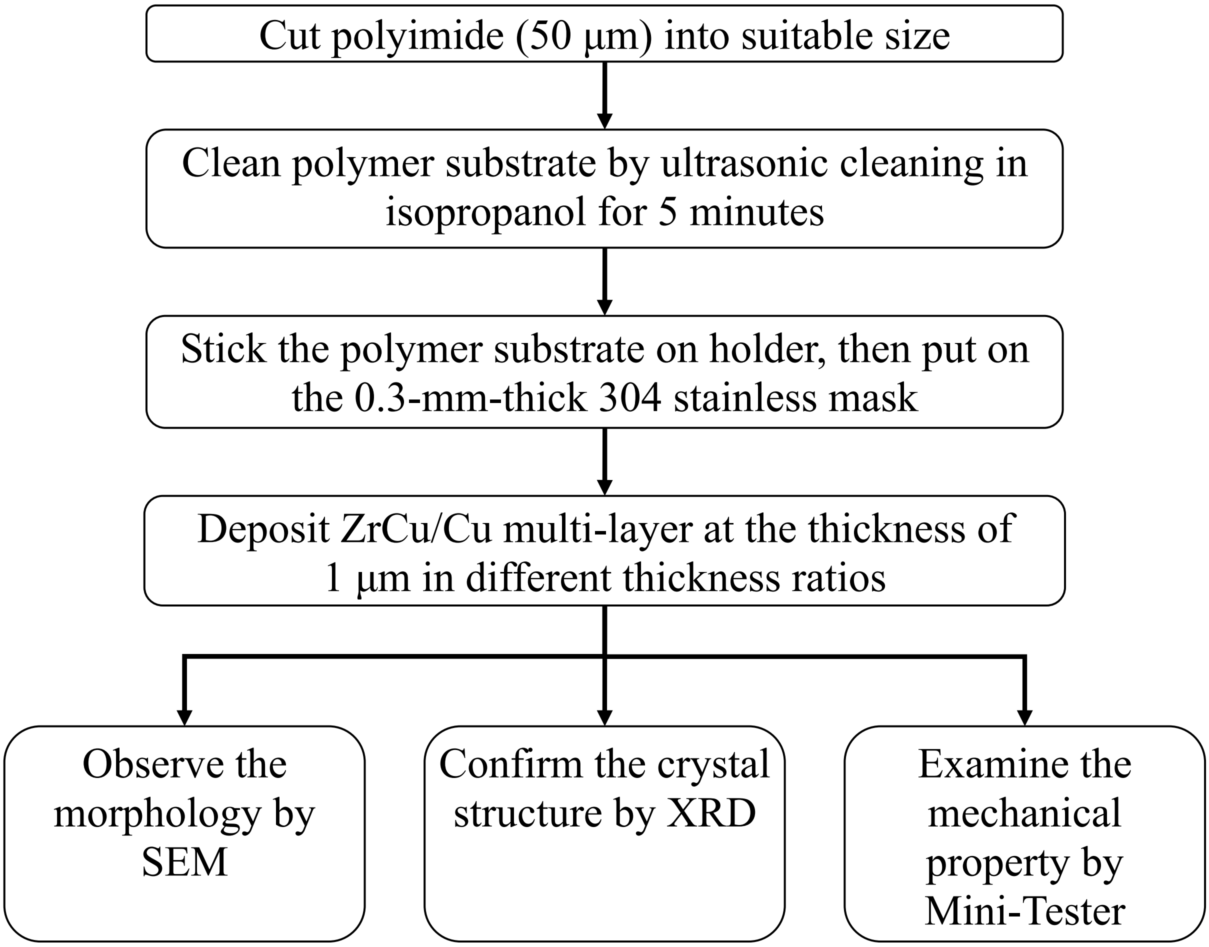

Figure 3.1 The flow chart of the experimental procedure in this study.

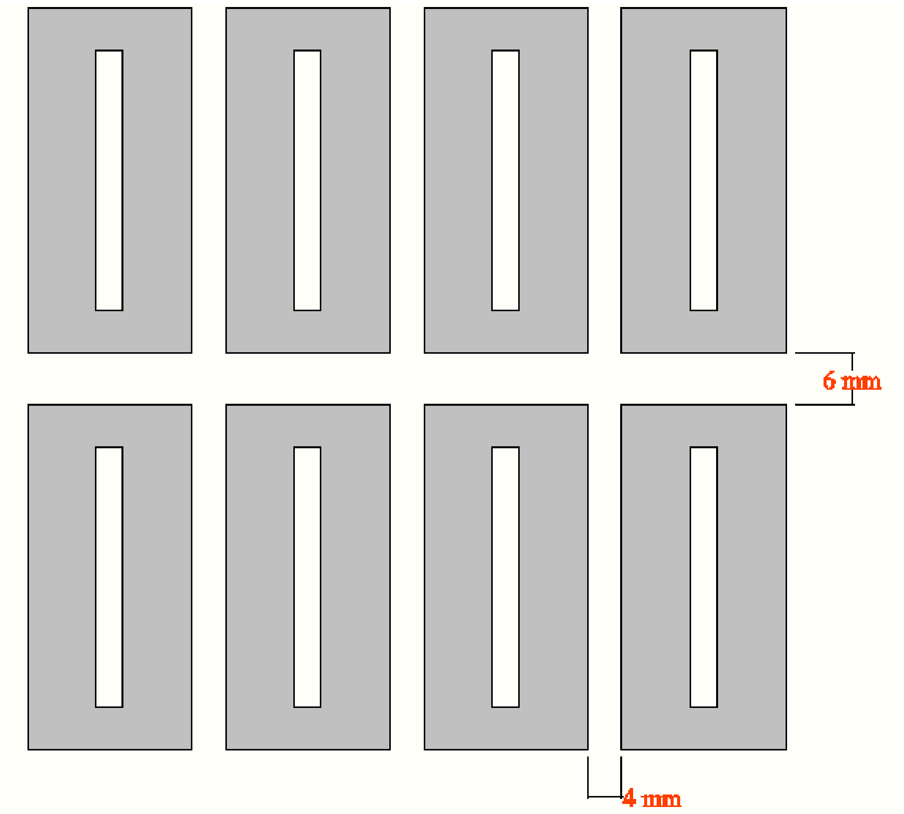

Figure 3.2 The pattern of 0.3-mm-thick stainless masks during sputtering.

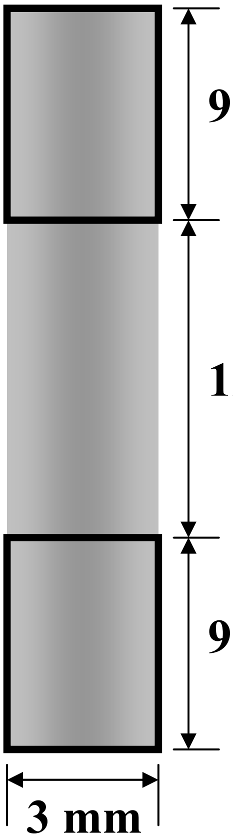

Figure 3.3 Schematic representation of specimen dimensions. The squire of 3 mm × 30 mm is fully deposited with the coated thin film, and only the middle region would be tensioned.

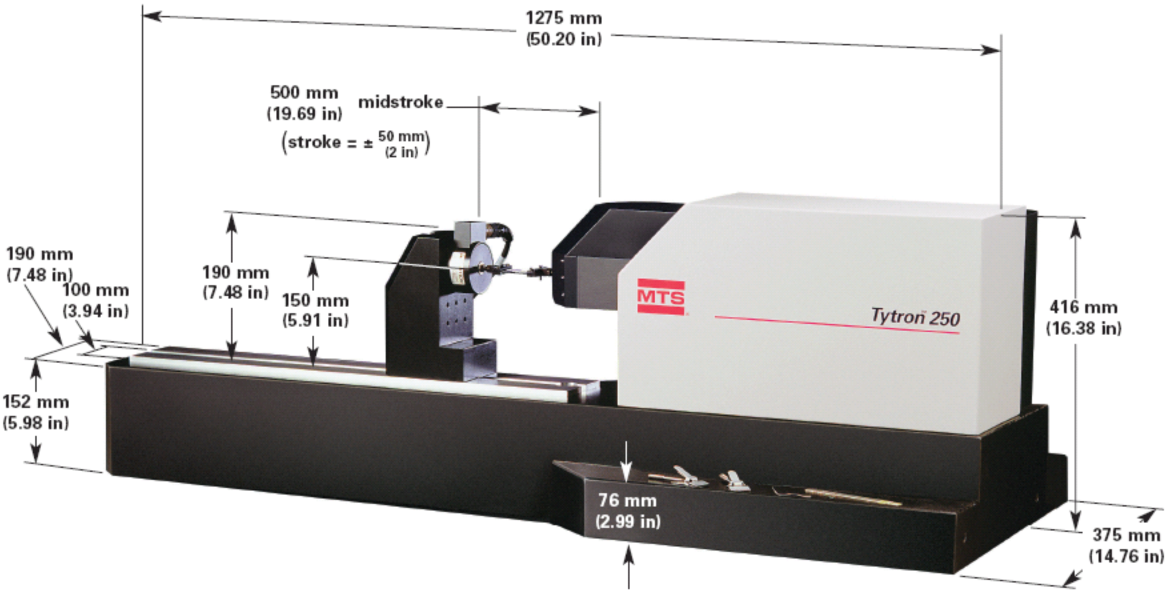

Figure 3.4 Illustration of the MTS Tytron™ 250 Microforce Testing System.

ZrCu/Cu (100 nm/100 nm) ZrCu/Cu (50 nm/50 nm) ZrCu/Cu (10 nm/10 nm)

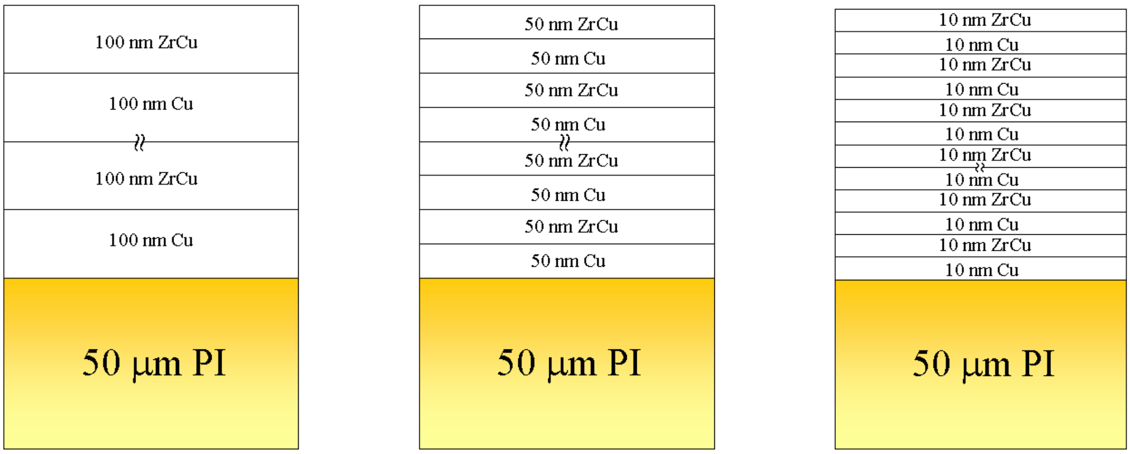

Figure 4.1 Schematic illustrations of the multilayer samples. The overall coated multilayered thin films is all about 1 μm.

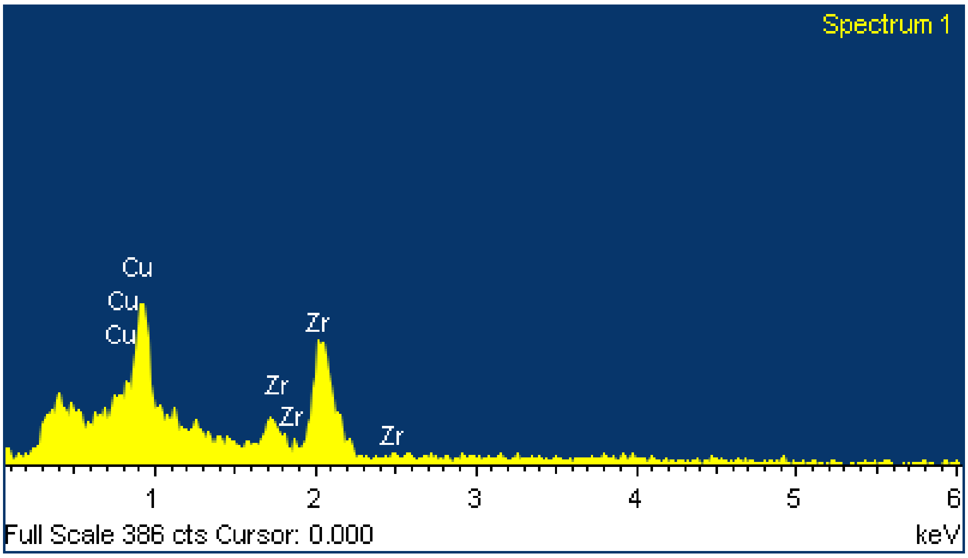

Figure 4.2 Representive EDS pattern of the as-deposited amorphous $Zr_{46}Cu_{54}$ thin film on the silcon nitride substrate.

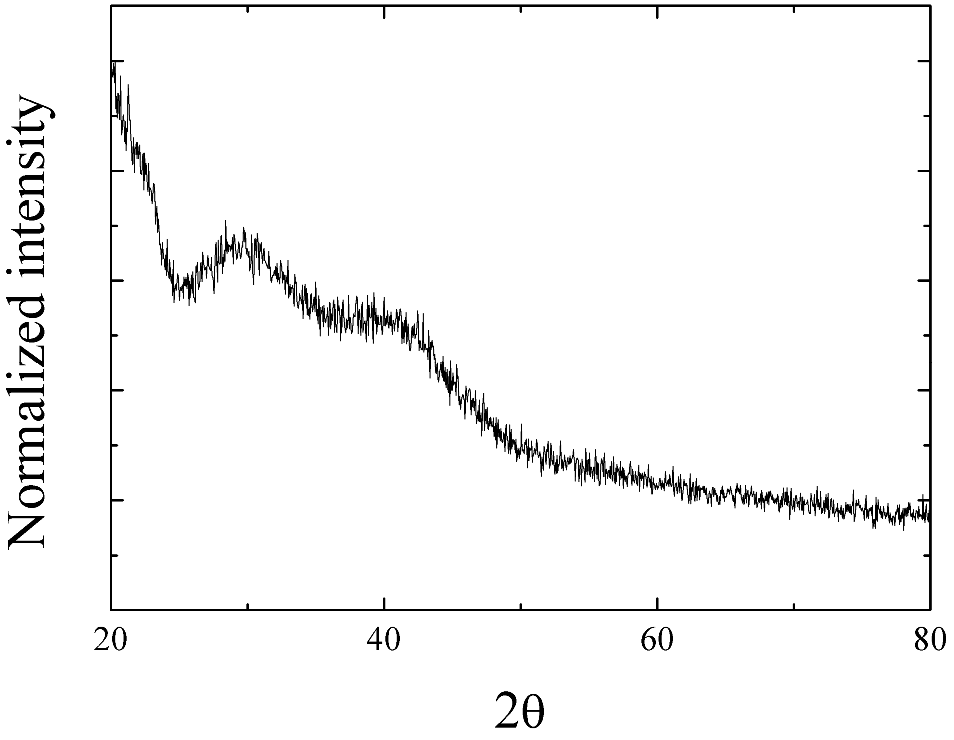

Figure 4.3 XRD pattern of the amorphous ZrCu thin film on the PI substrate.

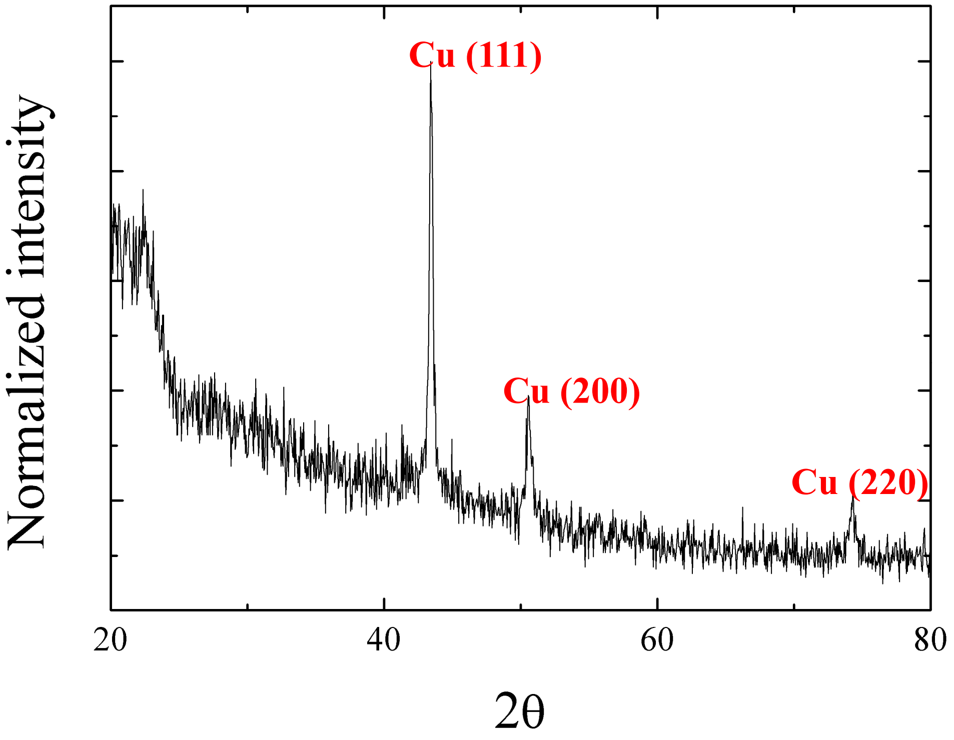

Figure 4.4 XRD pattern of the crystalline Cu thin film on the PI substrate.

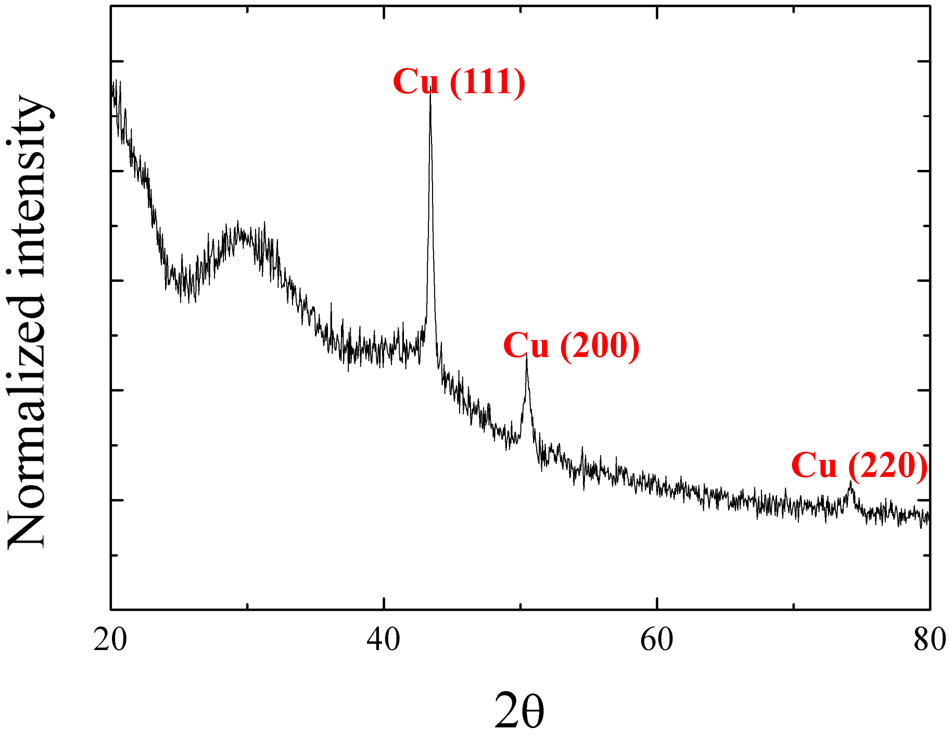

Figure 4.5 XRD pattern of the ZrCu/Cu (100 nm/100 nm) multilayered thin film on PI substrate.

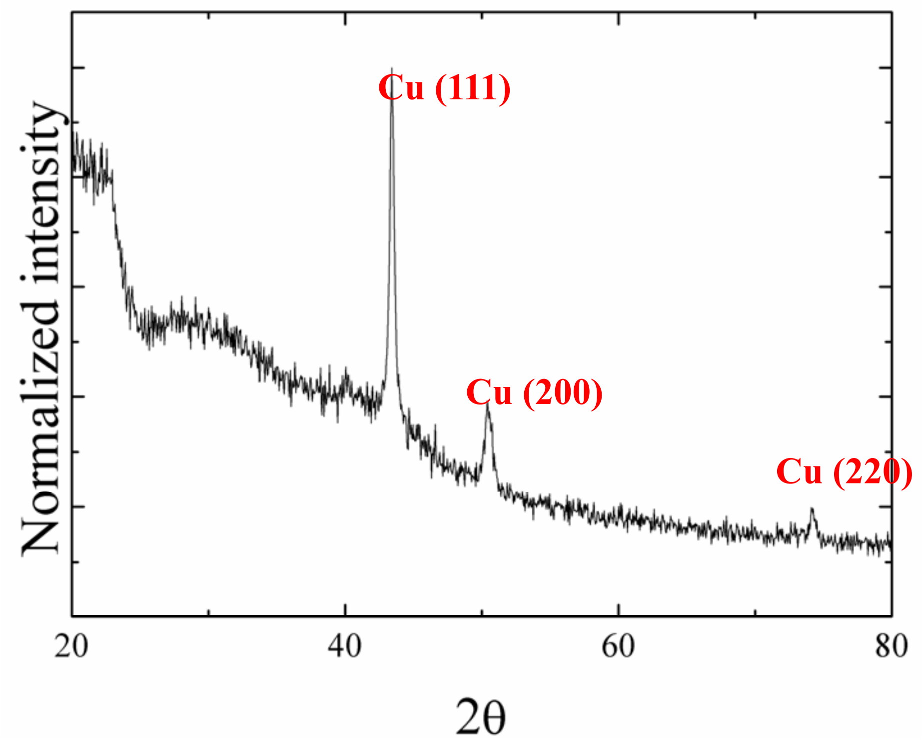

Figure 4.6 XRD pattern of the ZrCu/Cu (75 nm/75 nm) multilayered thin film on PI substrate.

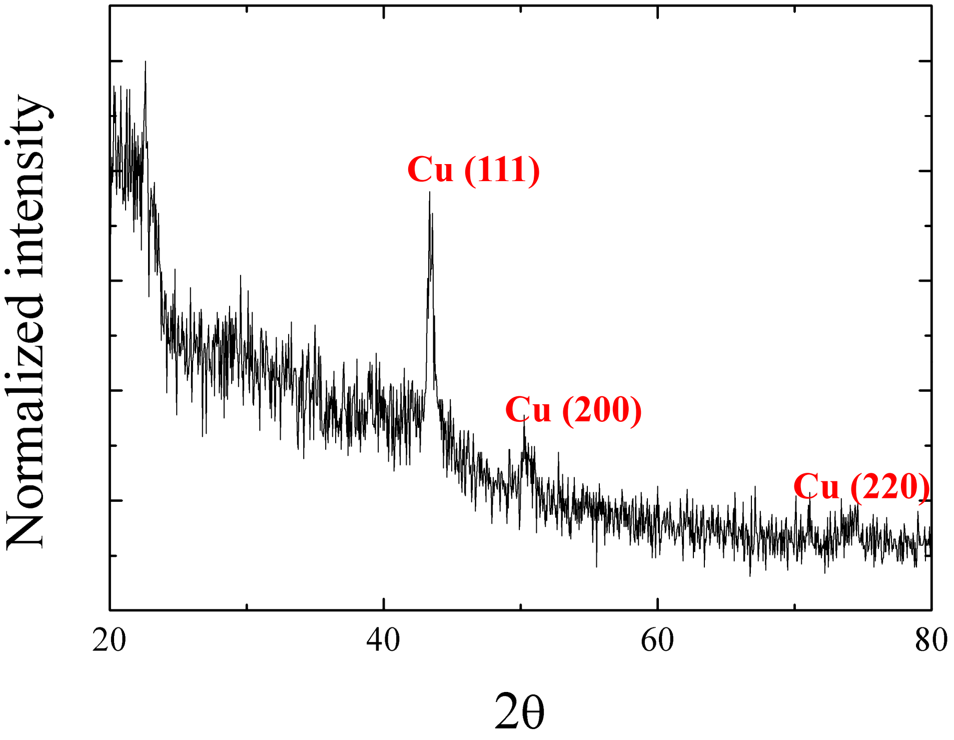

Figure 4.7 XRD pattern of the ZrCu/Cu (50 nm/50 nm) multilayered thin film on PI substrate.

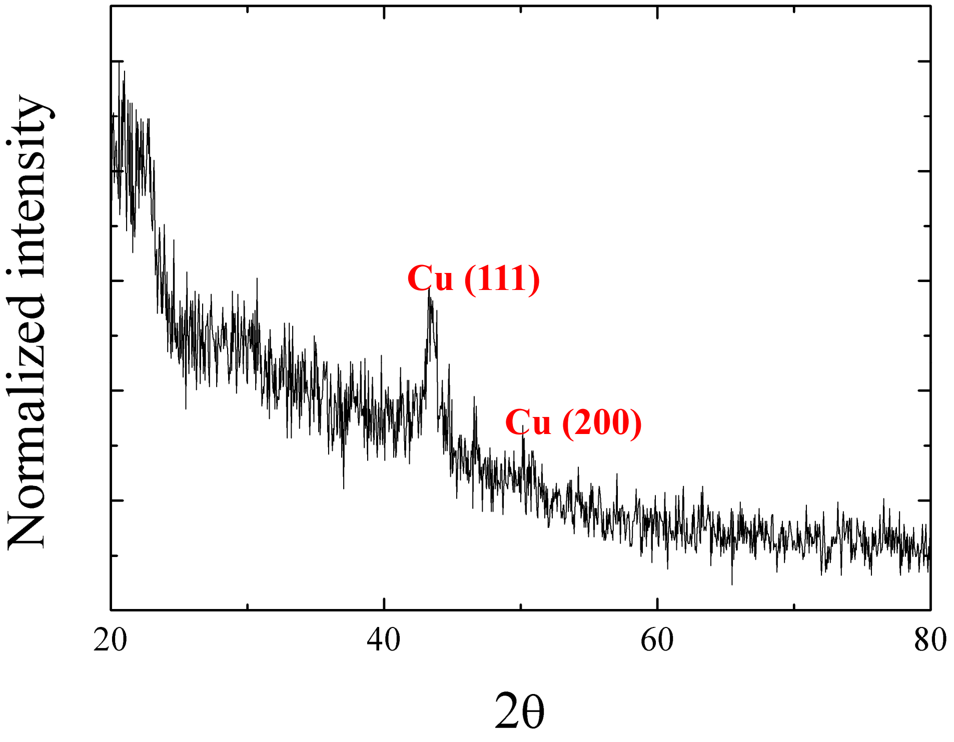

Figure 4.8 XRD pattern of the ZrCu/Cu (25 nm/25 nm) multilayered thin film on PI substrate.

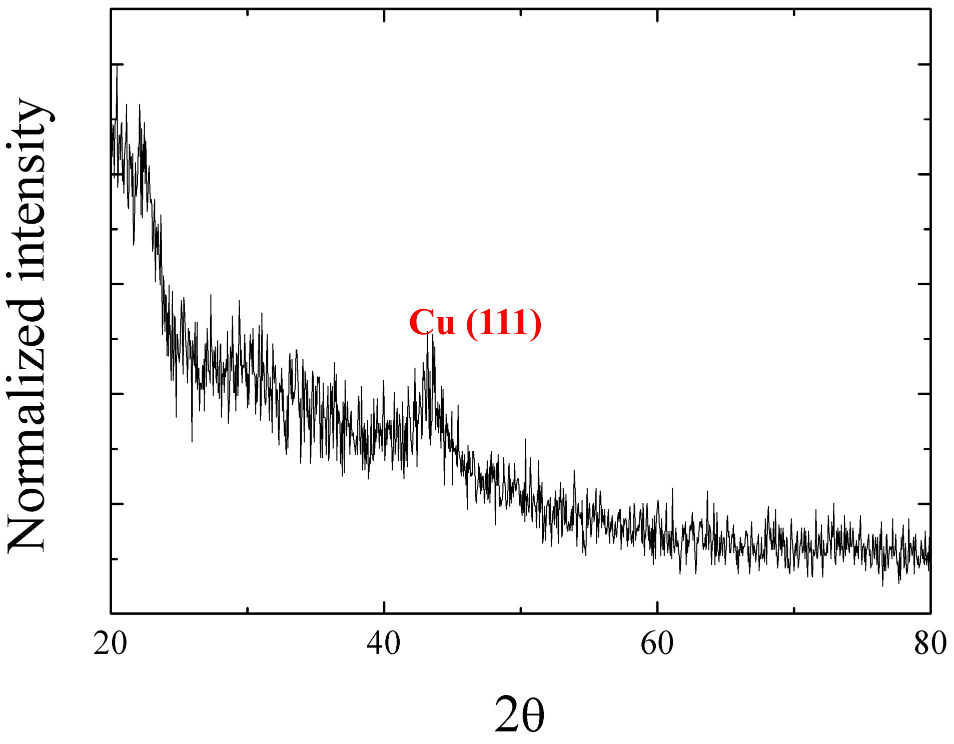

Figure 4.9 XRD pattern of the ZrCu/Cu (10 nm/10 nm) multilayered thin film on PI substrate.

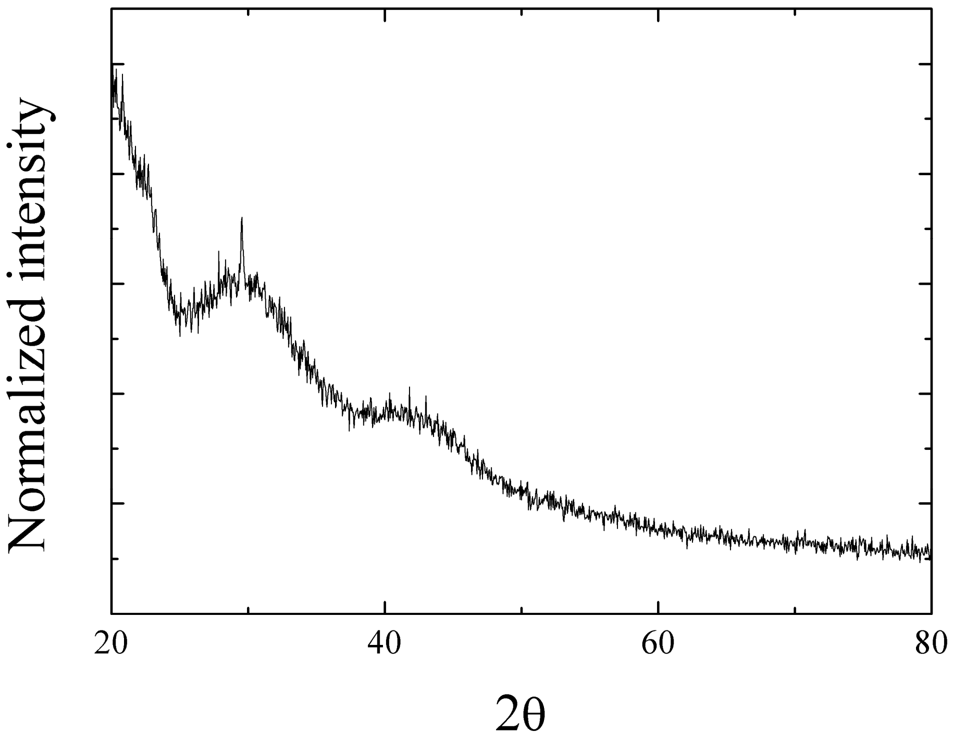

Figure 4.10 XRD pattern of the uncoated PI substrate.

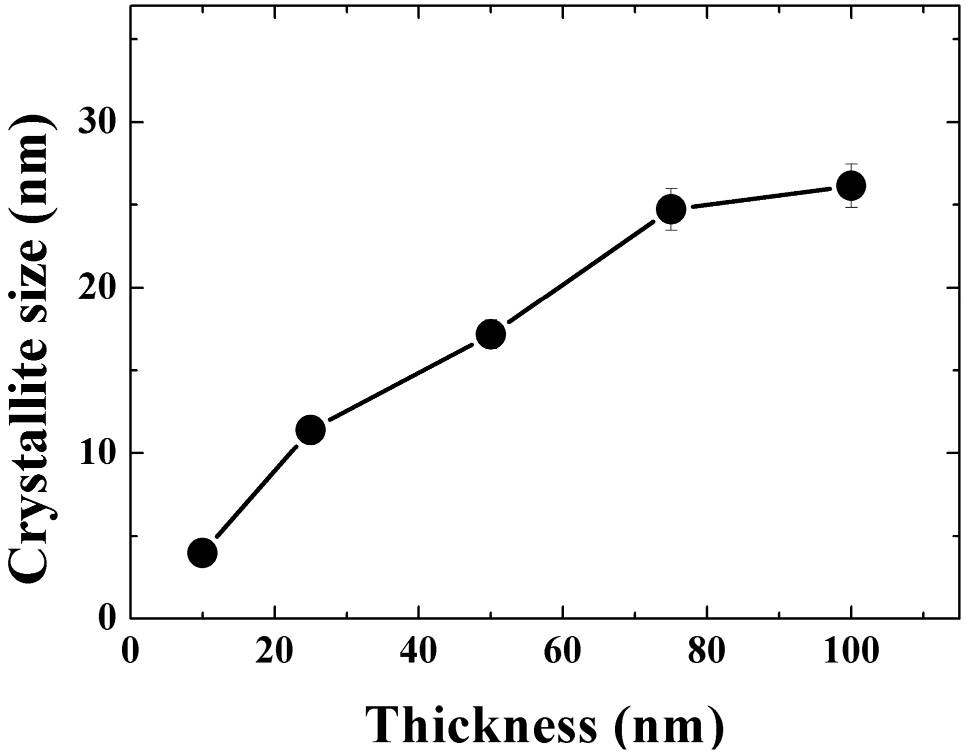

Figure 4.11 The relationship between crystallite sizes of Cu and thickness.

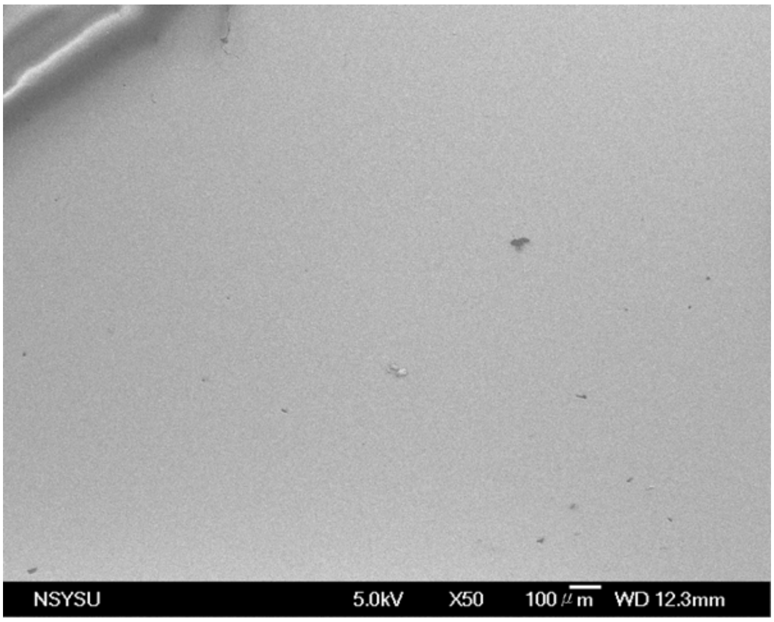

Figure 4.12 Surface morphology of the undeformed ZrCu/Cu (100 nm/100 nm) multilayer sample at a low magnification of 50X.

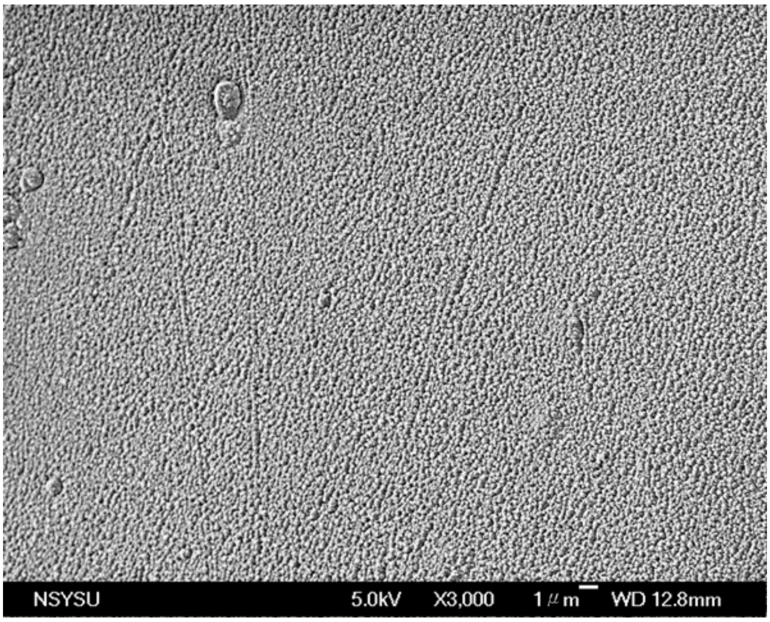

Figure 4.13 Surface morphology of the undeformed ZrCu/Cu (100 nm/100 nm) multilayer sample at a low magnification of 3000X.

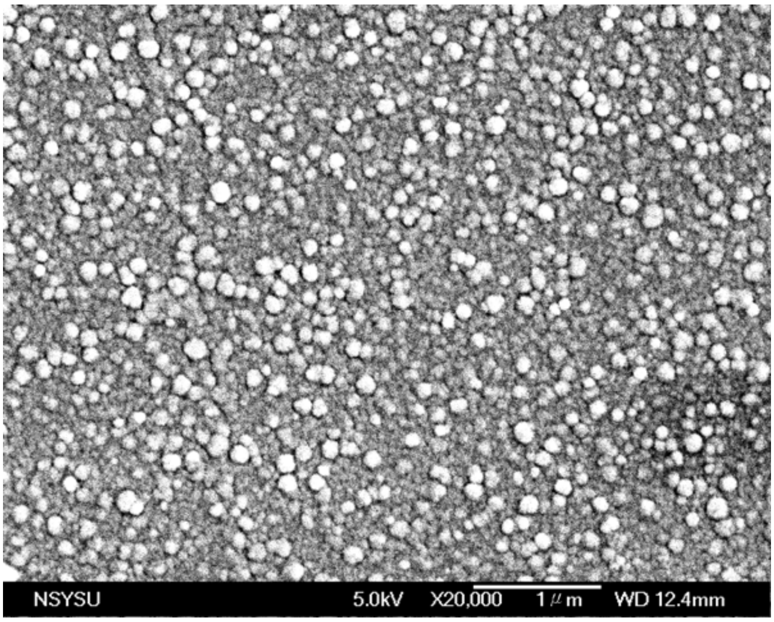

Figure 4.14 Surface morphology of the undeformed ZrCu/Cu (100 nm/100 nm) multilayer sample at a high magnification of 20000X.

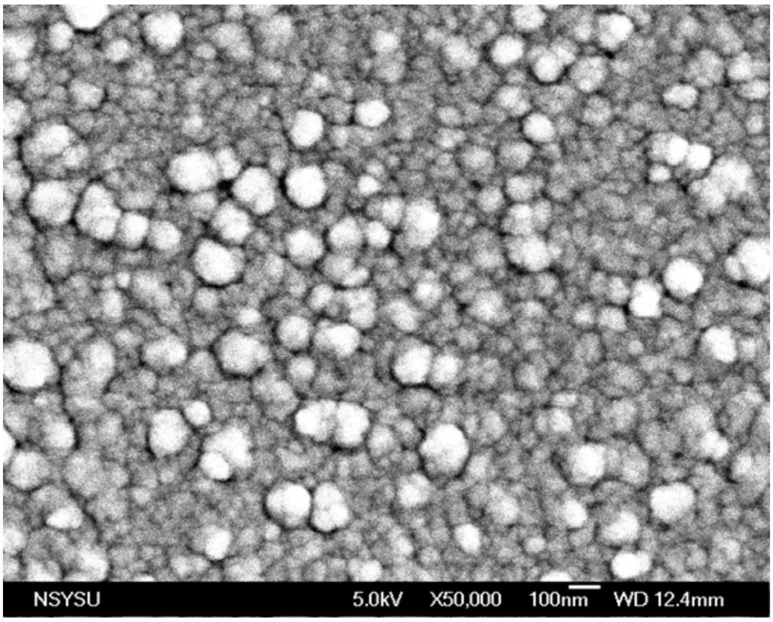

Figure 4.15 Surface morphology of the undeformed ZrCu/Cu (100 nm/100 nm) multilayer sample at a high magnification of 50000X.

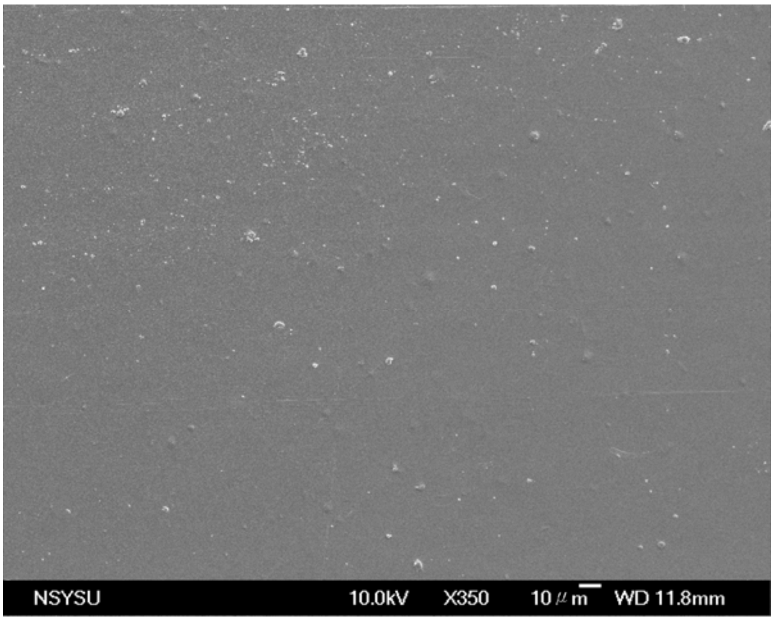

Figure 4.16 Surface morphology of the undeformed ZrCu/Cu (75 nm/75 nm) multilayer sample at a low magnification of 350X.

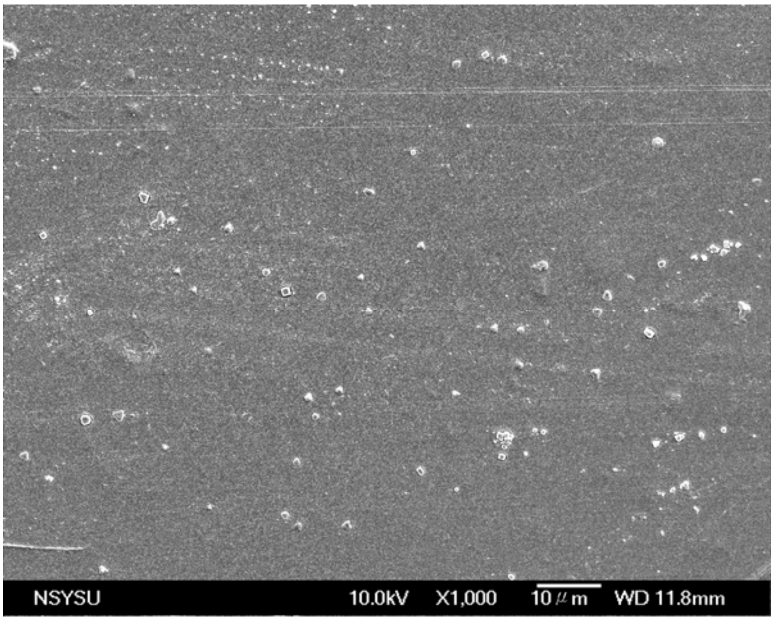

Figure 4.17 Surface morphology of the undeformed ZrCu/Cu (75 nm/75 nm) multilayer sample at a low magnification of 1000X.

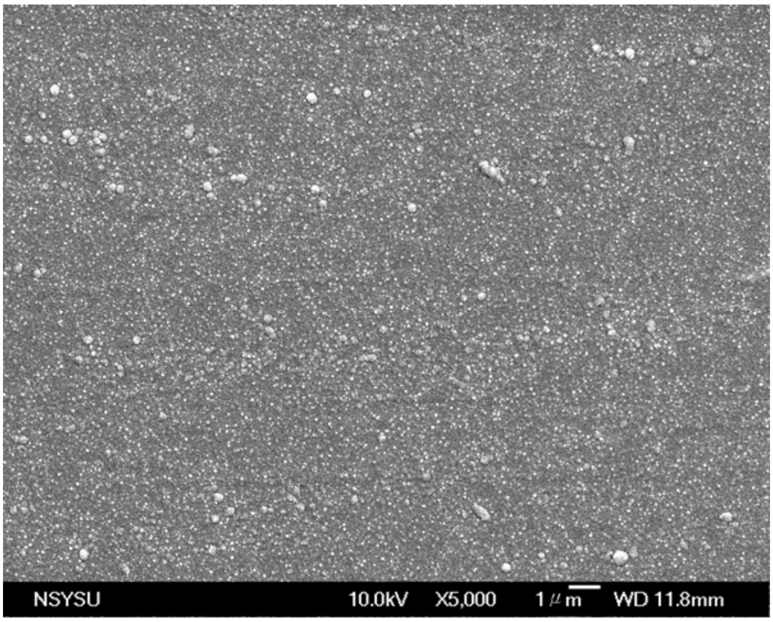

Figure 4.18 Surface morphology of the undeformed ZrCu/Cu (75 nm/75 nm) multilayer sample at a high magnification of 5000X.

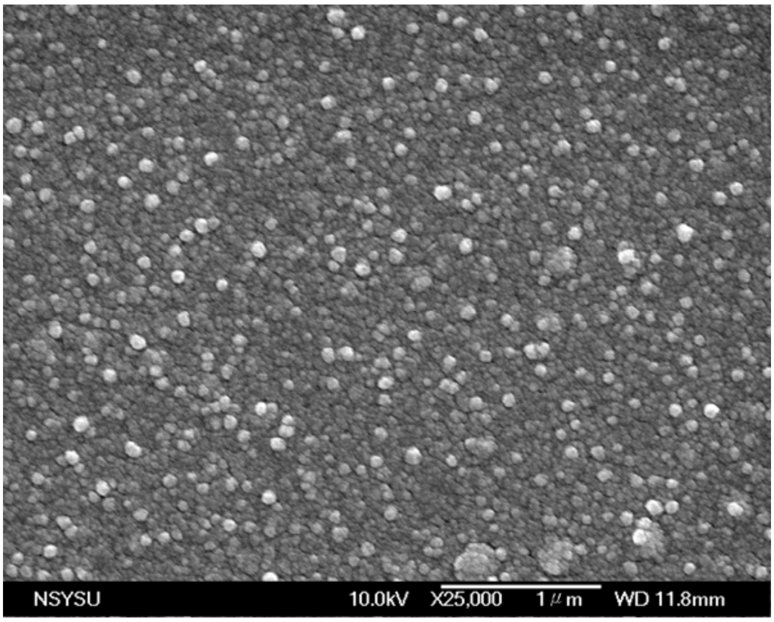

Figure 4.19 Surface morphology of the undeformed ZrCu/Cu (75 nm/75 nm) multilayer sample at a high magnification of 25000X.

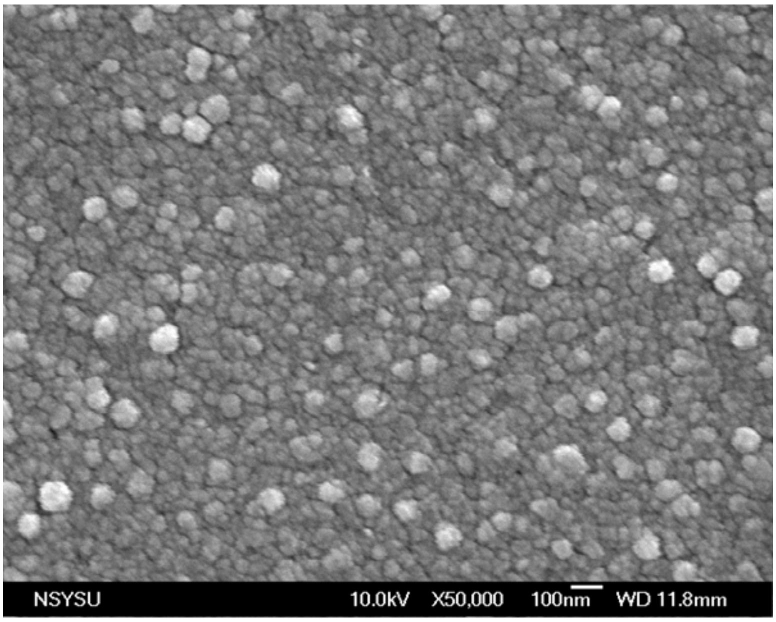

Figure 4.20 Surface morphology of the undeformed ZrCu/Cu (75 nm/75 nm) multilayer sample at a high magnification of 50000X.

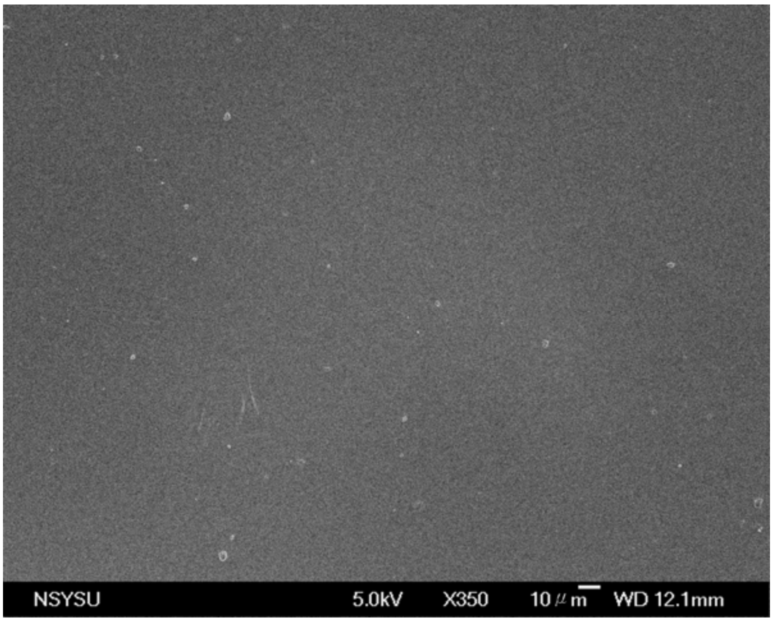

Figure 4.21 Surface morphology of the undeformed ZrCu/Cu (50 nm/50 nm) multilayer sample at a low magnification of 350X.

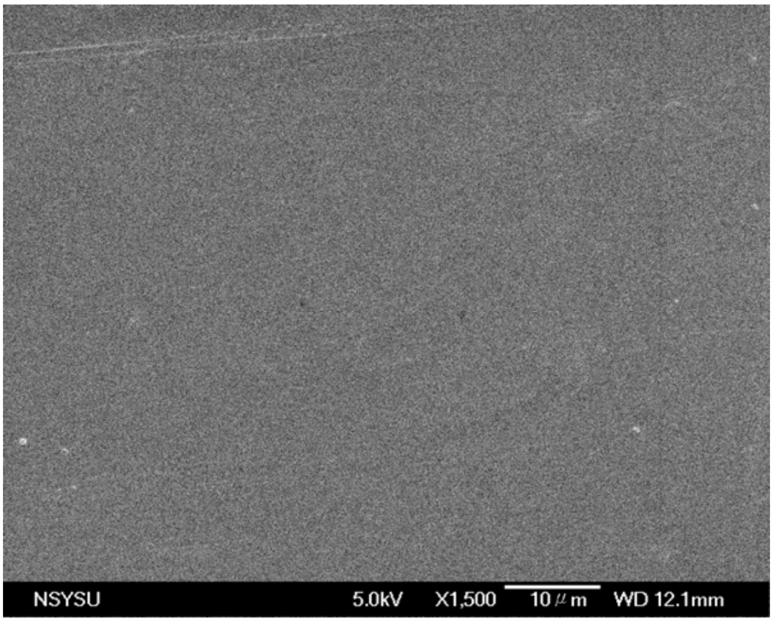

Figure 4.22 Surface morphology of the undeformed ZrCu/Cu (50 nm/50 nm) multilayer sample at a low magnification of 1500X.

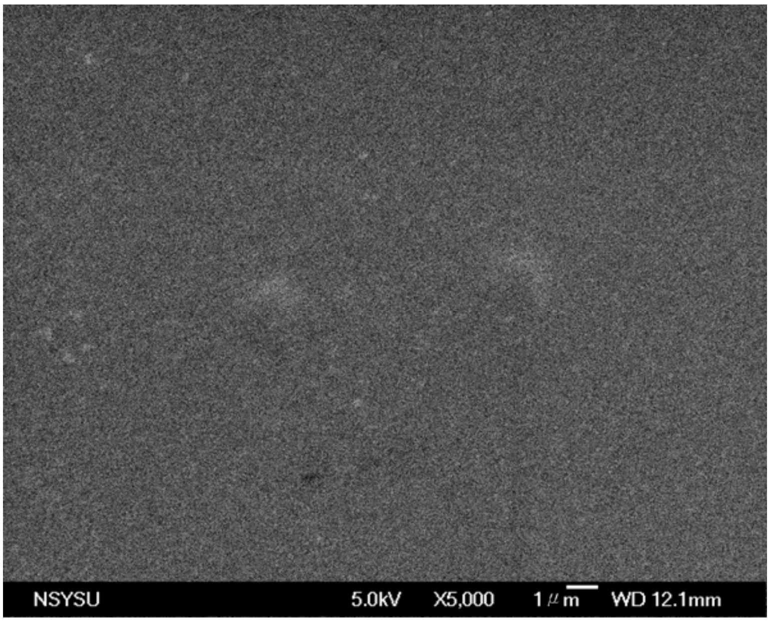

Figure 4.23 Surface morphology of the undeformed ZrCu/Cu (50 nm/50 nm) multilayer sample at a high magnification of 5000X.

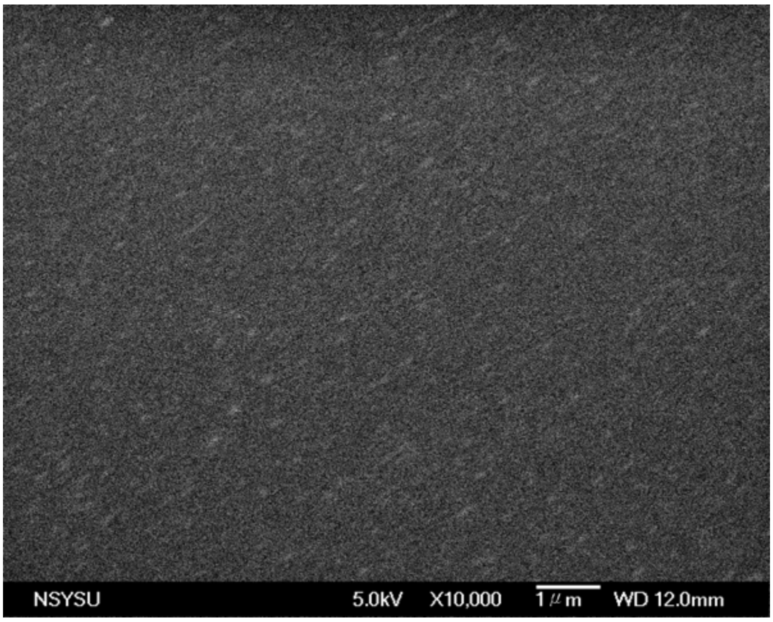

Figure 4.24 Surface morphology of the undeformed ZrCu/Cu (50 nm/50 nm) multilayer sample at a high magnification of 10000X.

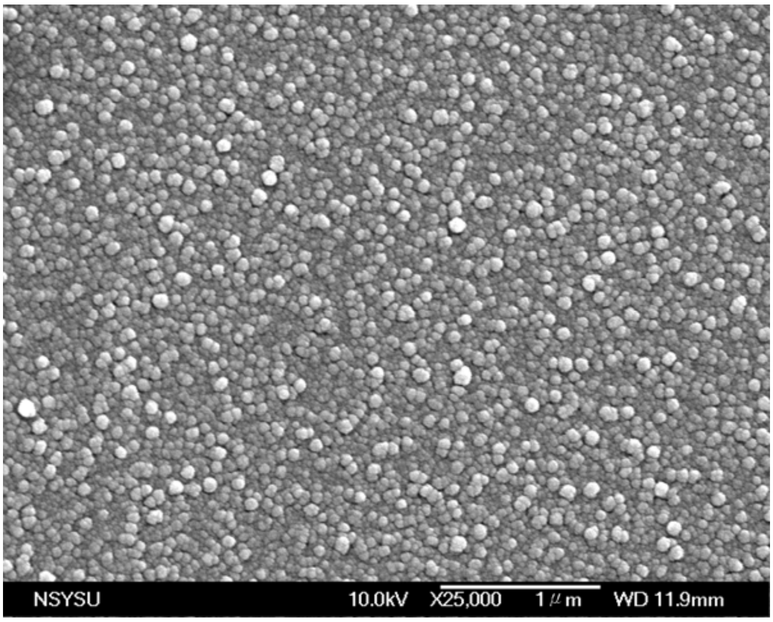

Figure 4.25 Surface morphology of the undeformed ZrCu/Cu (50 nm/50 nm) multilayer sample at a high magnification of 25000X.

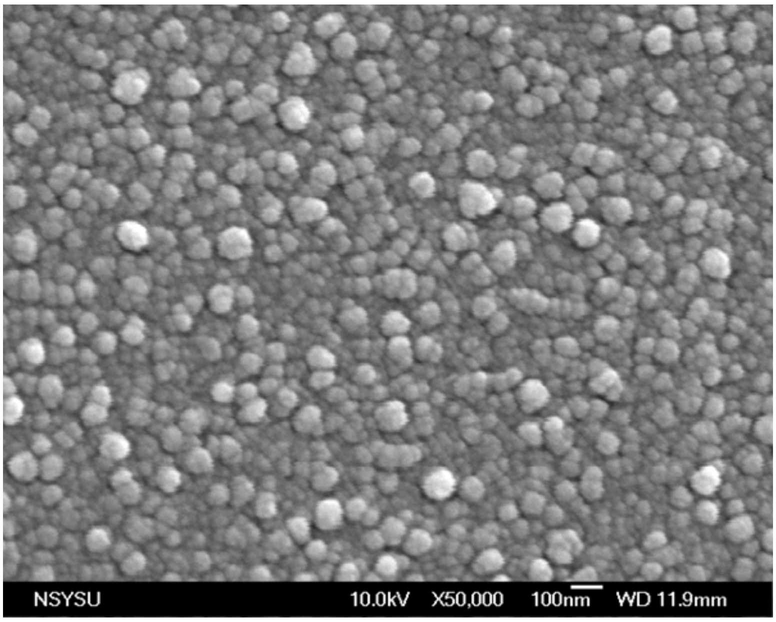

Figure 4.26 Surface morphology of the undeformed ZrCu/Cu (50 nm/50 nm) multilayer sample at a high magnification of 50000X.

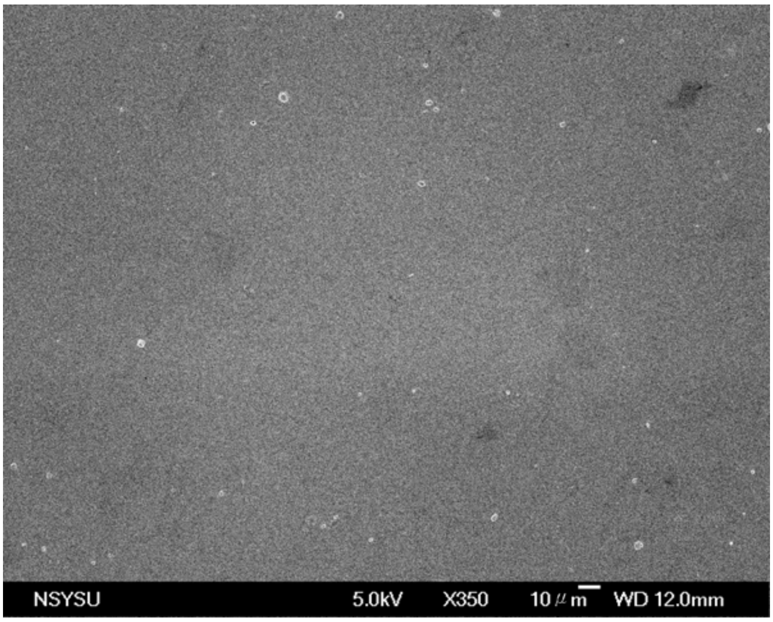

Figure 4.27 Surface morphology of the undeformed ZrCu/Cu (25 nm/25 nm) multilayer sample at a low magnification of 350X.

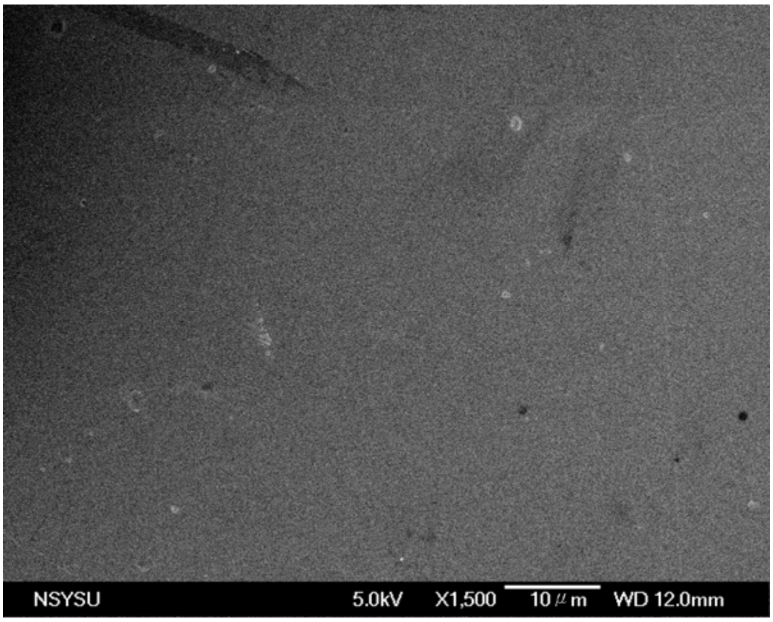

Figure 4.28 Surface morphology of the undeformed ZrCu/Cu (25 nm/25 nm) multilayer sample at a low magnification of 1500X.

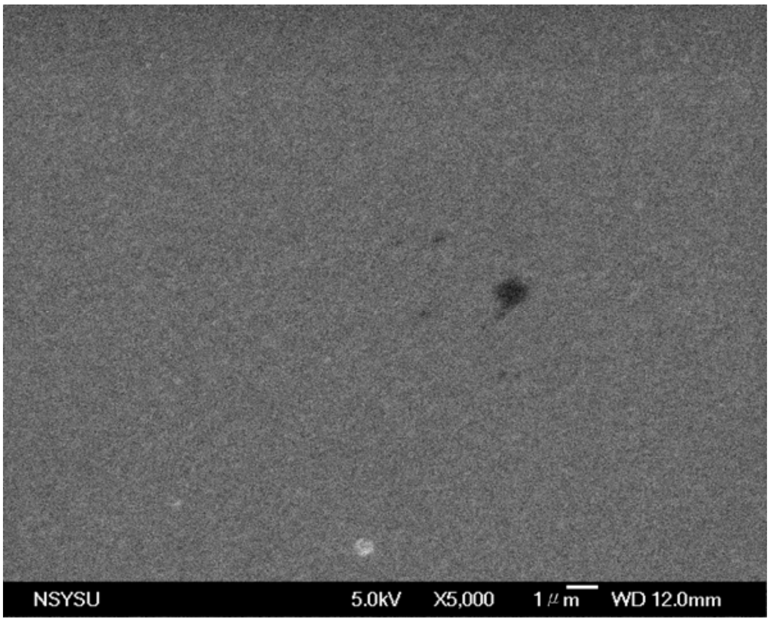

Figure 4.29 Surface morphology of the undeformed ZrCu/Cu (25 nm/25 nm) multilayer sample at a high magnification of 5000X.

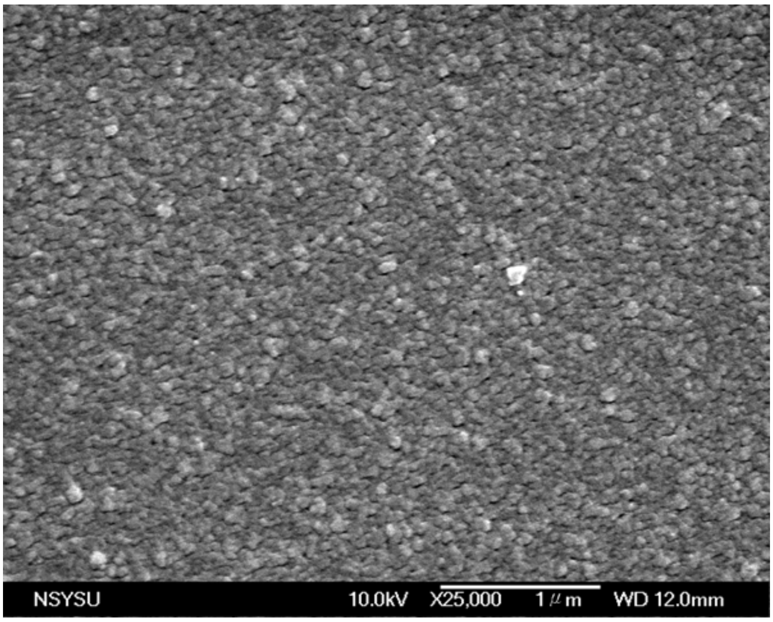

Figure 4.30 Surface morphology of the undeformed ZrCu/Cu (25 nm/25 nm) multilayer sample at a high magnification of 25000X.

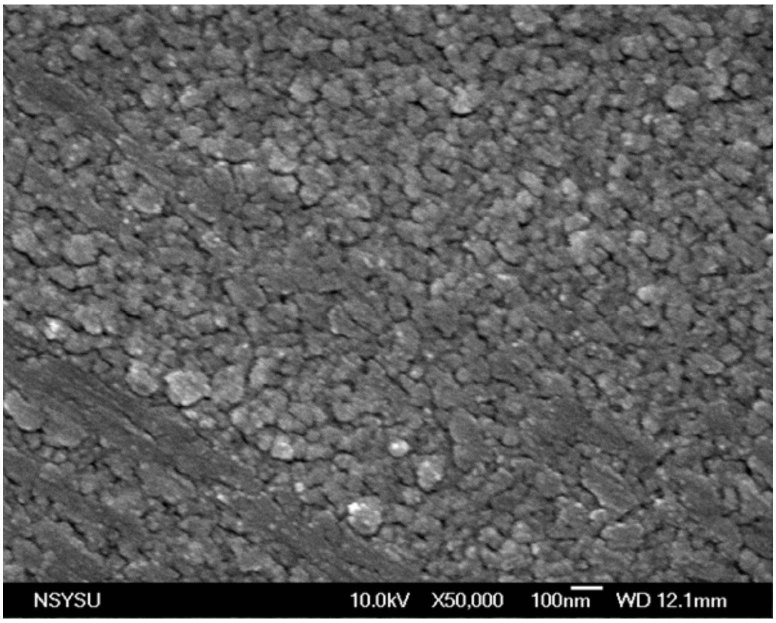

Figure 4.31 Surface morphology of the undeformed ZrCu/Cu (25 nm/25 nm) multilayer sample at a high magnification of 50000X.

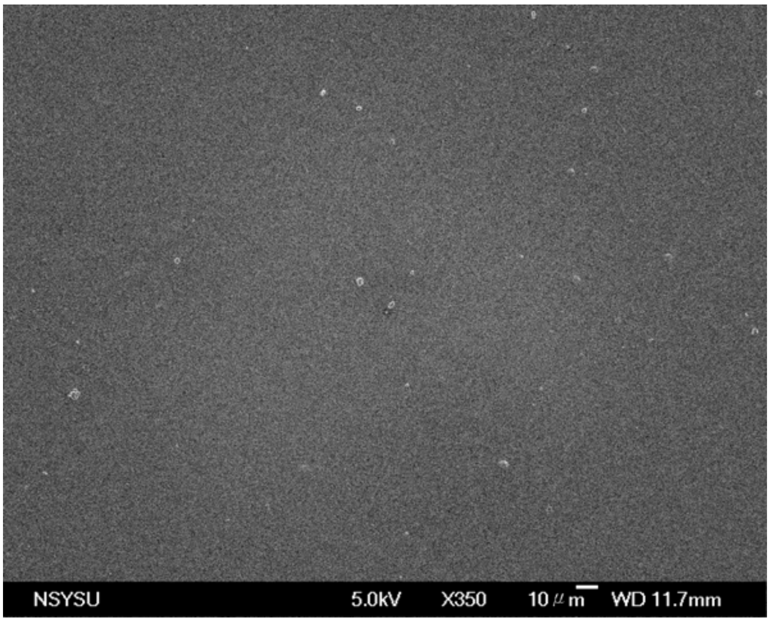

Figure 4.32 Surface morphology of the undeformed ZrCu/Cu (10 nm/10 nm) multilayer sample at a low magnification of 350X.

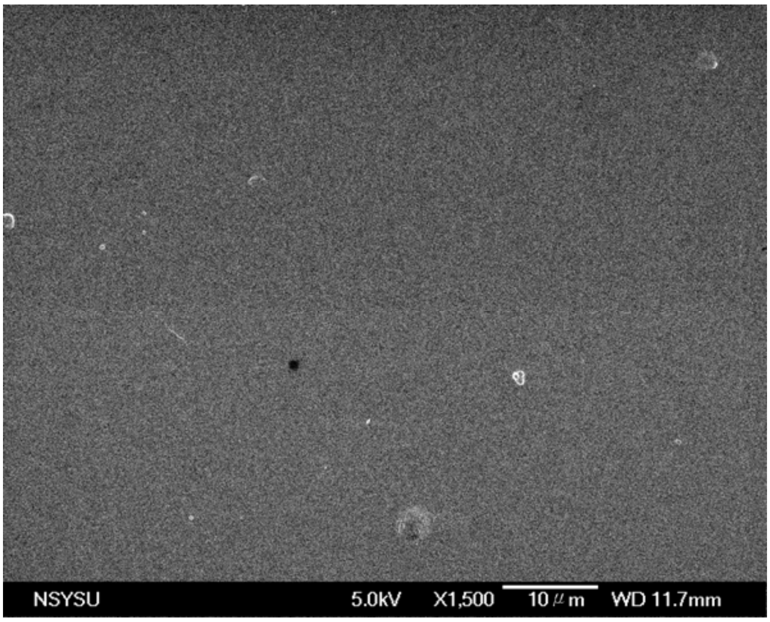

Figure 4.33 Surface morphology of the undeformed ZrCu/Cu (10 nm/10 nm) multilayer sample at a low magnification of 1500X.

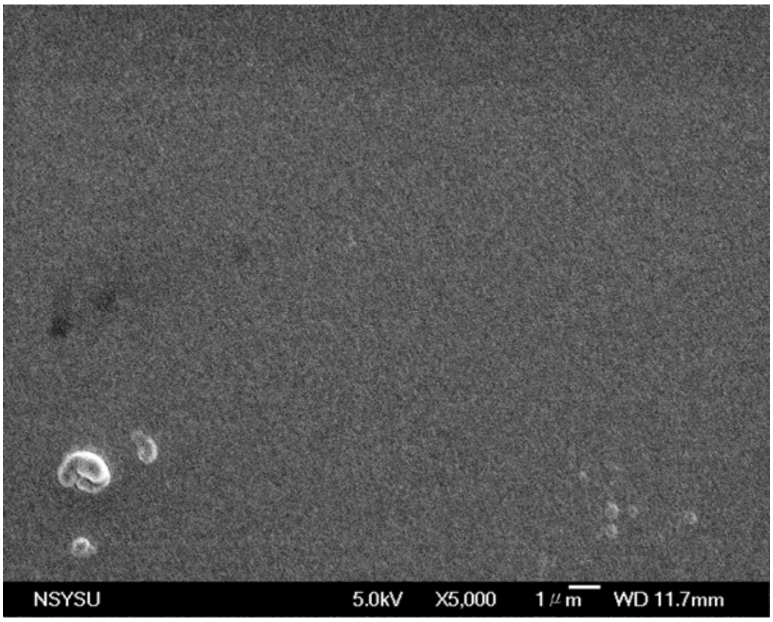

Figure 4.34 Surface morphology of the undeformed ZrCu/Cu (10 nm/10 nm) multilayer sample at a high magnification of 5000X.

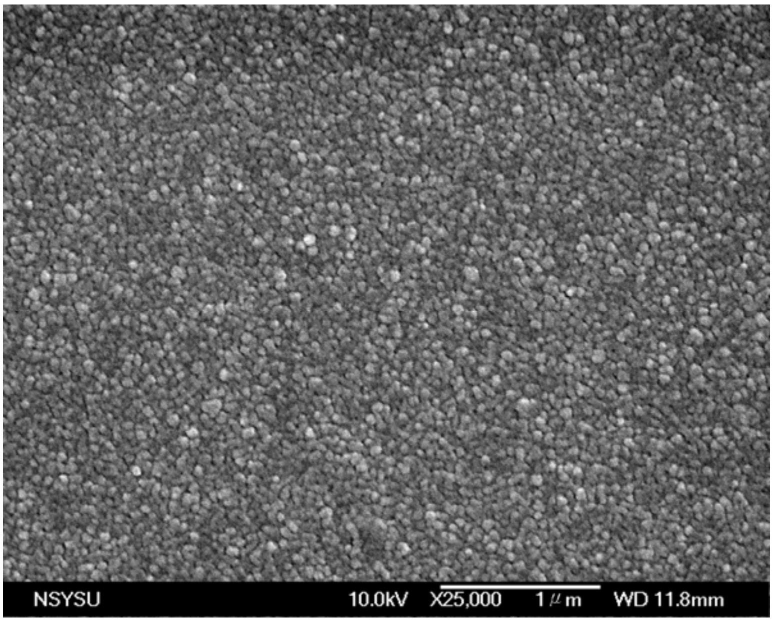

Figure 4.35 Surface morphology of the undeformed ZrCu/Cu (10 nm/10 nm) multilayer sample at a high magnification of 25000X.

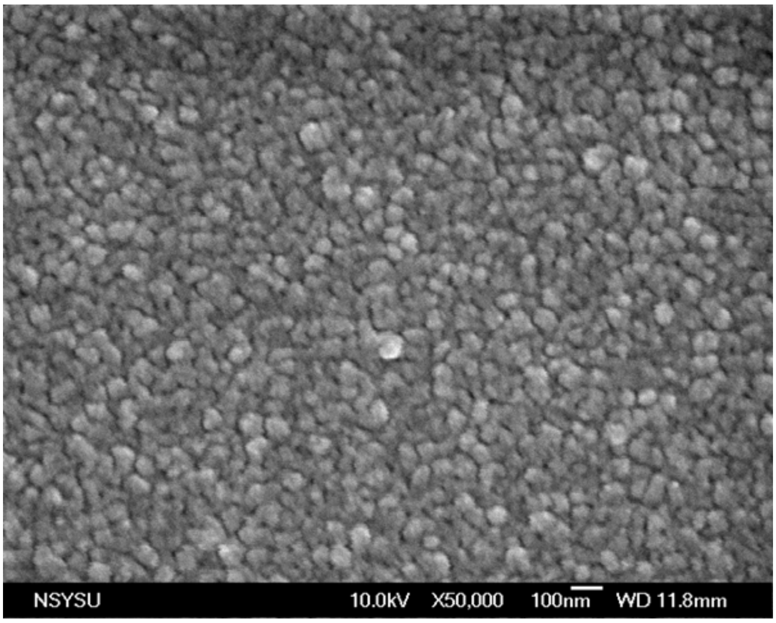

Figure 4.36 Surface morphology of the undeformed ZrCu/Cu (10 nm/10 nm) multilayer sample at a high magnification of 50000X.

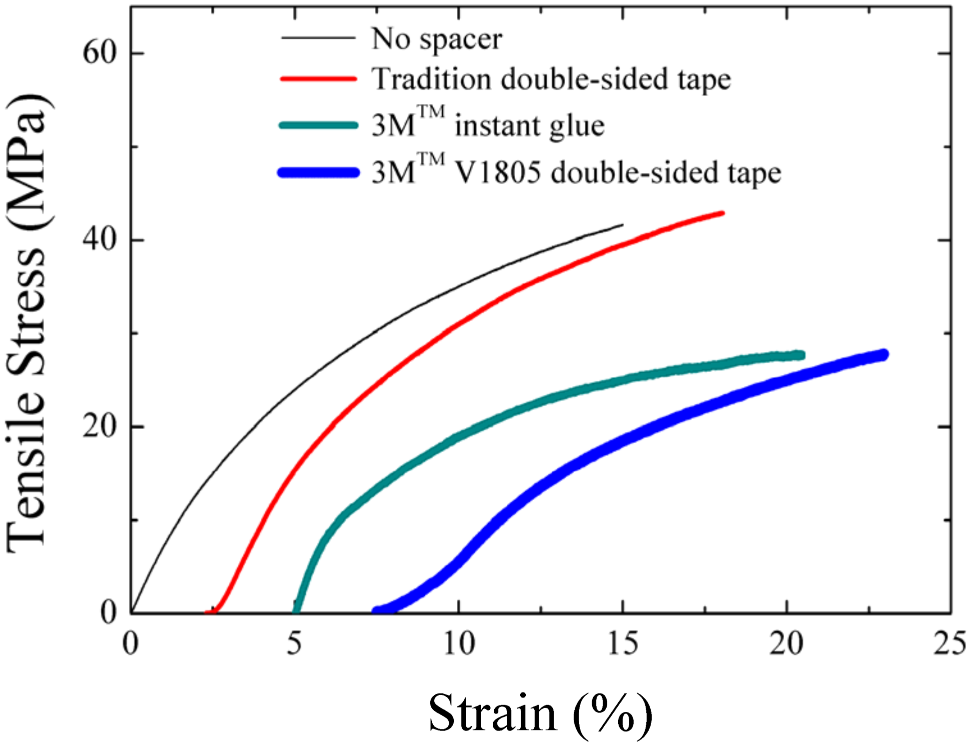

Figure 4.37 Stress-stress curves of clean PI with no spacer, stuck with the spacers stuck by the tradition double-sided tape,. the 3M^{TM} instant glue, and the 3M^{TM} V1805 double-sided tape.

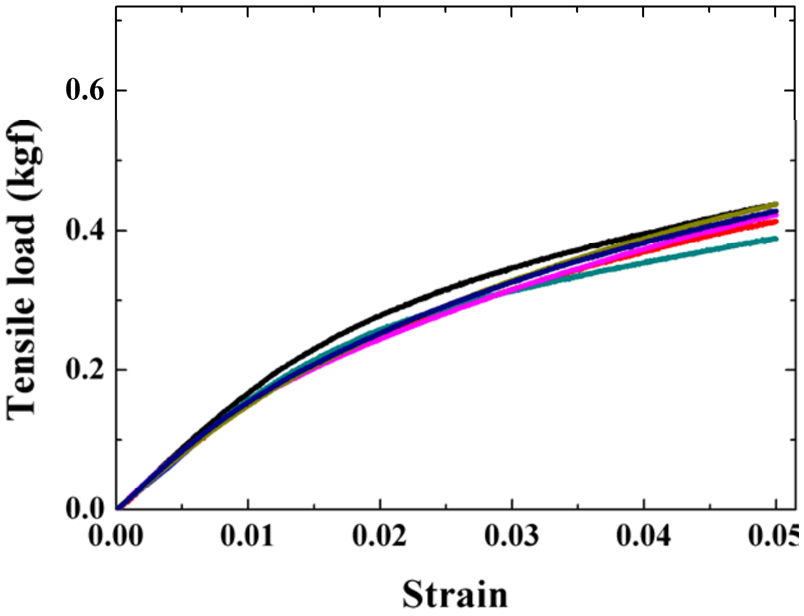

Figure 4.38 The tensile test results of the PI substrates in different rounds.

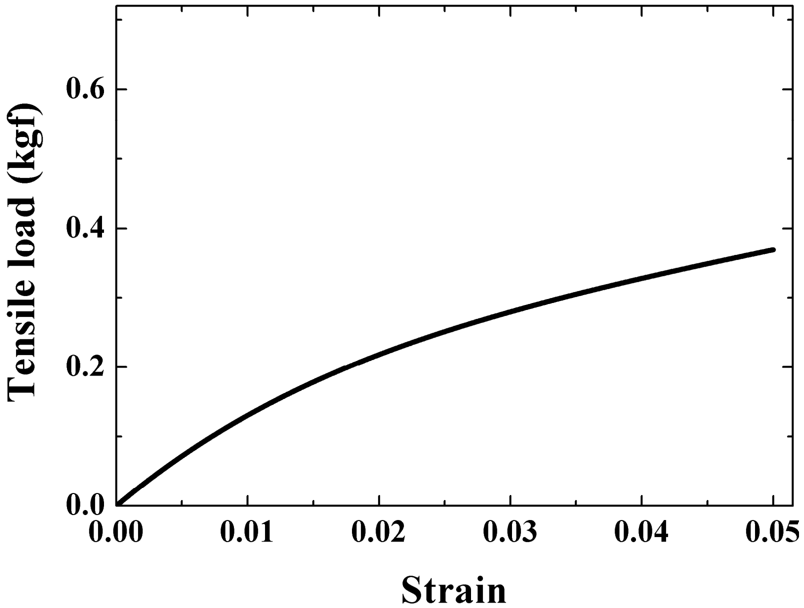

Figure 4.39 The 4-orderd fitted curve of averaged tensile test results of PI substrates

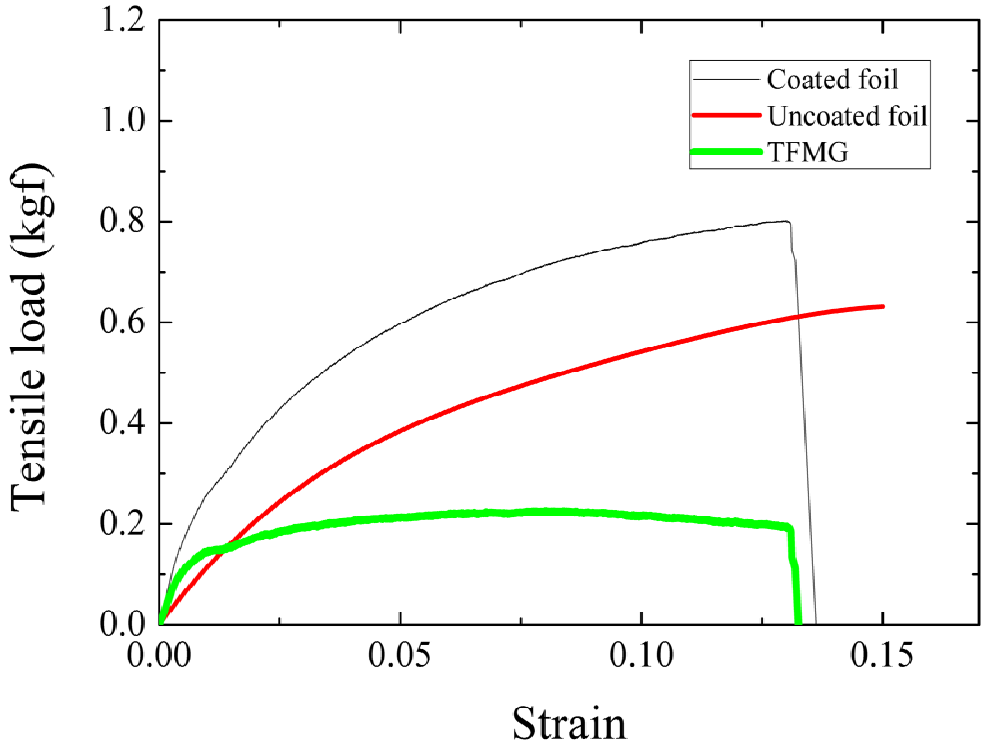

Figure 4.40 The schematic illustration of the extraction of TFMG tensile property by deducting the uncoated foil substrate from the coated foil.

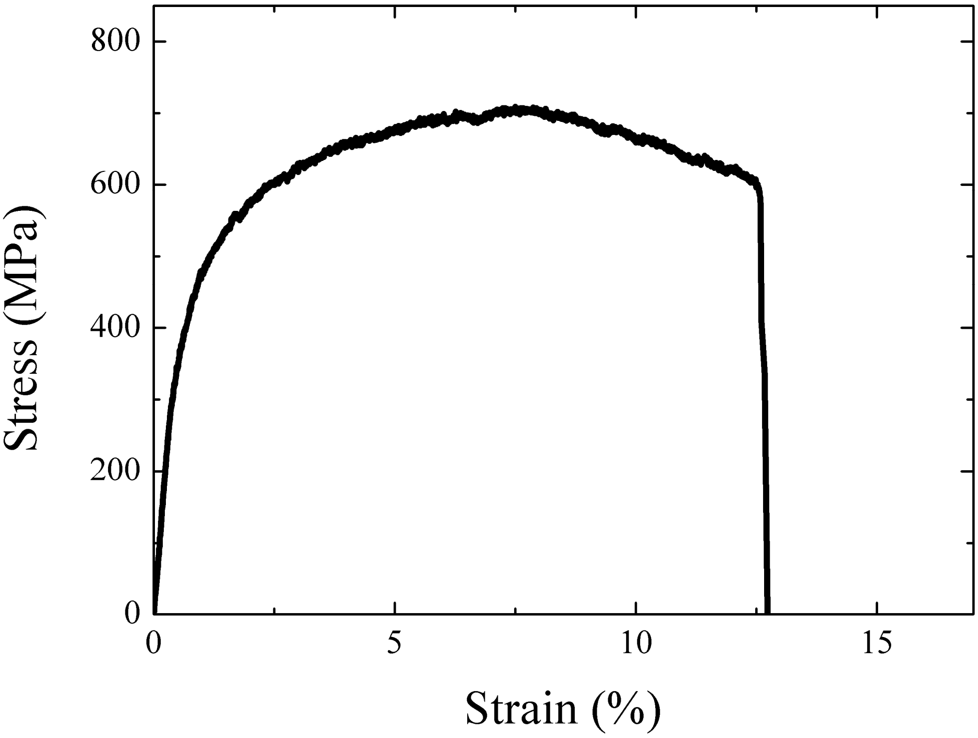

Figure 4.41 The representative engineering stress-strain curve of the ZrCu thin film 1 μm in thickness.

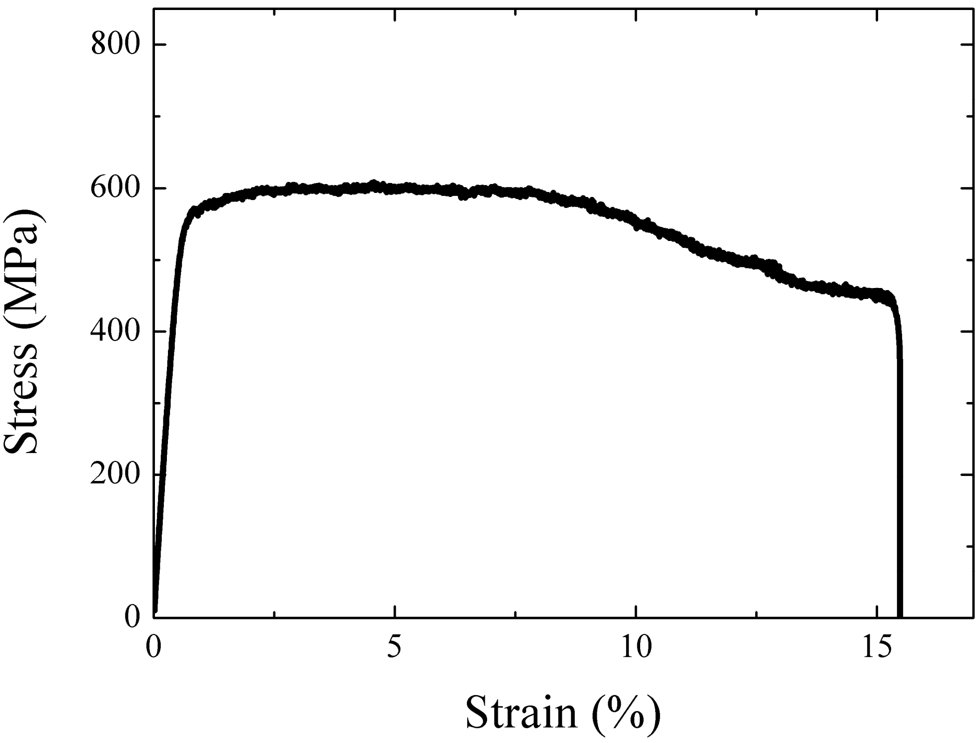

Figure 4.42 The representative engineering stress-strain curve of the nanocrystalline Cu thin film 1 μm in thickness.

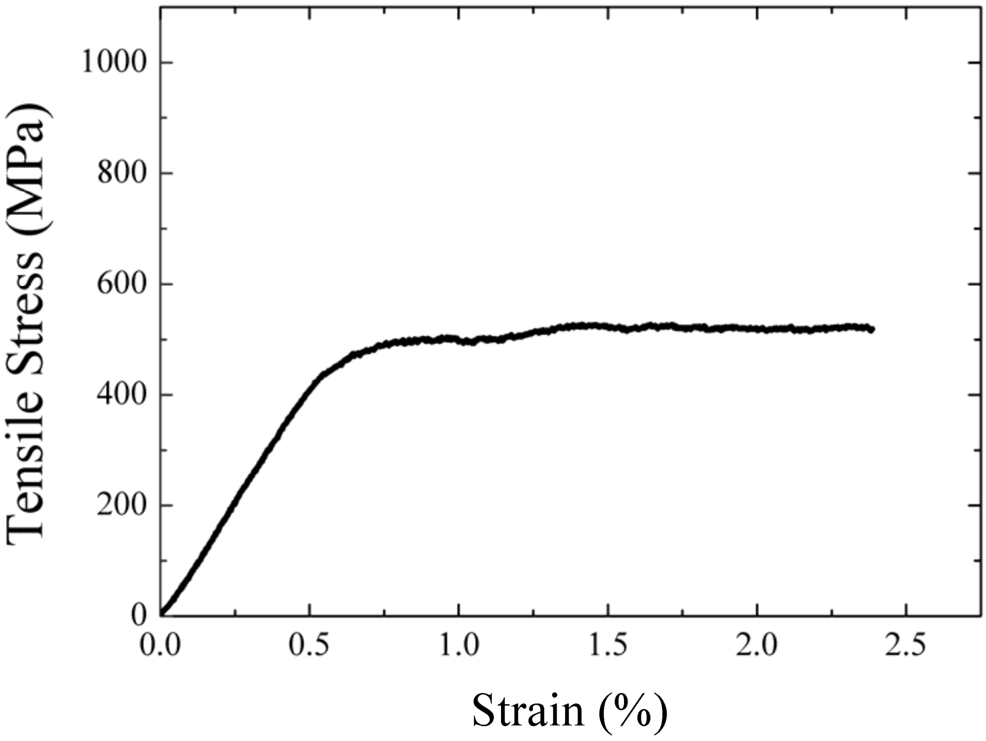

Figure 4.43 The representative engineering stress-strain curve to about 2% strain for the 1-μm-thick multilayered thin films of TFMG ZrCu and crystalline Cu layers with a thickness in 100 nm/100 nm.

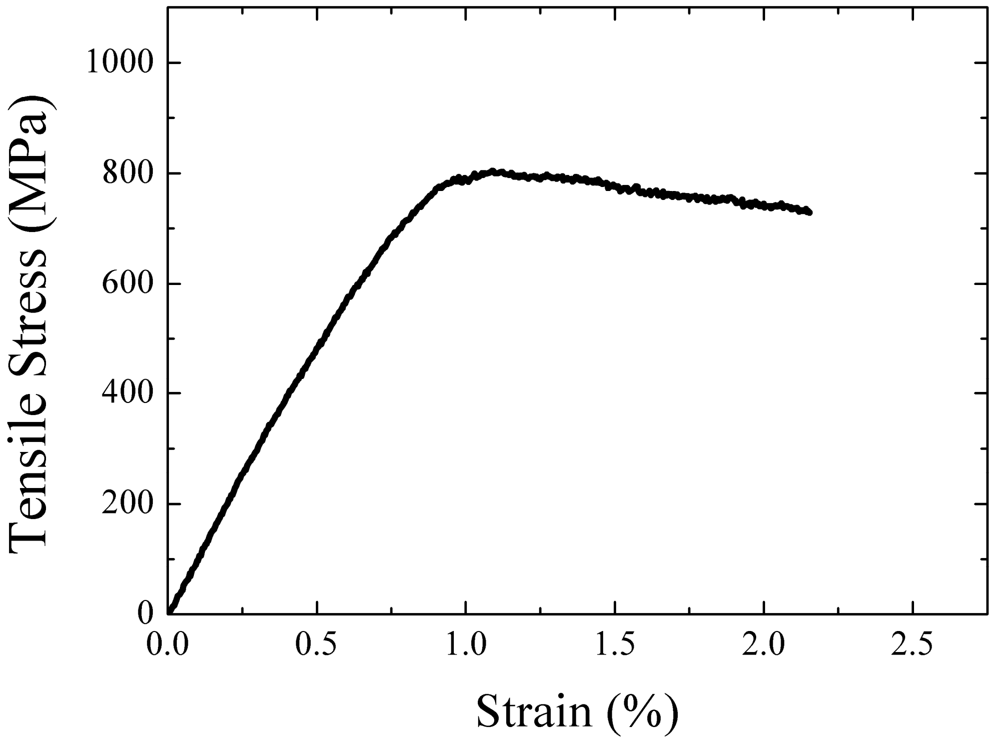

Figure 4.44 The representative engineering stress-strain curve to about 2% strain for the 1-μm-thick multilayered thin films of TFMG ZrCu and crystalline Cu layers with a thickness in 75 nm/75 nm.

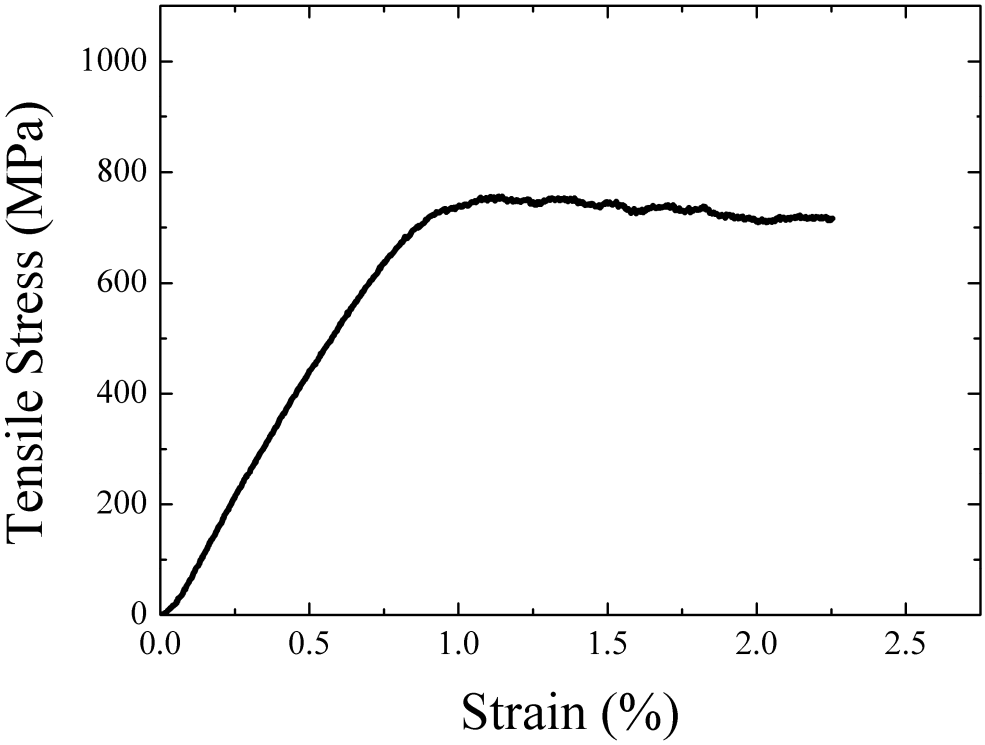

Figure 4.45 The representative engineering stress-strain curve to about 2% strain for the 1-μm-thick multilayered thin films of TFMG ZrCu and crystalline Cu layers with a thickness in 50 nm/50 nm.

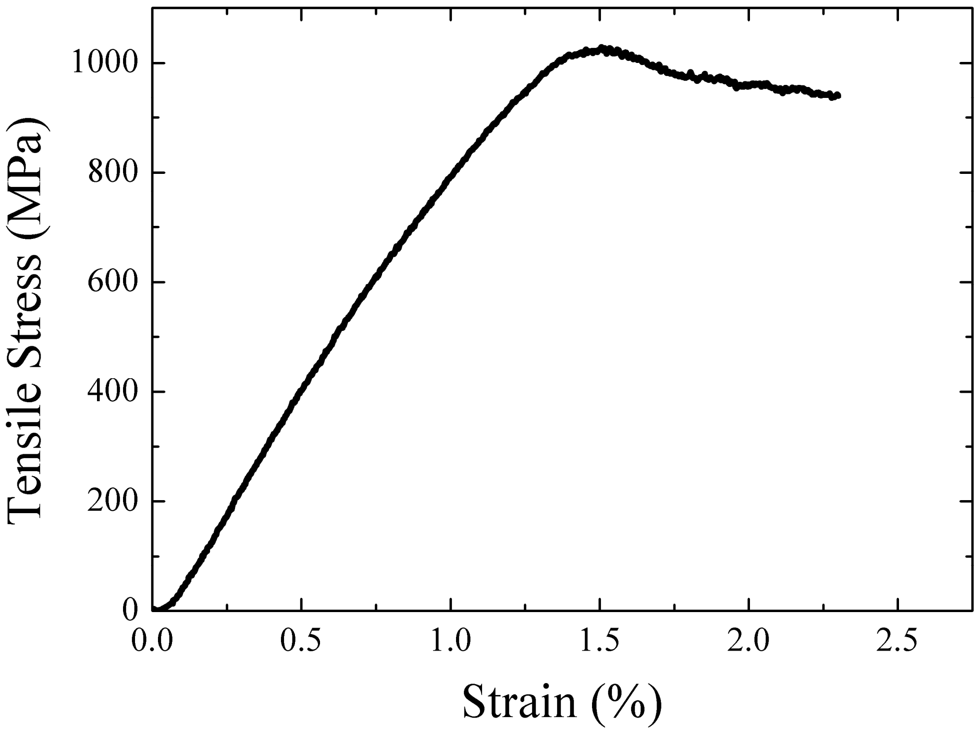

Figure 4.46 The representative engineering stress-strain curve to about 2% strain for the 1-μm-thick multilayered thin films of TFMG ZrCu and crystalline Cu layers with a thickness in 25 nm/25 nm.

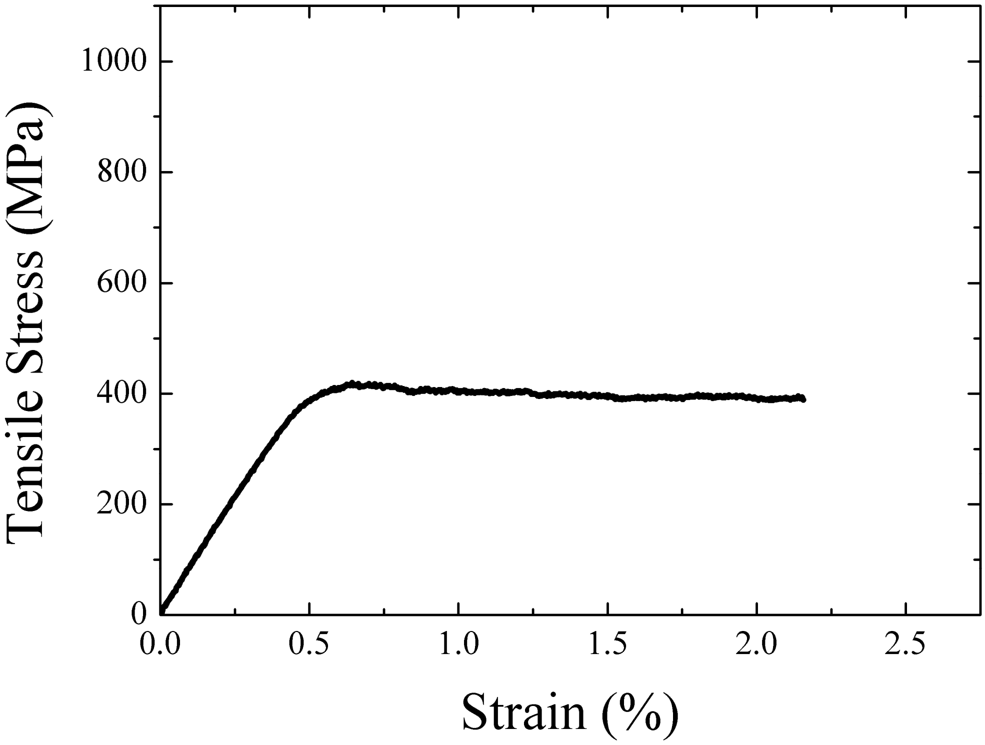

Figure 4.47 The representative engineering stress-strain curve to about 2% strain for the 1-μm-thick multilayered thin films of TFMG ZrCu and crystalline Cu layers with a thickness in 10 nm/10 nm.

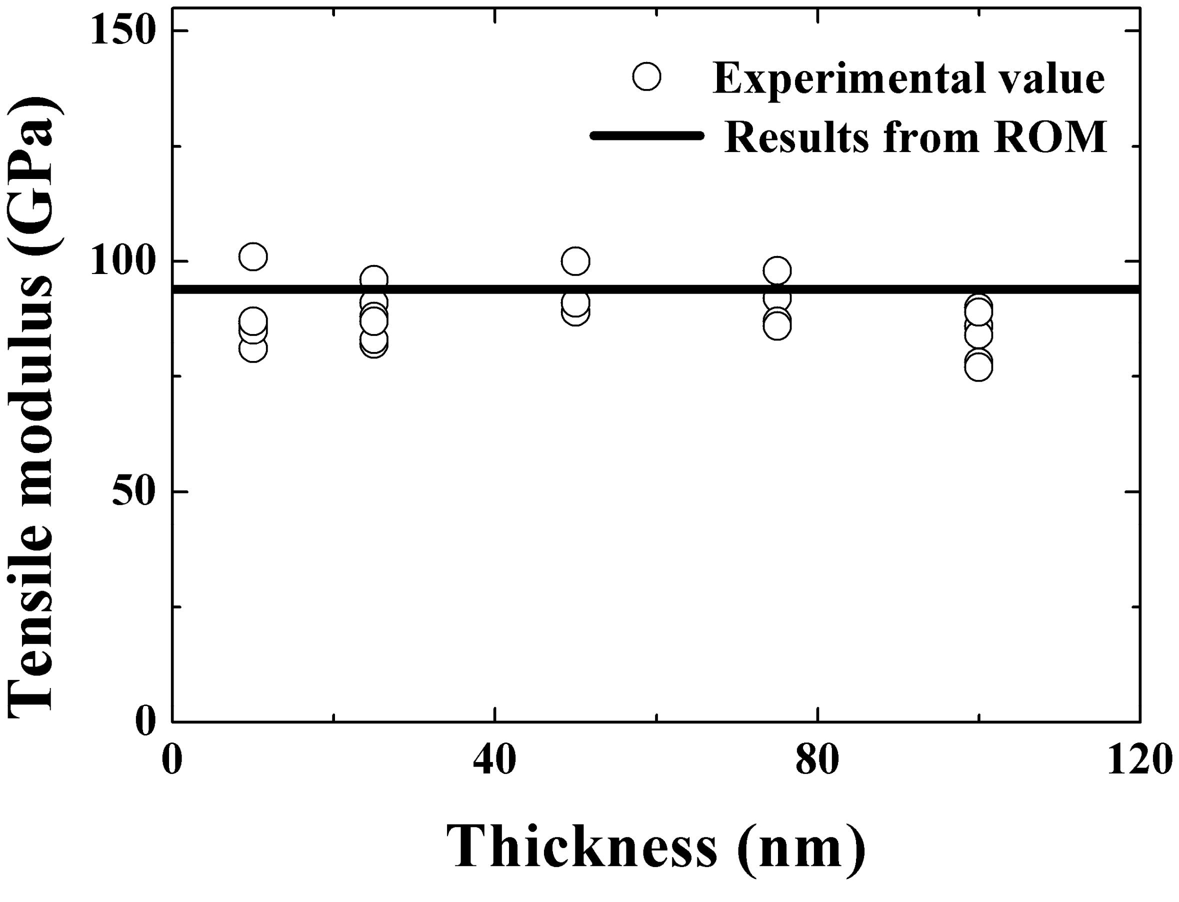

Figure 4.48 The dependence of the tensile modulus as a function of layer thickness.

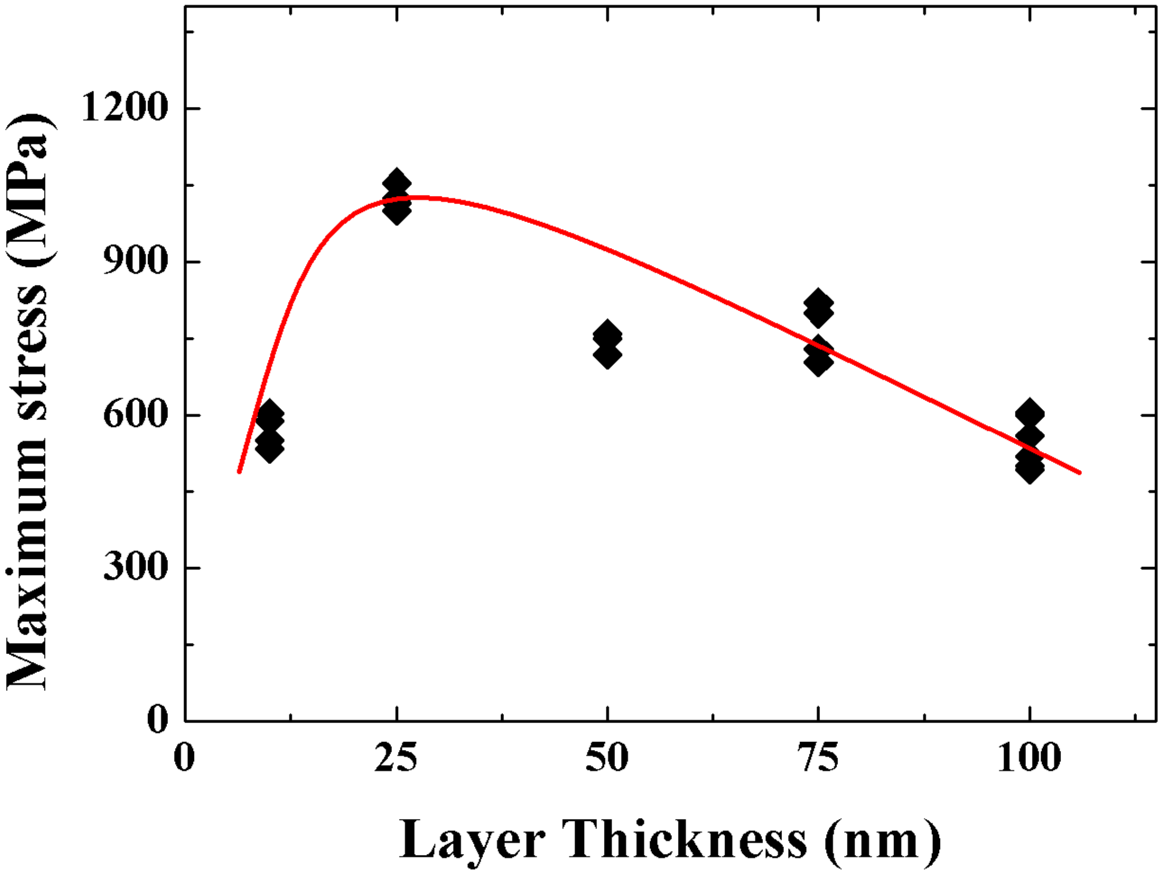

Figure 4.49 The dependence maximum stress of the tensile modulus as a function of layer thickness.

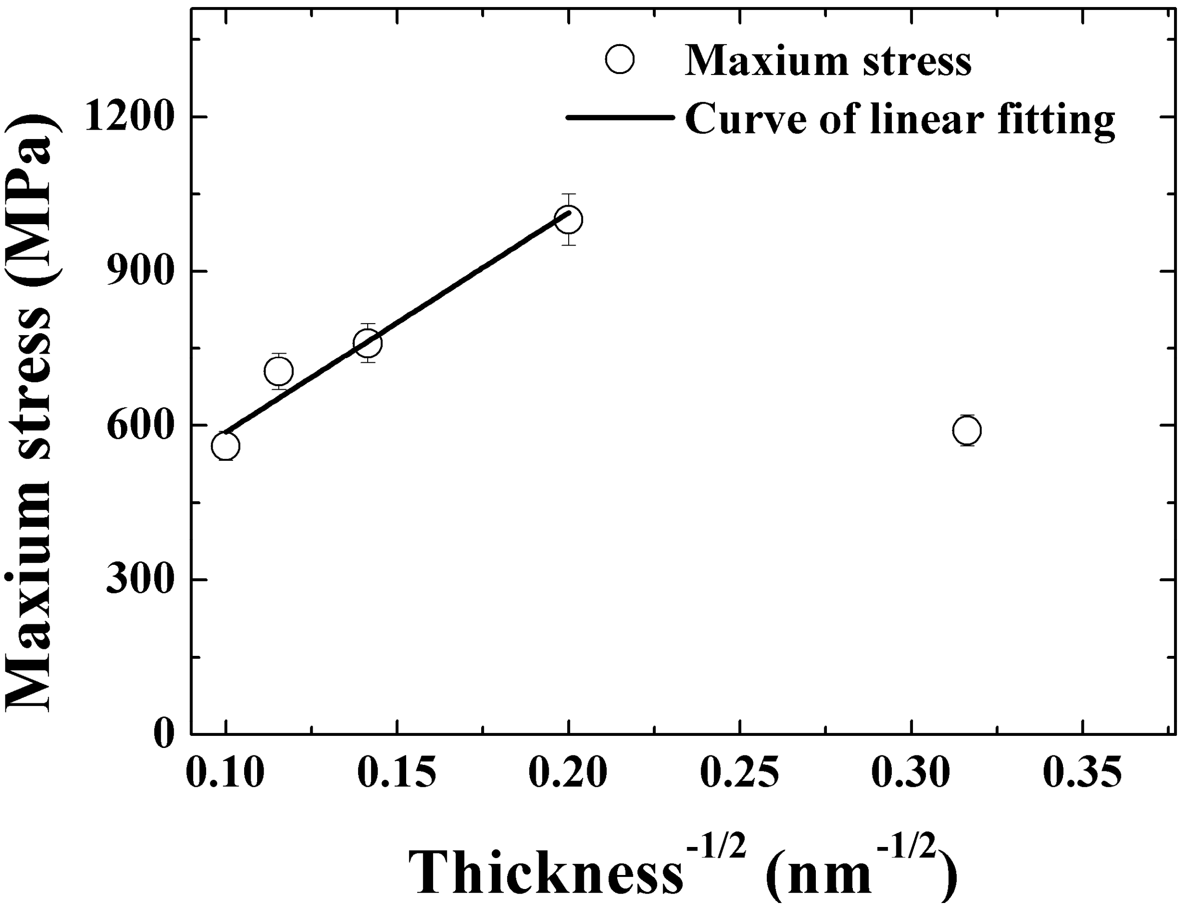

Figure 4.50 The Hall-Petch relation for multilayered ZrCu/Cu (100 nm/100 nm), (50 nm/50 nm), (25 nm/25 nm) and (10 nm/10 nm) multilayered samples.

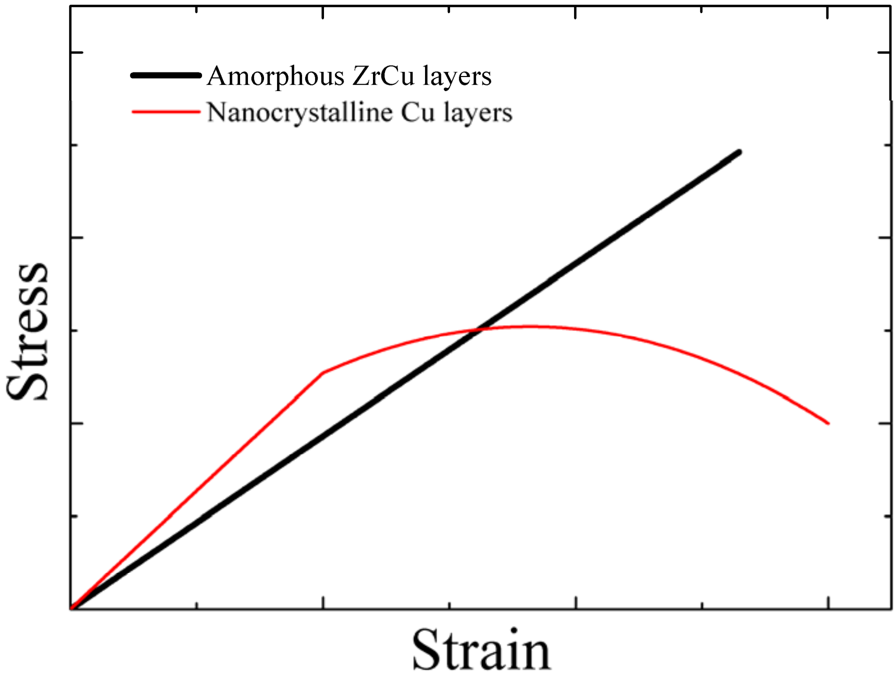

Figure 4.51 The schematic illustration of deforming behavior of amorphous ZrCu layers and nanocrystalline Cu layers.

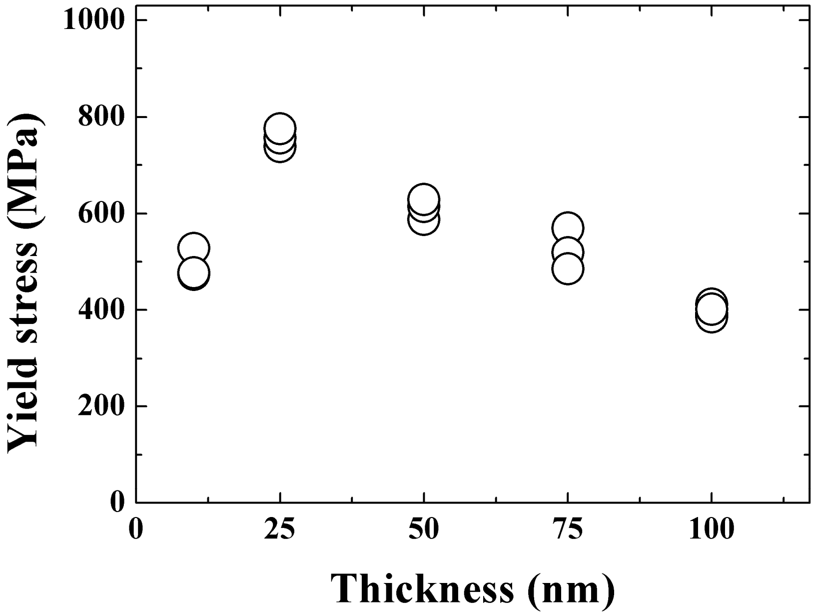

Figure 4.52 The dependence maximum stress of the tensile modulus as a function of layer thickness.

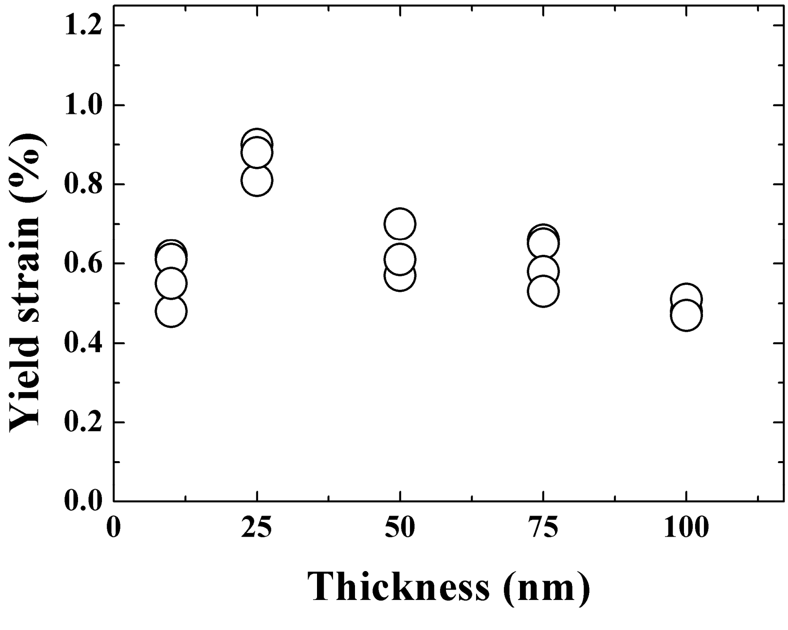

Figure 4.53 The dependence maximum stress of the tensile modulus as a function of layer thickness.

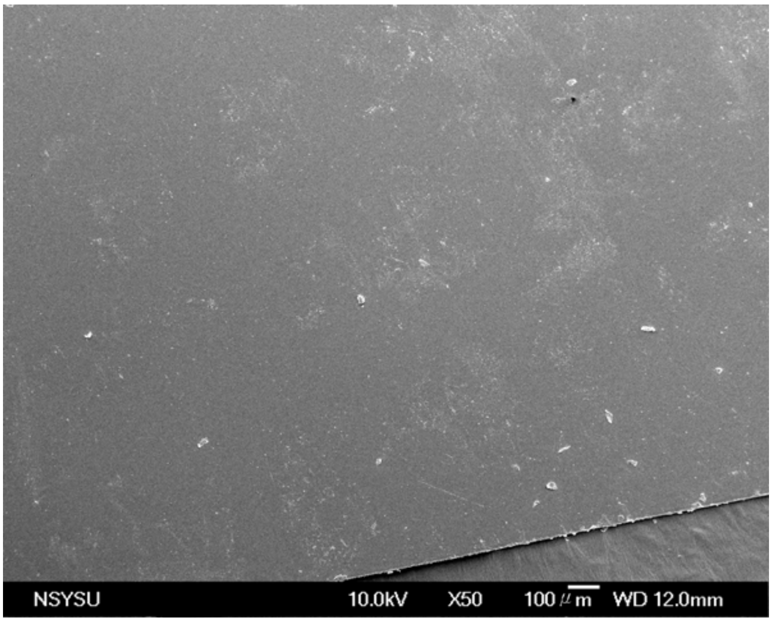

Figure 4.54 SEM surface morphology of the uncoated and tensile-loaded PI at a low magnification of 50X.

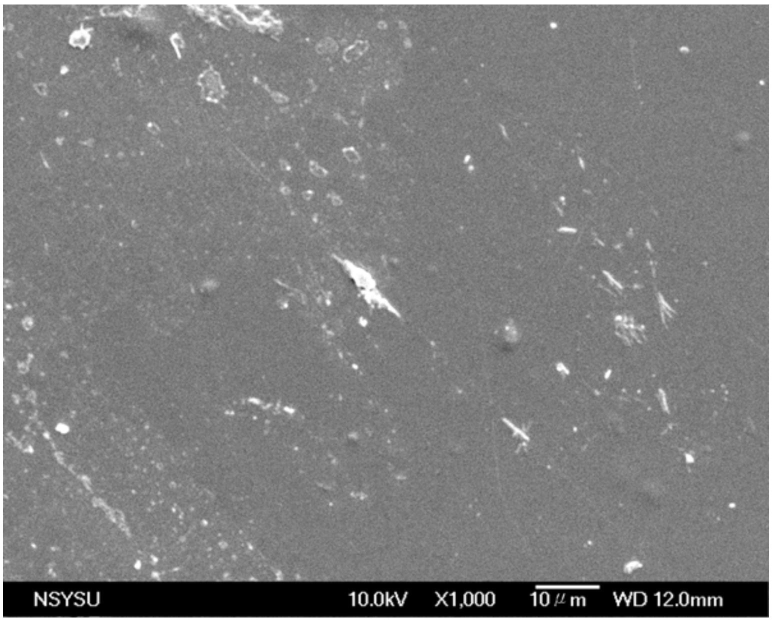

Figure 4.55 SEM surface morphology of the uncoated and tensile-loaded PI at a low magnification of 1000X.

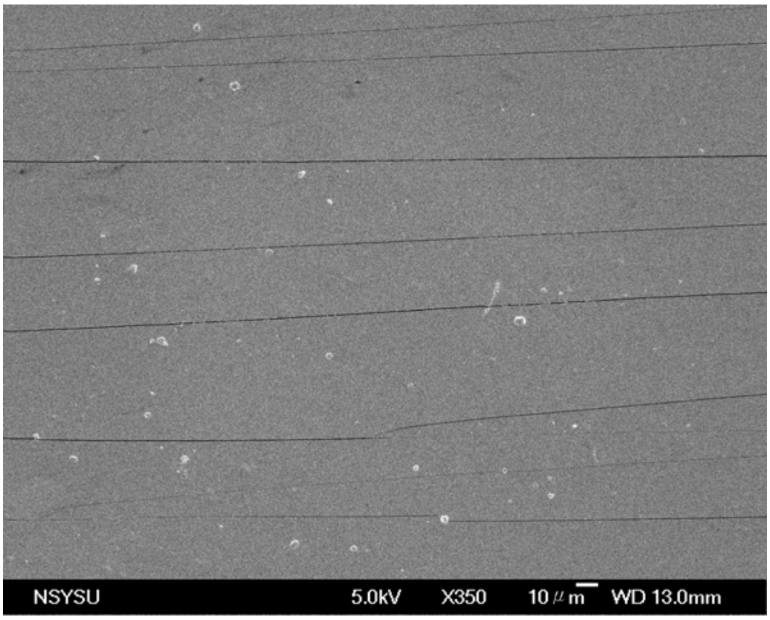

Figure 4.56 SEM surface morphology of the 1-µm-thick deformed monolithic amorphous ZrCu sample at a low magnification of 350X.

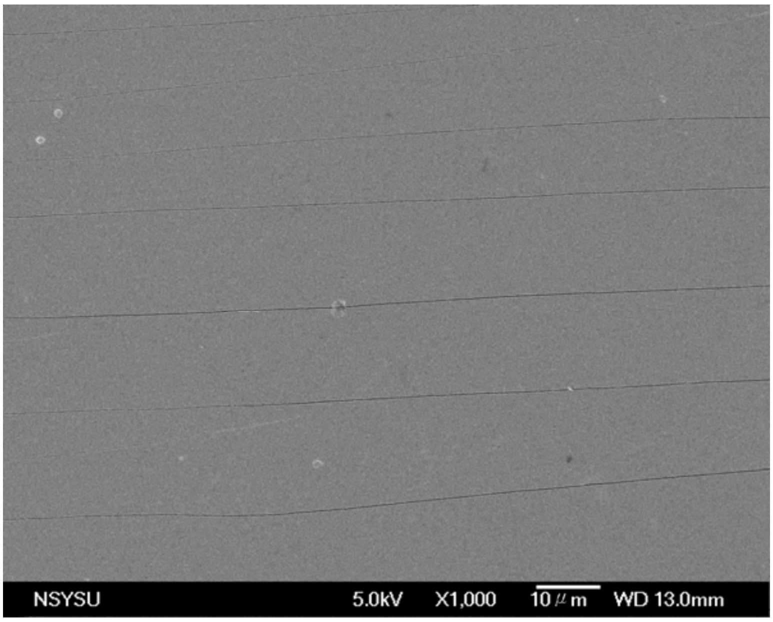

Figure 4.57 SEM surface morphology of the 1-µm-thick deformed monolithic amorphous ZrCu sample at a low magnification of 1000X.

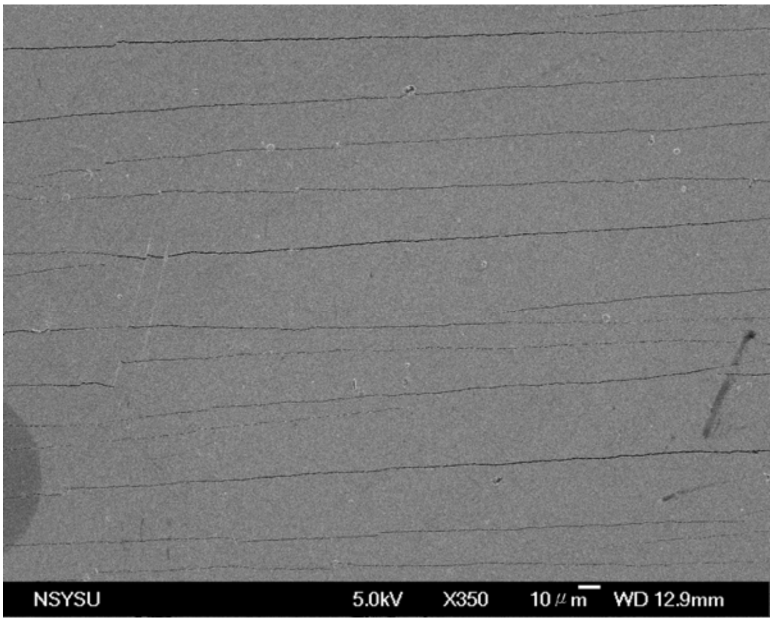

Figure 4.58 SEM surface morphology of the 1-μm-thick deformed monolithic Cu sample at a low magnification of 350X.

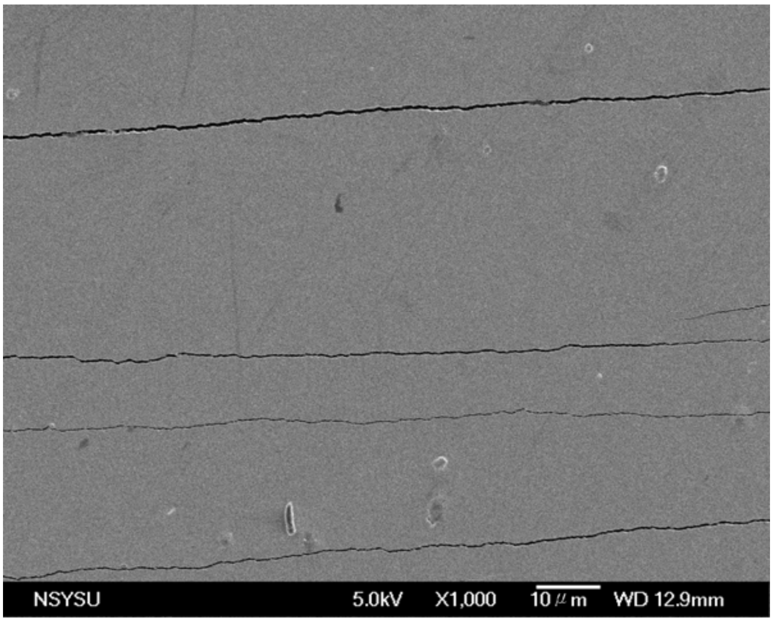

Figure 4.59 SEM surface morphology of the 1-μm-thick deformed monolithic Cu sample at a low magnification of 1000X.

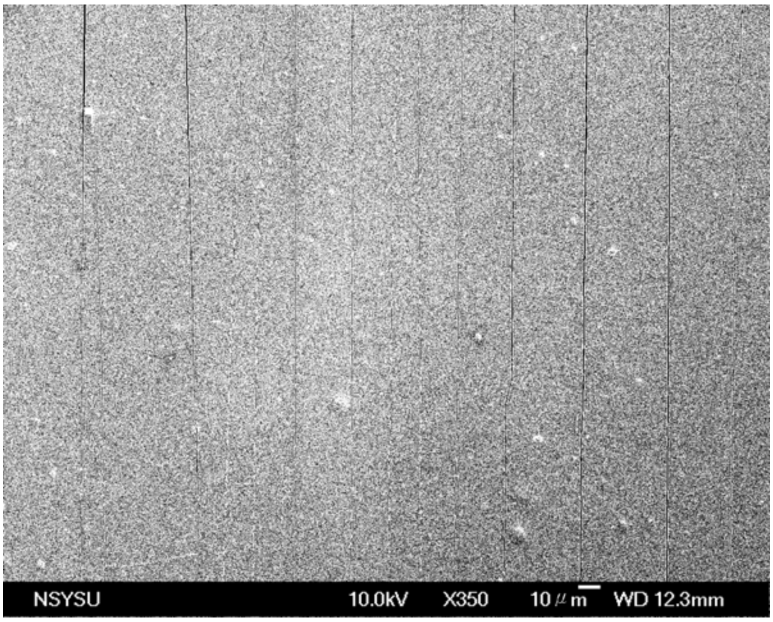

Figure 4.60 SEM surface morphology of the deformed ZrCu/Cu (100 nm/100 nm) multilayer sample at a low magnification of 350X.

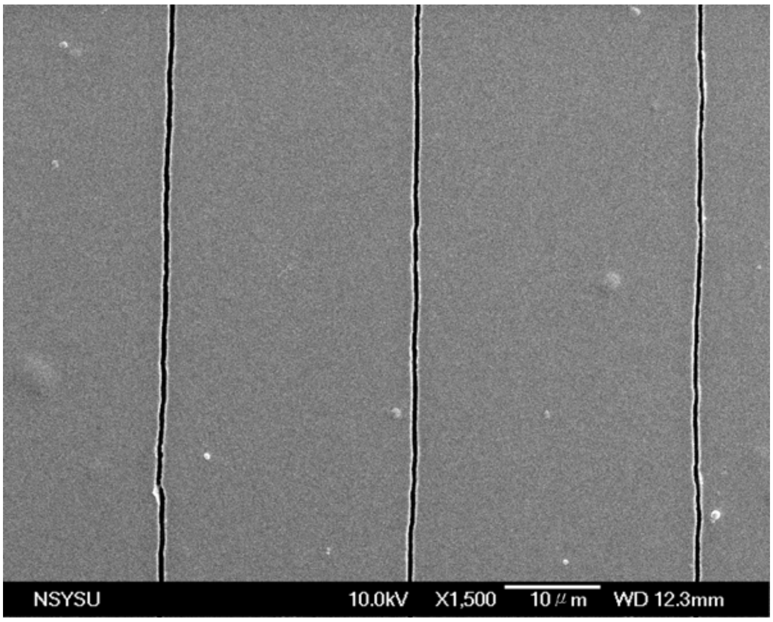

Figure 4.61 SEM surface morphology of the deformed ZrCu/Cu (100 nm/100 nm) multilayer sample at a low magnification of 1500X.

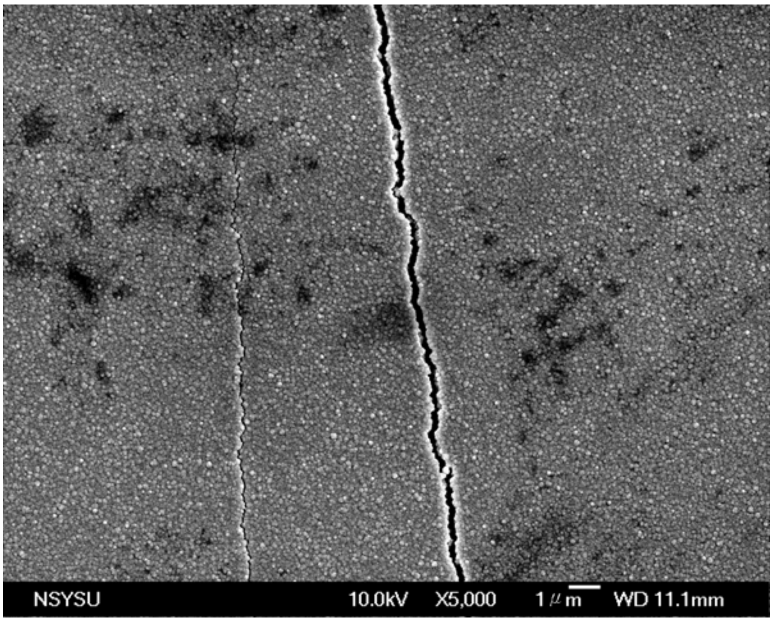

Figure 4.62 SEM surface morphology of the deformed ZrCu/Cu (100 nm/100 nm) multilayer sample at a high magnification of 5000X.

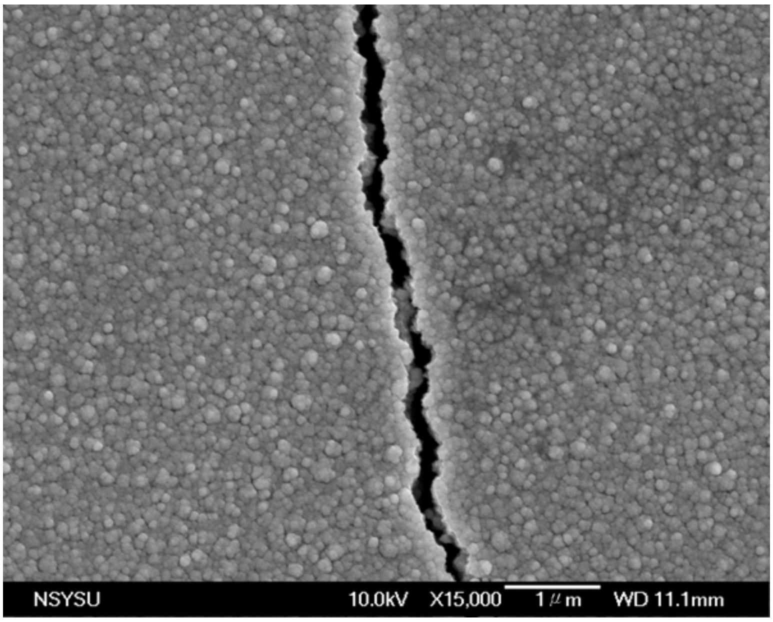

Figure 4.63 SEM surface morphology of the deformed ZrCu/Cu (100 nm/100 nm) multilayer sample at a low magnification of 15000X.

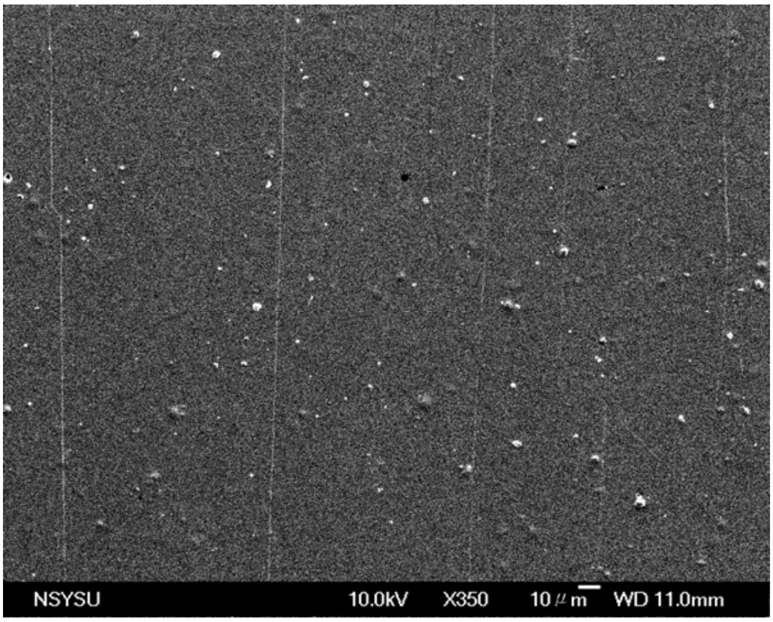

Figure 4.64 SEM surface morphology of the deformed ZrCu/Cu (50 nm/50 nm) multilayer sample at a low magnification of 350X.

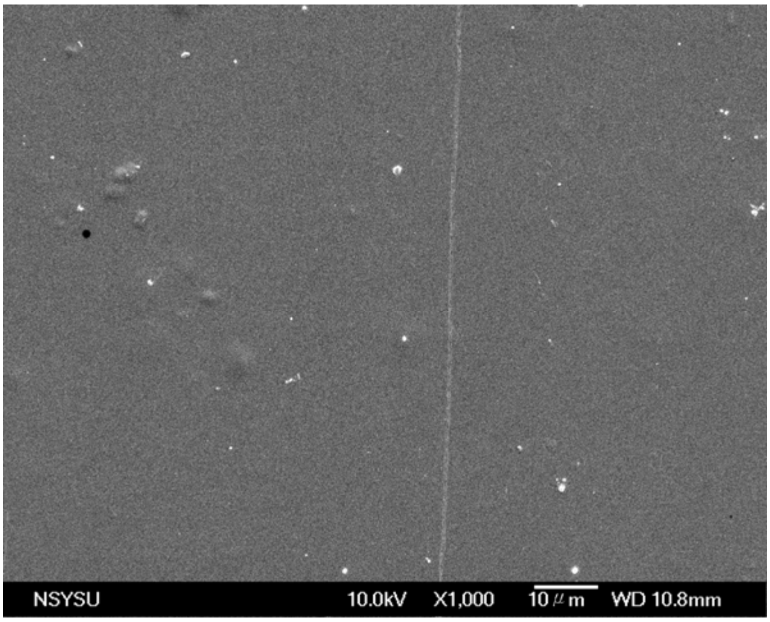

Figure 4.65 SEM surface morphology of the deformed ZrCu/Cu (50 nm/50 nm) multilayer sample at a low magnification of 1000X.

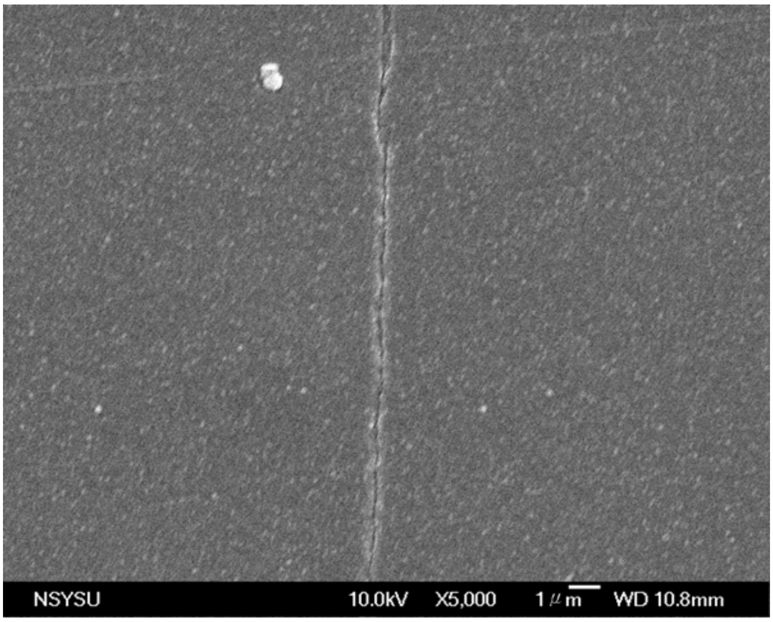

Figure 4.66 SEM surface morphology of the deformed ZrCu/Cu (50 nm/50 nm) multilayer sample at a high magnification of 5000X.

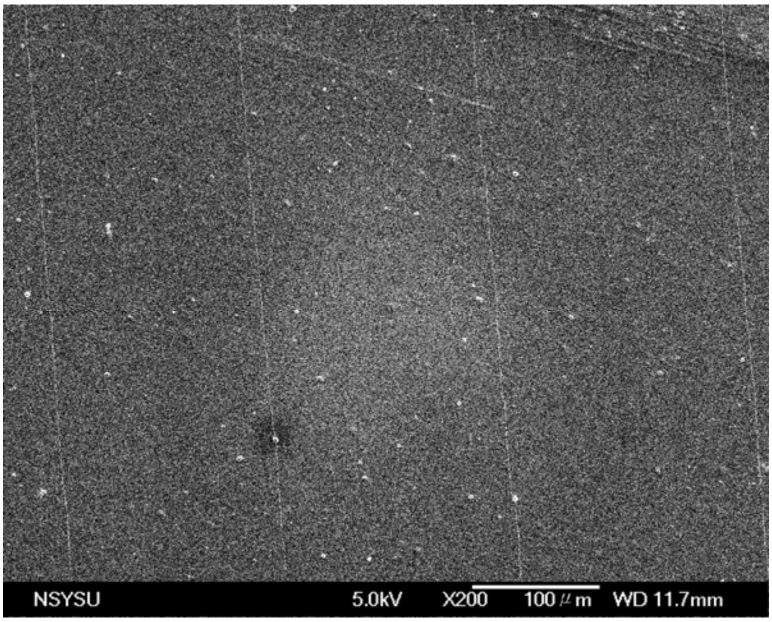

Figure 4.67 SEM surface morphology of the deformed ZrCu/Cu (25 nm/25 nm) multilayer sample at a high magnification of 200X.

Figure 4.68 SEM surface morphology of the deformed ZrCu/Cu (25 nm/25 nm) multilayer sample at a high magnification of 350X.

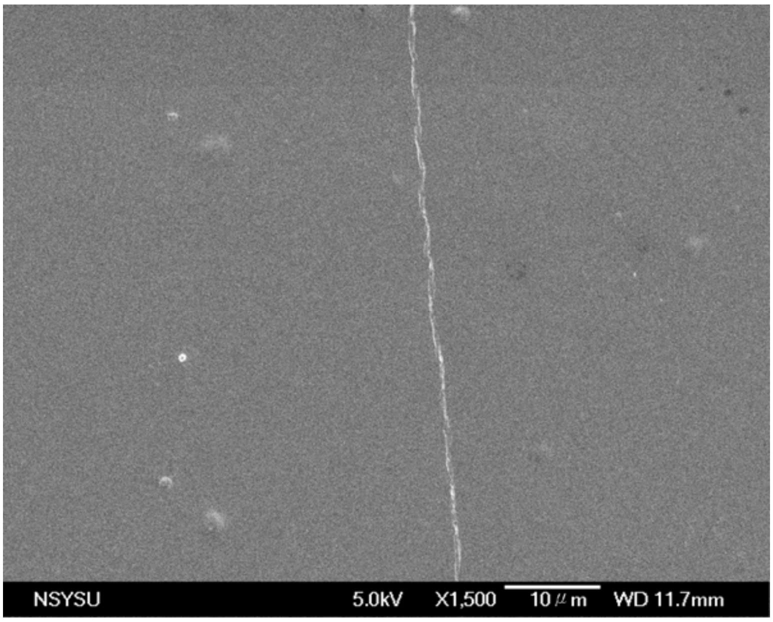

Figure 4.69 SEM surface morphology of the deformed ZrCu/Cu (25 nm/25 nm) multilayer sample at a high magnification of 1500X.

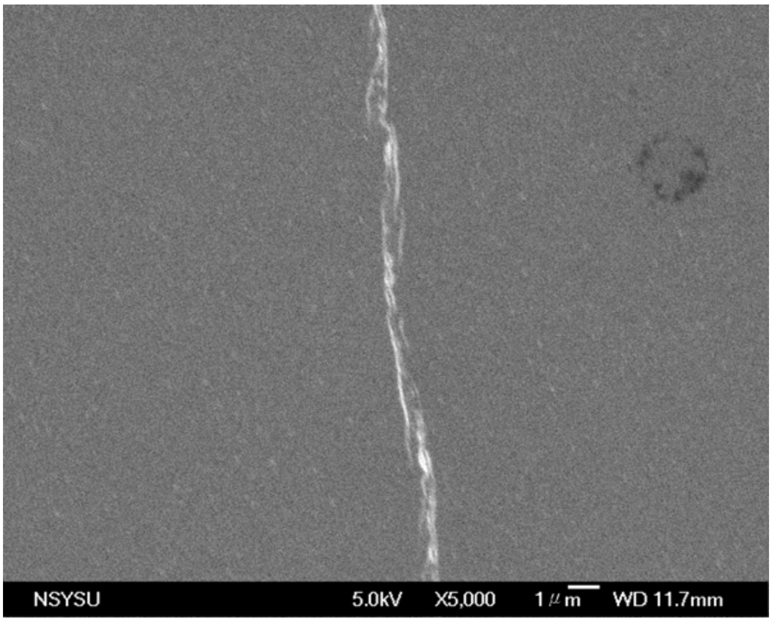

Figure 4.70 SEM surface morphology of the deformed ZrCu/Cu (25 nm/25 nm) multilayer sample at a high magnification of 5000X.

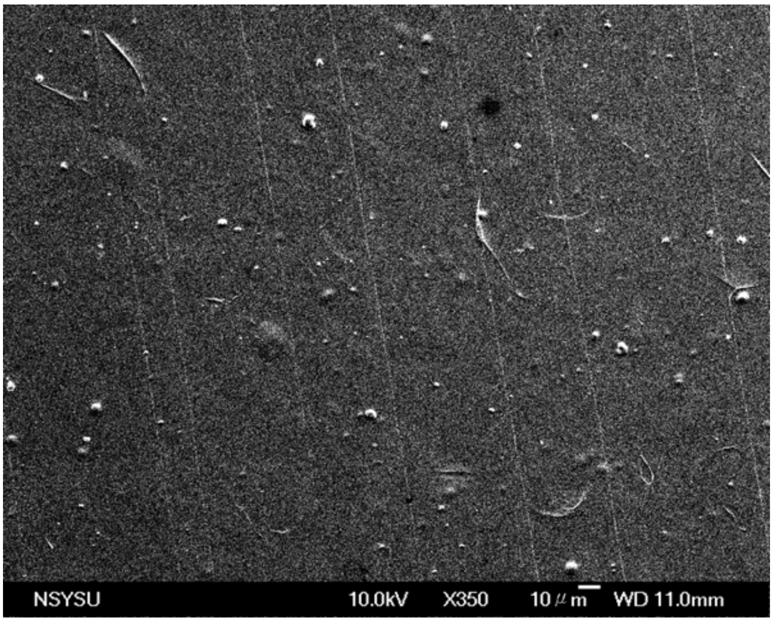

Figure 4.71 SEM surface morphology of the deformed ZrCu/Cu (10 nm/10 nm) multilayer sample at a low magnification of 350X.

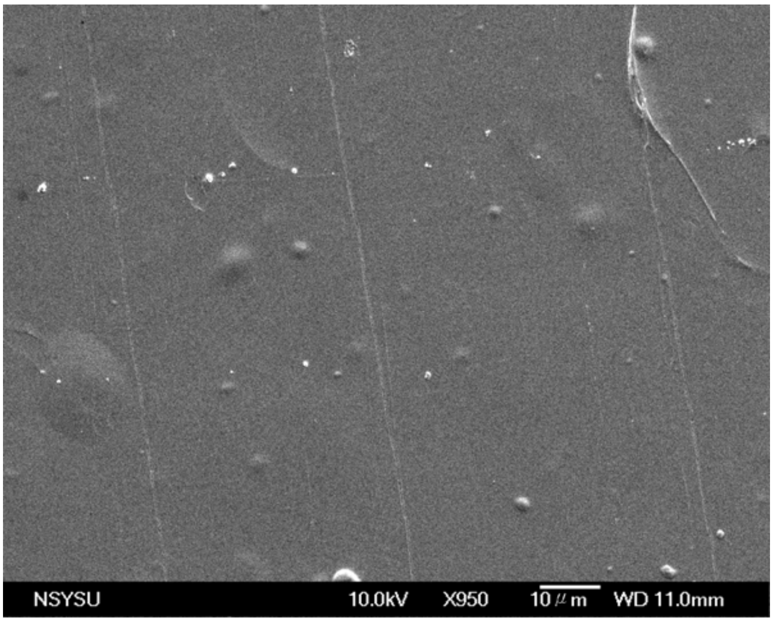

Figure 4.72 SEM surface morphology of the deformed ZrCu/Cu (10 nm/10 nm) multilayer sample at a low magnification of 950X.

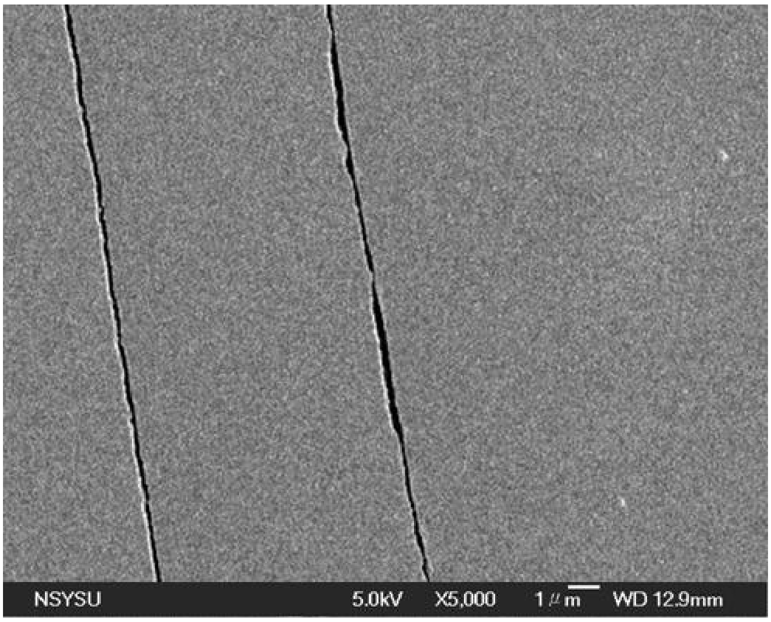

Figure 4.73 SEM surface morphology of the deformed ZrCu/Cu (10 nm/10 nm) multilayer sample at a high magnification of 5000X.

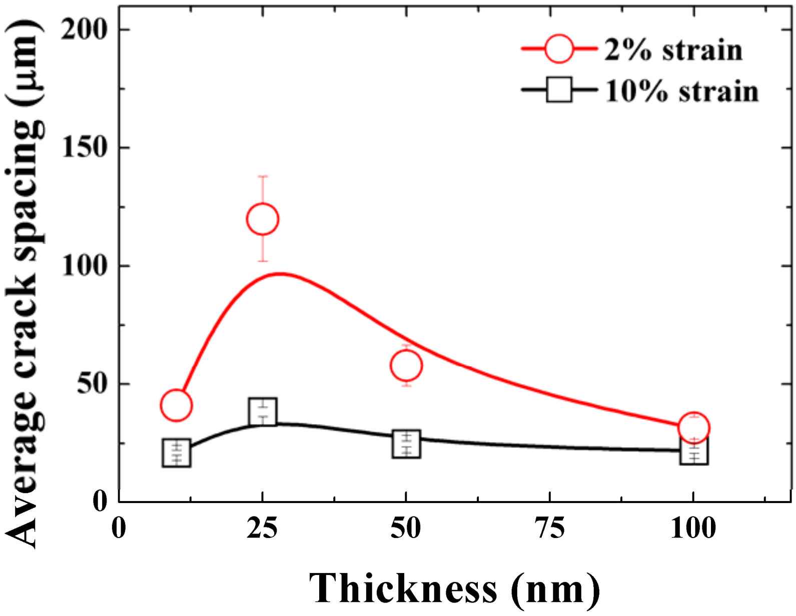

Figure 4.74 The schematic illustration of average spacing between microcracks after 2% strain and more 10% of ZrCu/Cu (100 nm/100 nm), ZrCu/Cu (50 nm/50 nm), ZrCu/Cu (25 nm/25 nm) and ZrCu/Cu (10 nm/10 nm)

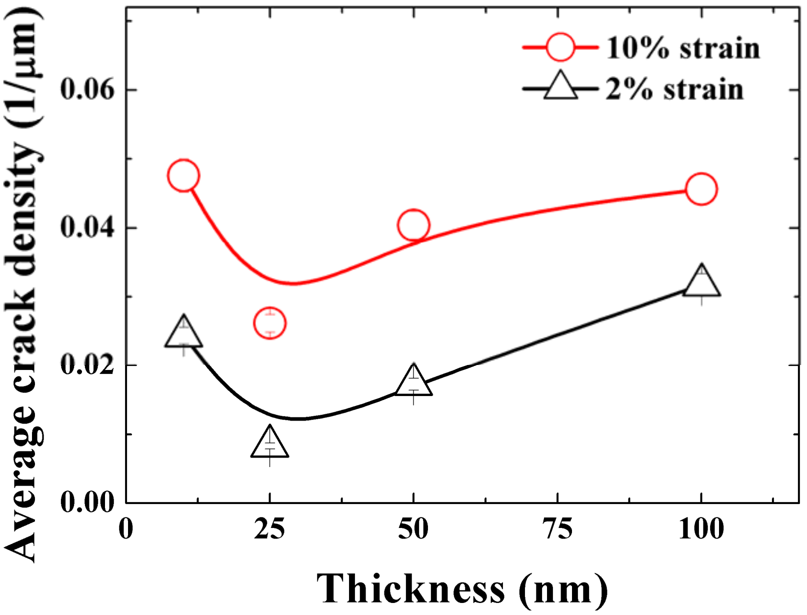

Figure 4.75 The schematic illustration of average crack density after 2% strain and more 10% of ZrCu/Cu (100 nm/100 nm), ZrCu/Cu (50 nm/50 nm), ZrCu/Cu (25 nm/25 nm) and ZrCu/Cu (10 nm/10 nm)

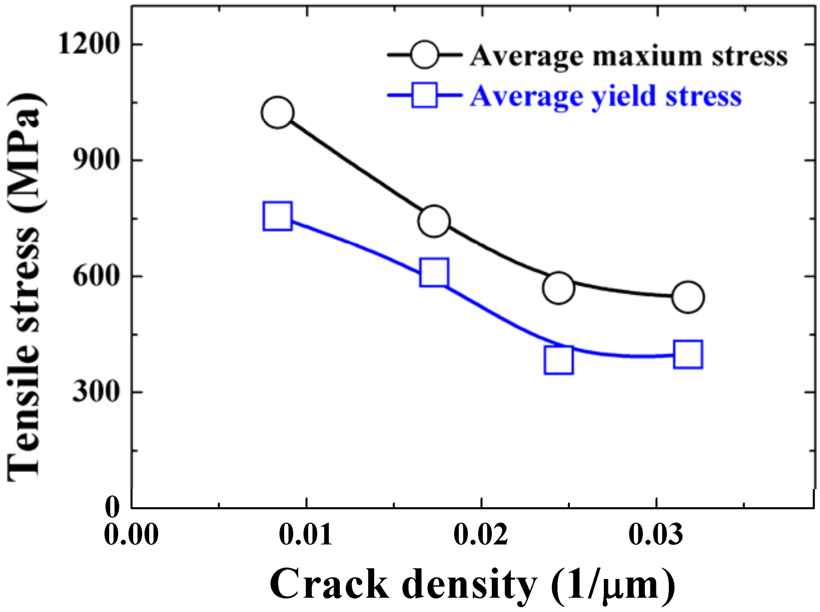

Figure 4.76 The schematic illustration of average crack density after 2% strain versus the average maximum stress of multilayered thin film.